CDF/DOC/SEC_VTX/CDFR/1922
January 12, 1993

SVX II Upgrade Proposal and Simulation Study

This CDF note is a copy of the SVX II upgrade proposal which was submitted to Fermilab on January 18, 1993. The individuals who helped prepare this proposal and the CDF Institutions presently participating in this upgrade project are listed below.

Authors

Nicola Bacchetta, Bruce Barnett, Ed Barsotti, Daniela Bartoletto, Robert Ely, Mark Frautschi, Art Garfinkel, Mike Gold, Hector Gonzalez, Ping Hu, Richard Hughes, Mike Lindenmeyer, John Matthews, Aldo Menzione, Giovanni Punzi, Fabrizio Raffaelli, Paul Ratzmann, Luciano Ristori, Vic Scarpine, Sally Seidel, Paul Shepard, Prem Singh, Alan Sill, John Skarha, Jeff Spalding, Jeff Wolinski.

SVX II Upgrade Group

Fermilab, Johns Hopkins, LBL, U. of New Mexico, U. of Padova, U. of Pennsylvania, U. of Pisa, U. of Pittsburgh, Purdue, U. of Rochester, Texas A&M

Contents

1 Summary

The accumulated CDF data make it clear that high resolution vertex detection is a key tracking component in the CDF program of high p_T physics, specifically the top search, and b physics. The planned increase in the number of p and $\bar{p}$ bunches in the accelerator in 1996, and the resulting shorter bunch spacing (132 ns or 395 ns) requires a replacement for the SVX and SVX′ detectors. Based on the experience gained with the current SVX detector we are proposing SVX II Stage 1 which is capable of operating with the shorter bunch spacing and which extends the high p_T and b physics capabilities of the present vertex detector.

The SVX was installed at the beginning of the current Run Ia. It has been successfully commissioned and the data taken demonstrates that it is working reliably and well (see below). Based on performance of the SVX we have confidence that the SVX II upgrade can be constructed, and will substantially strengthen the physics capabilities of CDF. This proposal to build the SVX II Stage 1 detector must be regarded as an urgent priority for CDF for Run II to start in 1996.

This document constitutes a proposal to begin the construction of the barrel portion of an upgraded silicon vertex detector. This SVX II Stage 1 detector is needed by CDF in order to both maintain and extend its capability to pursue the high p_T top search and mass measurement which is both the collaboration's and the laboratory's highest priority. SVX II Stage 1 also provides a necessary step in the evolution of the physics capabilities of the CDF detector toward an ambitious b physics program for the latter half of the decade.

In summary the design goals for the the SVX II upgrade are:

1. Accommodate improvements to the accelerator which necessitate replacement of the SVX, specifically shorter inter-bunch spacing and higher radiation levels. This is required for Run II which is the first run with the reduced bunch spacing.

2. Improve performance for vertex detection in high p_T physics, in particular to tag b decay vertices in top events.

3. Enhance the b physics capabilities of the present detector.

4. Provide a detector and electronic readout capable of supporting a Level 2 vertex trigger processor.

Features of the SVX II Stage 1 Barrel Detector

A summary of the SVX II barrel detector for which we are seeking stage 1 approval is given below:

- A set of three barrels which approximately double the length of the present SVX. See Fig. 1(a) and (b).

- Double-sided detectors with 90 degree stereo. The proposed detectors with intermediate strips and 7-bit analog to digital conversion should attain a resolution of $\approx 10\mu$m in r-ϕ and $\approx 25\mu$m in r-z.

- A pipelined readout chip which will support operation at either 395 ns or 132 ns between beam crossings.

- High speed digitization and readout of the SVX II analog data in $<5\mu$s in response to a level 1 trigger. The high speed of the readout is required in order to use the SVX II data in a level 2 vertex trigger processor.

- Support for a level 2 microvertex trigger processor (SVT). [1] This is a separate project which is being developed by the CDF collaboration. The ability to trigger on the impact parameters of reconstructed tracks will greatly extend the physics capabilities of the CDF detector.

- A new data acquisition system (DAQ) employing a highly parallel fibre optic readout and control utilizing low power optic drivers and receivers.

We expect the top physics program and other high p_T physics topics to be helped by increasing the length of the vertex detector in order to improve coverage of the luminous region in z at the interaction point. Doubling the length and adding z information will increase the b tag efficiency for top events by a factor of 1.6 to 2.0 depending on the top mass. In combination with an increase in luminosity, this increased efficiency gives a dramatic improvement to the overall physics capabilities of the detector.

The capability of using impact parameter information obtained from a vertex detector in the level 2 trigger to select events with secondary vertices will be of fundamental importance for any experimental program of b physics in a hadron collider environment. Having an impact parameter trigger implemented for SVX II will significantly increase the size of the b sample on tape. The experience gained in installing and running this trigger will help us to design more ambitious triggering systems in the future.

Upgrade Path

The SVX II barrel detector proposed here is the detector required to pursue the high p_T physics goals of the CDF collaboration once the collider begins operation with the shorter bunch spacing. It is also the first stage in a two stage upgrade path. The second stage would add forward disks to extend the η coverage out to approximately three. This additional η coverage is necessary for CDF to pursue b physics goals such as B_s mixing and CP violation studies with good flavor tagging capabilities.

This Stage 2 system greatly improves both the ability of the collaboration to pursue b physics and the solid angle coverage for several high p_T physics topics such as the measurement of the charge asymmetry for W production. We believe that our upgrade program will provide a powerful vertex detector with the large η acceptance required for flavor tagging in

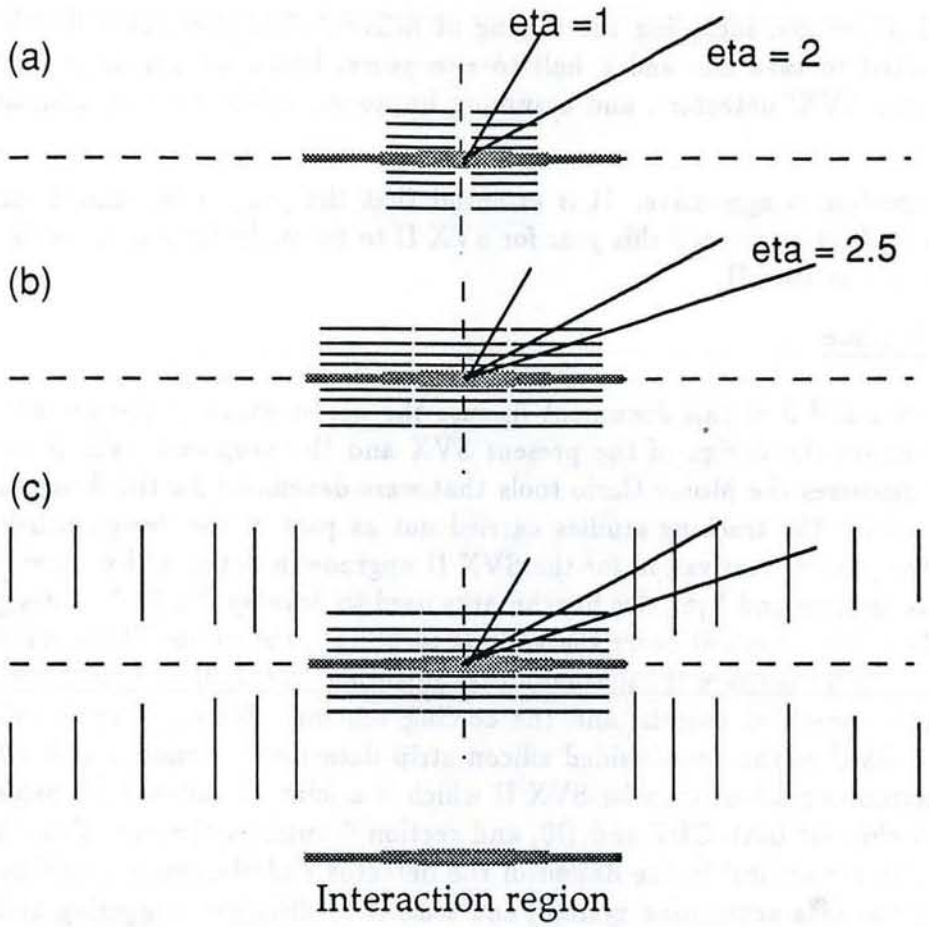

Figure 1: Schematic of the upgrade concept showing: (a) The present SVX. Barrel geometry with a total length of 51 cm. (b) SVX II Stage 1. Barrel geometry with a total length of 102 cm, still contained within the present VTX. (c) SVX II Stage 2. As (b) with the addition of disk detectors for forward tracking.

order to pursue a b physics program into the Main Injector era where measurements involving B mixing and CP violation studies will be important physics objectives. Figure 1 shows the present SVX layout and our SVX II Stage 1 and 2 concept. Stage 1 can be viewed as a detector for Run II in 1996, with Stage 2 an addition for the Main Injector running in the latter part of the decade. The proposal presented here covers the Stage 1 barrel portion of the SVX II upgrade.

Summary of Manpower, Schedule and Cost

Our initial estimate for the project cost in materials and services for the SVX II barrel detector is \$3.8M, of which \$360K will be spent on R&D in FY93, with the major purchases in FY94. With this funding, and with the level of manpower outlined in section 12 the detector will be ready for installation in January 1996. This requires that the design and R&D work be completed and that the final design decisions be made by early 1994. The

construction process, including the testing of delivered components and sub-assemblies is then expected to take one and a half to two years, based on our experience in building the SVX and SVX′ detectors, and assuming improved efficiency with additional assembly facilities.

This schedule is aggressive. It is essential that the project be funded, and the design and R&D be fully supported this year for SVX II to be ready for the operation with shorter bunch spacing in Run II.

Proposal Outline

Sections 2 and 3 of this document discuss the performance of the present SVX in Run Ia and compare the design of the present SVX and the proposed SVX II barrel detector. Section 4 discusses the Monte Carlo tools that were developed for the design of SVX II and gives results for the tracking studies carried out as part of the design process. Section 5 presents the physics motivation for the SVX II upgrade in detail and presents the results of the various high p_T and b physics benchmarks used to develop the SVX II design. Sections 6 through 11 of the proposal cover the various technical subsystems of the SVX II barrel detector. Section 6 discusses the mechanical engineering and design of the SVX II bulkheads, ladders and assembled barrels, and the cooling scheme. Section 7 covers the design and continuing R&D of the double-sided silicon strip detectors. Section 8 addresses the design of the electronics readout chip for SVX II which is a joint Fermilab/LBL project to provide a common chip for both CDF and D0, and section 9 outlines the radiation damage considerations that are critical in the design of the detector and electronics. Section 10 discusses the rest of the data acquisition system, and section 11 discusses triggering and in particular the level 2 trigger processor development. Finally section 12 discusses the cost, manpower and schedule for the Stage 1 SVX II project.

2 SVX Performance

The SVX detector has been installed in CDF and is currently taking data in Run Ia. The installation and commissioning has gone smoothly. In this section we summarize initial indications of SVX performance and potential.

During the spring and summer of 1991, the two SVX barrels were assembled at Fermilab. Optical survey information was used to measure the position of each silicon microstrip detector to 10 microns. First $\bar{p}p$ collisions were observed in the SVX in April, 1992, and as of mid-December CDF had collected 5 pb^{-1} of data with the SVX. Through the commissioning of the Tevatron and CDF, no serious damage, radiation or otherwise, has occurred to the detector. Greater than 98.7% of the 46,080 strips are functioning well. Included in the bad-strip count are 128 channels from the one SVX chip (out of a total of 360) that has failed. Fits to the Landau distribution of SVX hits show a signal-to-noise in routine CDF operations of about 9:1. Occupancies are typically 8% with 2% coming from physics, and

6% coming from noise fluctuations. Much of the noise contribution could be reduced with additional flexibility in setting the readout threshold levels. Nevertheless, the occupancy is still such that the SVX is a factor of three away from limiting the CDF DAQ readout time.

Tracks are reconstructed in the SVX by projecting found tracks in the central tracking chamber back into the SVX. We have compared the ratio of three-layer to four-layer SVX tracks in order to measure the individual layer hit efficiencies. They range from 97% to 99% with on-going improvements in the hit association and clustering algorithms being made to gain efficiency.

The addition of the SVX has made a noticeable improvement to the CDF momentum and mass resolution. For the $J/\psi \rightarrow \mu^+\mu^-$ data sample, the J/ψ mass width reduces by 35% from 26 MeV/c^2 (CTC only, no beam constraint) to 17 MeV/c^2 (CTC + SVX combined fit) when the SVX hits are included. This should help in the reconstruction of exclusive B meson final states and preliminary results are expected soon. Improvement in the W boson mass resolution is also anticipated.

Much care and attention was paid during the SVX design and construction to the use of low mass materials and components. The result was an $\sim$ 3% of a radiation length of material contribution (at normal incidence) to the CDF detector. Early studies indicate that the secondary particle and photon conversion backgrounds from this material are very low and present no problems to the data analysis.

Using the optical survey constants measured during the barrel construction, we observe a residual distribution with a sigma of 18 microns. When tracks are used to align the device in situ, allowing for only simple translations of the individual ladders, the residual distribution narrows to less than 14 microns. This is shown in Figure 2. Such a high quality alignment so early in the data-taking, when the asymptotic resolution is only 10 microns, is a nice reward for the effort spent in the careful design and construction of the SVX.

First indication of displaced vertices can be seen in the SVX event display of Figure 3. This event contains a clearly displaced J/ψ decay with associated tracks on one side and a second displaced vertex on the opposite side. The analysis of such events with bubble chamber-like clarity and micron scale precision will provide significant new physics results. Quantitative analysis of these events has already produced a preliminary measurement of the J/ψ 3D decay length distribution (Figure 4). A clear excess on the positive side is evident. After background subtraction using the side band distribution, a correction (derived from a Monte Carlo study) assuming the J/ψ is from a B decay. The resultant distribution agrees well with the average B lifetime. The decay length distribution in the signal region is also well fit to a sum of prompt J/ψ production and a reasonable fraction of J/ψ's from B decay. B tagging algorithms designed for the top search perform as expected on the J/ψ sample. Studies of jets, which should have a B contamination at the fraction of a % level, can be used as a control sample for the b tagging algorithms. First results indicate that the background rejection expected from Monte Carlo studies is attained in data.

Some effort has gone into using the SVX pulse height information for particle identi-

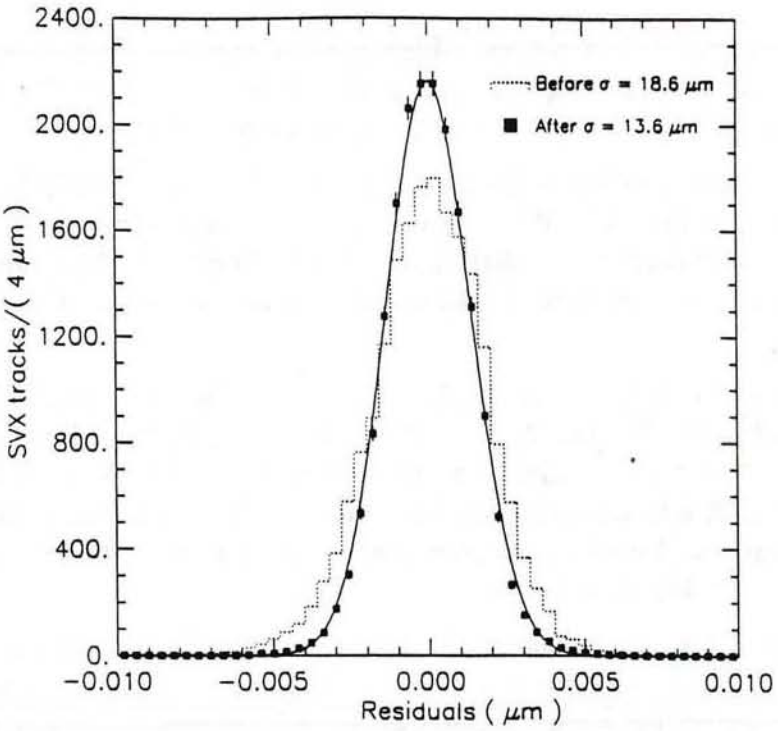

Figure 2: Residual distribution for hits associated with tracks before and after in situ track alignment.

fication. Figure 5 shows the smallest pulse height, from four-hit SVX tracks versus track momentum. Proton and kaon bands are clearly visible. This information may prove useful in B meson and baryon tagging and reconstruction.

To date, the radiation protection system for the SVX is functioning well. The accelerator division has been very cooperative in keeping the dose to the SVX at a minimum. So far no noticeable increase in SVX noise or leakage current, which would indicate radiation damage, has been observed. We estimate (with an uncertainty of about a factor of two) that the inner layer of the SVX has been exposed to about 2 Krads. The radiation dose will be carefully controlled and monitored throughout the CDF data-taking.

Overall, it can already be concluded that the SVX project has been successful. A silicon vertex detector can be installed and operated at the Fermilab Tevatron collider. It is with this understanding and experience that the design and construction of the SVX II detector can proceed with confidence.

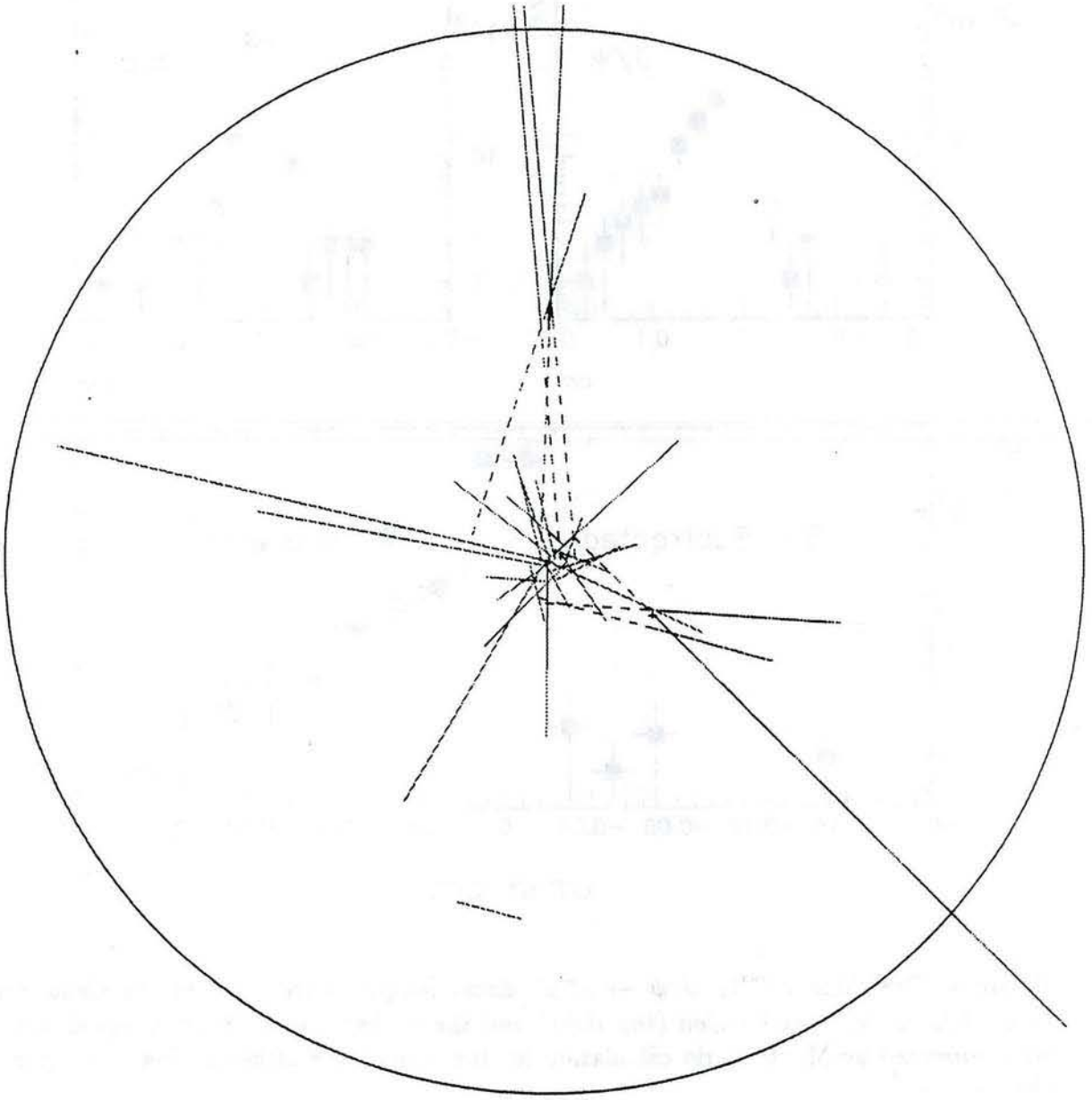

Figure 3: SVX display showing two displaced vertices in a $J/\psi \rightarrow \mu^+\mu^-$ event. The length of the tracks is proportional to their momenta and the J/ψ is in the displaced vertex at the 4 o'clock position.

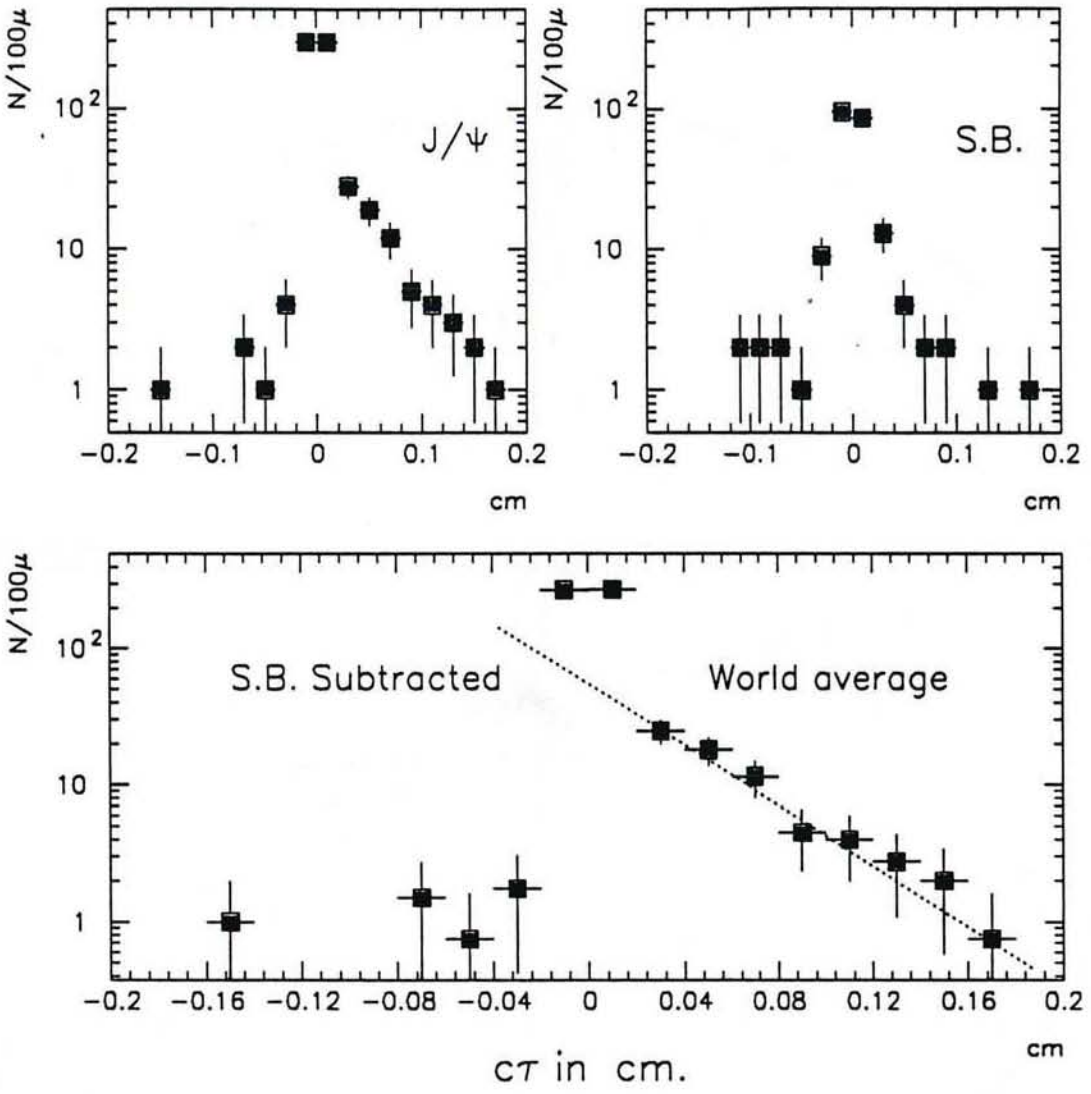

Figure 4: Preliminary CDF $J/\psi \rightarrow \mu^+\mu^-$ decay length distribution in the signal region (top left), the side band region (top right) and the background subtracted signal distribution, corrected by Monte Carlo calculation for the momentum ofthe missing decay particles (bottom).

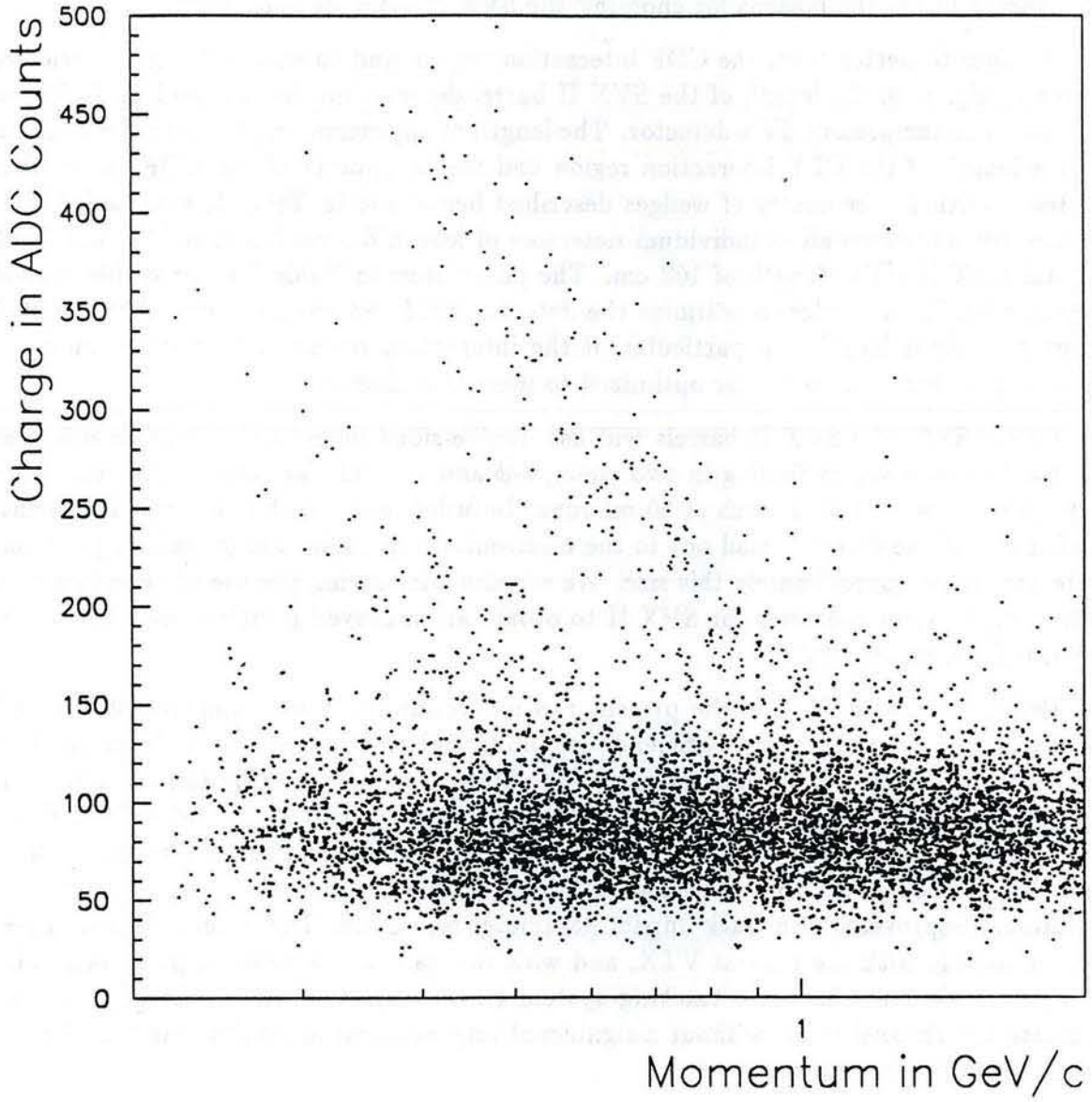

Figure 5: Smallest pulse height versus track momentum in the SVX, showing distinct proton and kaon bands.

3 SVX and SVX II Design Comparison

The two principal contributions to the improved performance of the SVX II Stage 1 barrel detector over the present SVX detector are the increased geometric coverage and the addition of z readout. Table 1 shows a comparison between the SVX and SVX II detector designs. We discuss below the reasons for choosing the SVX II detector parameters.

In order to better cover the CDF interaction region, and to extend the geometric acceptance to higher η, the length of the SVX II barrel detector has been significantly increased compared to the present SVX detector. The length of approximately 1 meter is well matched to the length of the CDF interaction region and the acceptance of the CDF outer tracking system. With the geometry of wedges described below and in Table 1, standard 4 inch diameter silicon wafers allow individual detectors of length 8.5 cm (as in SVX), and result in a total SVX II active length of 102 cm. The parameters in Table 1 assume this individual detector length. In order to optimize the detector yield and cost, we may choose a slightly shorter detector length. In particular, if the interaction region can be made shorter, the SVX II geometry can be better optimized to meet this change.

Unlike SVX, the SVX II barrels will use double-sided detectors to provide information for tracking and vertex finding in two views, r-ϕ and r-z. The amplifier chips will again be 128 channels wide with a pitch of 50 microns. In order to avoid the need for significant fan in/fan out of the detector read out to the electronics, this limits the ϕ readout pitch on the detectors to be approximately this size. We are also considering the use of detectors with an intermediate strip geometry for SVX II to obtain an improved position resolution over the present SVX readout pitch.

Experience using SVX in the present run has confirmed the advantages of having four layers per view for alignment, efficiency (redundancy) and pattern recognition in the high multiplicity hadron collider environment. The inner radius is given by the detector readout pitch and the requirement of an integral number of r-ϕ readout chips and is limited by the accelerator beampipe radius. We are proposing a new 1.0 inch diameter beryllium beampipe for SVX II, compared to the present 1.5 inch diameter pipe used with SVX, to obtain additional improvement in track impact parameter resolution. The outer radius is chosen to be compatible with the present VTX, and with this radius the detector position resolution is well matched to the outer tracking system track projection error. Larger radii would increase the channel count without a significant improvement in track finding efficiency and track parameter resolution.

For SVX II, the silicon microstrip detectors will be mounted onto ladder structures and arranged in twelve azimuthal sectors in each barrel. This is a similar geometry to that used for SVX. The 30° wedge geometry is well matched for detector widths (again quantized in integral number of chips) and to axial cabling schemes, and to the parallel processing used in the Silicon Vertex Tracker (SVT). The SVT will reconstruct tracks in individual detector wedges simultaneously to reduce processing time.

Detector Parameter	SVX	SVX II
Readout coordinates	r-ϕ	r-ϕ;r-z
Number of barrels	2	3
Number of layers per barrel	4	4
Number of wedges per barrel	12	12
Number of ladders	96	144
Ladder length	25.5 cm	34.0 cm
Combined barrel length	51 cm	102 cm
Layer geometry	3° tilt	staggered radii
First layer radius	2.989 cm	2.416 cm
r-ϕ readout pitch (4 layers)	60;60;60;55 μm	60;55;60;55 μm
r-z readout pitch (4 layers)	-	166;111;166;166 μm
Active length of readout channel (r-ϕ)	25.5 cm	17.0 cm
Number of r-ϕ readout chips/ladder (4 layers)	2;3;4;6	4;6;8;12
Number of r-z readout chips/ladder (4 layers)	-	4;6;8;8
Number of readout chips/wedge (r-ϕ;r-z)	15;-	30;26
Number of r-ϕ readout channels	46,080	138,240
Number of r-z readout channels	-	119,808

Table 1: Comparison of the geometrical layout and design parameters of the SVX and SVX II detectors.

In order to allow wedge-to-wedge alignment, adjacent detectors in a layer will overlap by several strips. A small overlap was achieved in SVX by tilting the detectors 3° from tangential. With double-sided detectors, the clearance restrictions for chips and wirebonds would require much larger tilt angles. This is particularly true for the innermost layer which is at a reduced radii compared to SVX. We are therefore considering the use of a staggered radii geometry with a separation of $\sim$7 mm between neighboring ladders to allow greater overlap between wedges without mechanical interference.

In order to minimize the bulkhead support material, yet keep the length of silicon read out per electronics channel sufficiently small (and therefore reducing the amplifier input capacitance and noise), we have chosen a three barrel configuration. Each ladder is composed of four 8.5 cm detectors and is 34 cm in length. Pairs of detectors are wire-bonded together and read out at each end of the ladder, for both the r-ϕ and r-z readout. To minimize the inactive gaps between barrels, the readout electronics will be mounted on hybrids glued onto the detector surface. Only a small gap between barrels will be required for the bulkhead support, cabling, and cooling lines. Mounting the readout hybrids on the detector surface will noticeably reduce the gap between SVX II barrels and improve the geometric coverage compared to SVX.

Given the detector lengths and widths, and chip pitch, there are natural choices for the pitch for the z strips and these are shown in Table 1. We have simulated the detector performance with resolutions corresponding to pitches similar to the ones chosen and find it

to perform well for tracking and vertex-finding in the r-z plane.

SVX II will use an entirely new data aquisition system to operate with beam-crossing times as short as 132 nsec, and provide the digitized analog information in time for level 2 trigger formation. The use of analog information for the present SVX, to find the pulse-height weighted cluster centroid, provides a significant improvement in the resolution. In addition, for SVX II, the use of analog information in centroid finding provides good z resolution for tracks out to high incidence angles (high rapidity). The large number of channels and the need for fast readout speeds, have lead to a design with digitization on-board the front-end chip. Many of the features of this chip, for example the "nearest neighbor" readout scheme, and the desire for a readout threshold which can be set per chip, are based directly on our experience with the present detector. The data aquisition, and the control of the front-end chips will be highly parallel, to reduce the impact of a single component failure. To provide the necessary bandwidth with minimal material and low power consumption, SVX II will use optical fiber transmission from the detector to a VME based DAQ system and the SVT trigger processor. There has been significant R&D on optical readout for SSC experiments, and while this is a relatively new technology, the development appears timely for SVX II.

From our study of the design parameters chosen for the SVX and the experience gained in the SVX construction, we have found that a 4-layer barrel structure with a wedge geometry is a natural choice for SVX II. Several significant improvements will be made, however, when compared to the SVX detector. SVX II will have double the length, z readout, a smaller inner radius, a smaller inactive region between barrels, and a fast DAQ system with trigger capabilities. The staggered radii geometry will simplify the barrel construction and improve the wedge-to-wedge overlap for alignment. These improvements will make the SVX II detector an even more powerful vertex detector than the already successful SVX.

4 Tracking Simulation

4.1 Model Geometries

The geometric design of a vertex detector for CDF is strongly influenced by the long luminous region of the Tevatron. For this study we assume that the extent of the luminous region in z will remain unchanged from current operation (a gaussian with $\sigma_{z_v} = 30$ cm). In order to cover such an interaction region, one is naturally led to a barrel geometry. Considerations such as acceptance for high p_T leptons, and tagging of b jets from top (see section 5.3), and the desire to minimize the material preceeding the CTC in the central rapidity region lead naturally to the conclusion that the length of the barrel should be about $\pm 2\sigma_{Z_v}$. This length fits conveniently inside the present CDF VTX. The considerations that led to the choice of four layers of silicon in the barrel at the radii of the current SVX design remain valid: an inner radius as small as possible to achieve the best impact parameter resolution, given the constraints of the beam pipe diameter and the severe radiation environment; an outer radius as large as the VTX will allow; four layers to allow for redundancy in case of catastrophic loss of a large section of a barrel layer. As discussed below, the outer radius is sufficiently large compared to the inner radius to provide efficient pattern recognition.

There remain two critical design issues:

- measurement of the z coordinate in the barrel,
- tracking and vertexing at large η.

With a barrel of length 102 cm, the detector provides precision vertexing through 4 layers of silicon out to $|\eta| < 2.5$ for tracks originating from the center of the detector (detector η). Due to high track multiplicities, stand alone tracking (pattern recognition) in the SVX II barrel detector is expected to be difficult. For the current run, the tracking algorithm is based on finding a track in an outer tracker, which currently is the CTC. Figure 6 shows the pointing resolution in the azimuthal direction of the barrel detector as a function of the ratio of outer to inner barrel layer radii with the SVX. The corresponding CTC error is 0.6 mR. The choice of the current SVX design, with a ratio of 2.6 for the outer layer and inner layer radii, is seen to be nearly optimal and well matched to the CTC pointing resolution. At high luminosities, the increased track multiplicities make pattern recognition more difficult in the inner CTC superlayers. Changes in the front-end electronics for the CTC are expected to improve the two track resolution by about a factor of two and roughly compensate for the increased track density. Wire aging is not expected to be a problem up to an integrated luminosity of at least 1 fb^{-1}. In this study, we assume that the tracking performance of the CTC will not degrade at high luminosity. However, the CTC single track efficiency drops off sharply for tracks that traverse fewer than 4 super layers, corresponding to a detector η of 1.4. A set of radial disk tracking devices at fixed z from the edge of the barrel (55 cm) out to the CTC end plate (155 cm), with each disk extending out to a radius equal to the inner wall of the CTC (27 cm) is modelled to provide tracking capability at high

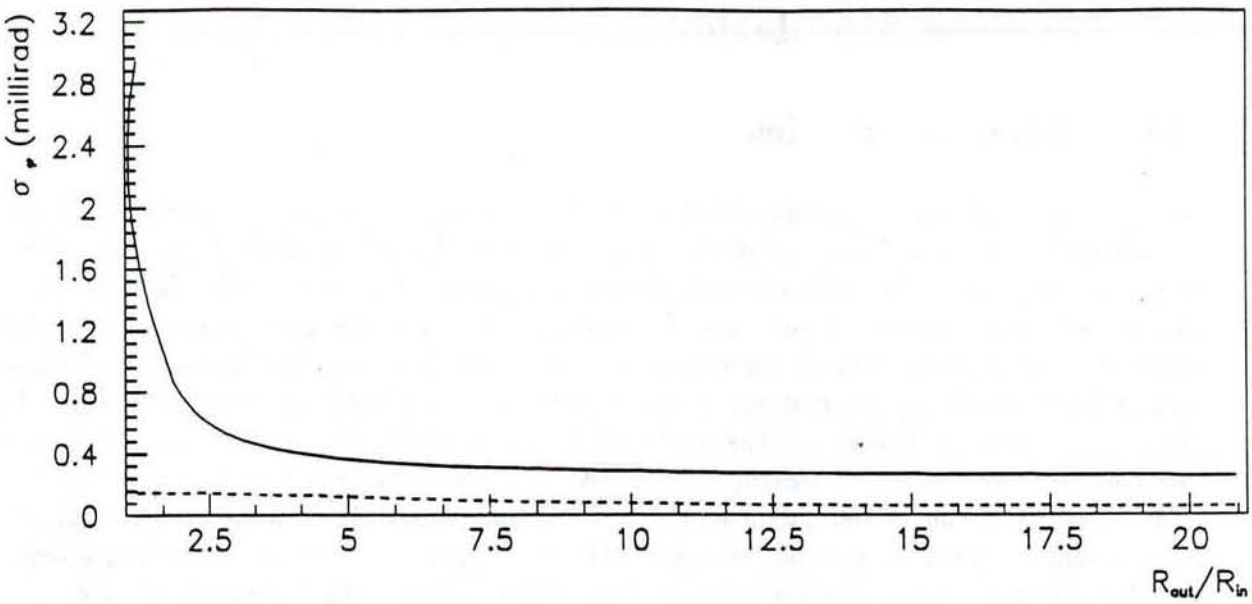

Figure 6: The solid curve is the error on the azimuthal pointing resolution (σ_ϕ) as a function of the ratio of barrel outer to inner radii (R_{out}/R_{in}) using only the SVX. The dashed curve is the same pointing error with the CTC resolution included.

rapidity $1.4 < |\eta| < 2.5$. Candidate technologies for these disks include silicon detectors and gas microstrip detectors. Other geometries, such as layers of axial straw tubes preceeding the CTC can be imagined. One aspect of this study was to first demonstrate the physics motivation for tracking at large rapidity, and for this purpose we take a set of radial disks as an example of how to achieve tracking in this region.

An important consideration in the SVX II design is how a z coordinate measurement can be achieved and how such a measurement supplements the tracking of the CTC. The measurement of the z coordinate in the SVX barrel will improve the single track z resolution by almost an order of magnitude. This will improve the tagging of leptons from heavy flavor decays as well as mass and vertex resolution.

To evaluate the capability of an elongated silicon barrel detector as well as the enhancements of z measurement in the barrel and additional disk devices, we examine five detector geometries:

G1 The present SVX geometry, with measurement of the ϕ-coordinate only. The active silicon covers a total length in z of 51 cm. There is a gap in the coverage at $z = 0$ to allow for support and cable access.

G2 A barrel geometry with 4 layers, similar to the present SVX, but with a total z coverage of 102 cm. This geometry again has measurement of the ϕ-coordinate only.

G3 Same as (G2) but with both ϕ and z information.

G4 Geometry (G2) with a forward tracking upgrade using 6 radial disks spaced in z from 55 to 155 cm and each extending out to 27 cm in radius. The spacing in z has been chosen to enhance the tracking coverage in the CTC plus disk system.

G5 Geometry (G3) with the same disk arrangement as (G4).

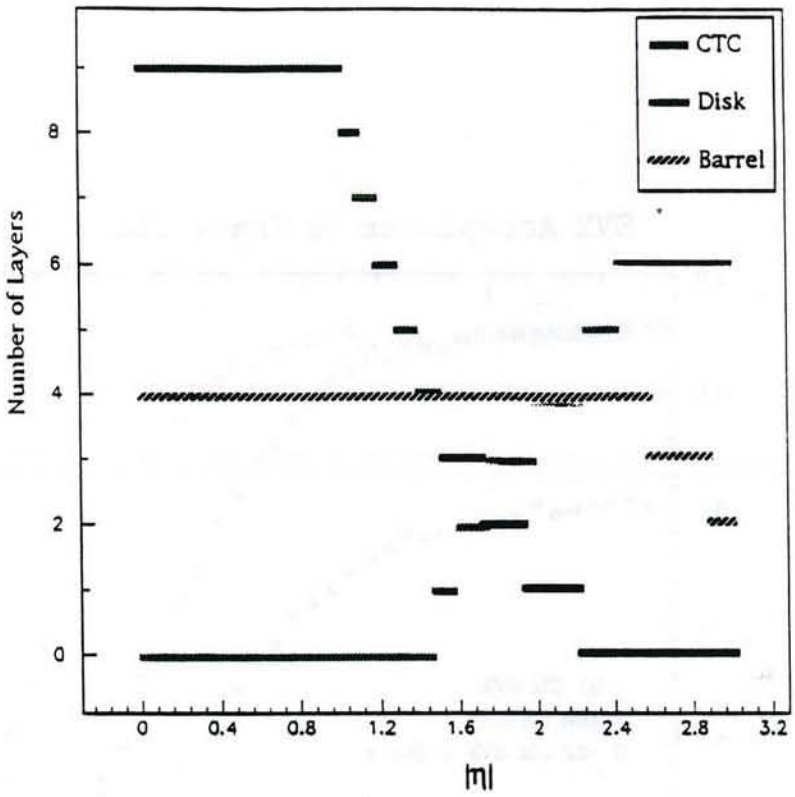

Figure 7: The number of detector elements (layers or superlayers) traversed by a high p_T particle originating at the detector origin vs η.

The acceptance of the CTC, SVX barrel, and radial disks is shown in Fig. 7, where the number of detector elements traversed by a high p_T particle originating at the detector origin is plotted as a function of rapidity. The geometric acceptance for geometries (G1) and (G2) is plotted as a function of rapidity in Fig. 8, where the tracks originate from an interaction point smeared in z with $\sigma_z = 30$ cm. The increase in acceptance for (G2) demonstrates the importance of covering the extended interaction region. The extension of the tracking to larger rapidity provided by a system of radial disks is demonstrated in Fig. 8 as well. The radial disk placement has not been optimized and involves consideration of the other detector elements in the endplug region.

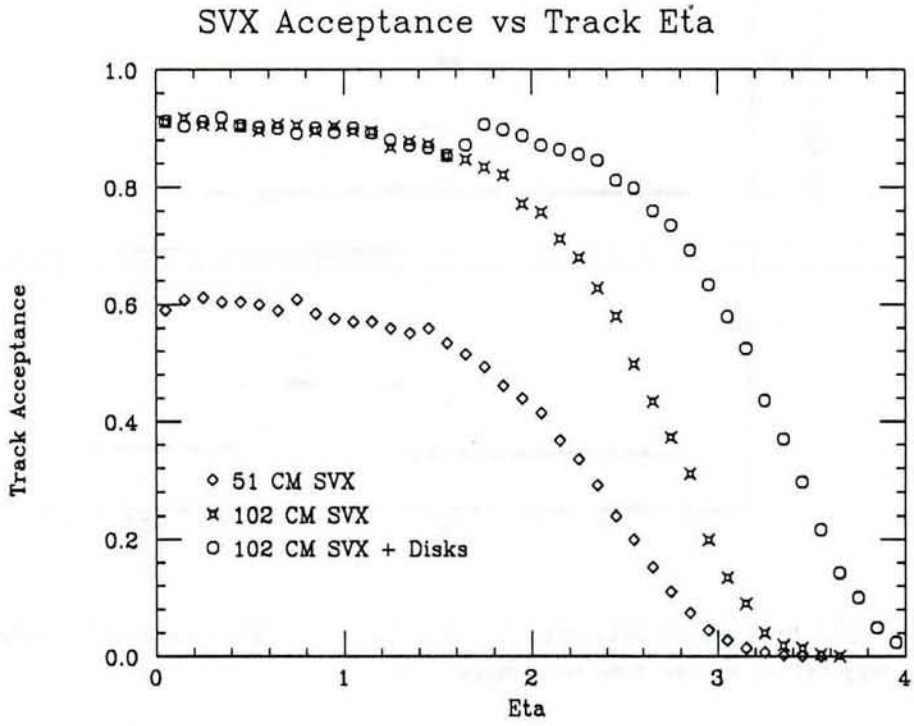

Figure 8: Geometric acceptance for geometries G1 (current SVX barrel length) , G2 and G3 the elongated barrel (2 $\times$ current SVX) , and G4 and G5 the elongated barrel plus disks. The acceptance of the CTC is not included.

4.2 Simulation Tools

Two fast simulation programs were developed to model the geometries G1-G5. The first is the CDF fast detector simulation, QFL, modified for an elongated barrel geometry with both ϕ and z measurements (G1-G3). The second, SVXSIM, is a very fast, easily modified, simulation developed specifically for this study and capable of incorporating the VTX z resolution and radial disks. These simulations share many features. They are based on a covariance matrix calculation technique [2]. As a consequence, any inefficiencies due to pattern recognition are modeled in an ad hoc fashion. In QFL, the CTC efficiency is 100% for tracks with $p_T > 200$ MeV/c traversing at least three CTC superlayers. For SVXSIM, the efficiency per CTC wire layer from the data is used to model an efficiency per superlayer. We require 4 of 12 axial and 3 of 6 stereo wires for a layer to be included in the fit. We then further require some minimum number of axial superlayers plus disks in order for a track to be found in the outer tracker. The absolute minimum is a point-slope measurement: at least one axial superlayer or two disks. More stringent requirements are investigated in the following section on single track results. The CTC error calculation includes efficiencies and resolutions per wire layer from the data. This is known to properly reproduce the CTC errors measured in the data [3]. The material in the barrel is equivalent to the total material in the current SVX plus VTX inner wall, equally distributed in each of the four cylindrical layers. The z measurement resolution is degraded as a function of the angle of incidence α into the silicon according to a parameterization interpolated from calculations done by Luth [4] (see Fig. 9). This parameterization includes the effects of strip pitch (100 μm), the thickness of the silicon layer (300 μm), and the readout signal/noise ratio (12:1). We have studied this resolution in detail, following the work of Luth [4], to determine the effect of strip layout and signal/noise for our design. The results of these studies are summarised in section 7.2 of this document. In SVXSIM the contribution of the VTX to the z resolution is modeled [5] as 16 measurements from a radius of 21 cm down to a radius of 11 cm each with a resolution of 200 μm/$\sin\theta$ (see impact parameter resolution plots in Fig. 10 labeled G1). The disks are idealized tracking elements providing 3D information with resolution comparable to the barrel detector. The r measurement is degraded with the angle of incidence of the track according to the z resolution parameterization given in Fig. 9. The geometry, resolution and material of the barrel and disk detectors are summarized in Tables 2 and 3.

These two simulations have been compared in detail to the CDF full detector simulation, CDFSIM, for G1. We have compared the calculated errors on all five track parameters as a function of p_T and η. The calculations from all three simulation programs are in good agreement. This checks the material model as well as the simulation algorithm. For example, the error on the impact parameter is calculated as 11 μm at high p_T and 44 μm at a p_T of 1 GeV/c. The agreement in our simulation tools is such that further discussion of geometries G1-G5 will be made without reference to the method of simulation.

Table 2: Summary of Barrel Detector Parameters.

Structural element /detector	radius (cm)	$\frac{1}{2}$ length (cm)	thickness[5] (cm)	thickness[5] (%X_0)	σ_ϕ (μm)	σ_z^1 (μm)
Beam pipe	2.60	—	—	0.16	—	—
VTX[2]	11.0-21.0	51.0	—	—	—	200.0
CTC[3]	27.6	155.0	0.10	3.00	—	—
SVX II[4]	3.0, 4.3, 5.7, 7.8	51.0	0.03	0.75	12.0	30

[1]At $\eta = 0$.
[2]16-wire modules.
[3]Inner wall.
[4]Layers 1 – 4.
[5]Thickness of one layer

Table 3: Summary of Radial Disk Parameters.

z (cm)	55.0, 62.5, 70.0, 102.5, 126.5, 150.0
Disk radius (cm)	27.0
thickness (%X_0)	0.75
thickness (cm)	0.03
σ_{ϕ_0} (μm)	15.0
σ_r (μm)[1]	30.0

[1]At $\eta = \infty$

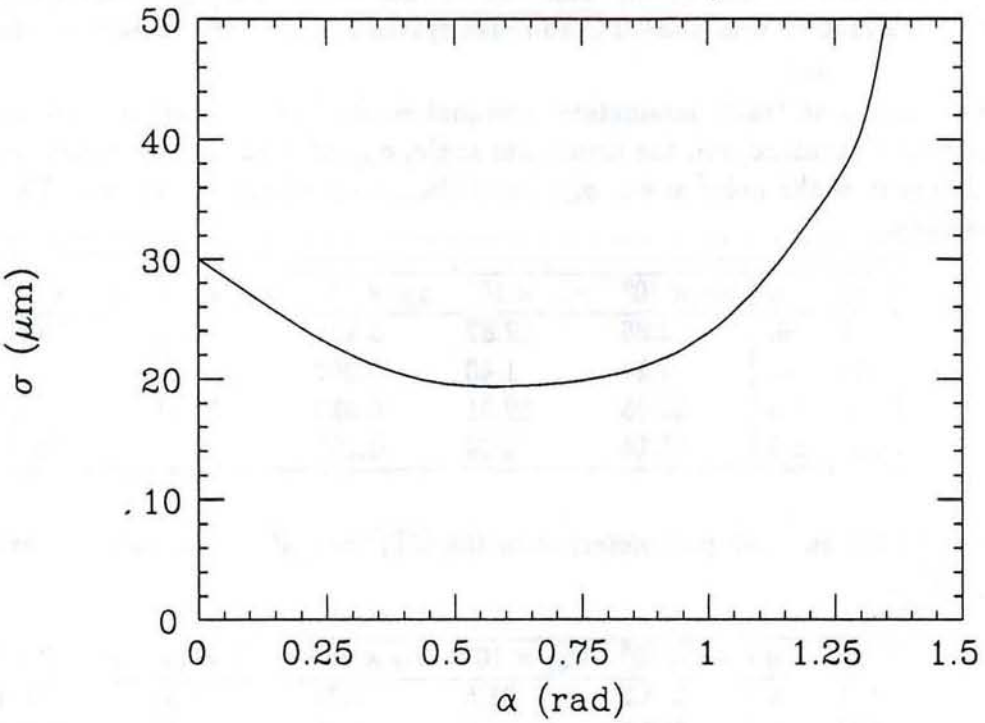

Figure 9: z resolution as a function of angle of incidence α. The parameterization is an interpolation for a thickness of 300 μm, S/N = 12, and pitch = 100 μm.

4.3 Single Track Results

In order to demonstrate the tracking capabilities of the different geometries, we examine the behavior of the transverse impact parameter error (σ_D), z impact parameter error (σ_z), and momentum resolution as a function of rapidity for track p_T of 1 GeV/c and 20 GeV/c. Figures 10, 11, and 12 compare these errors for the different geometries. These plots show the enhanced capability of the elongated barrel, of the elongated barrel with z resolution, and of the high η tracking provided by the disks. We note that the disks allow tracking out to $|\eta| \sim 3.0$. Because the precision of the tracking at large rapidity is limited by the large multiple Coulomb scattering in the barrel detector, the precision of the radial disks is not very significant. Their role is predominantly one of an outer tracking device allowing the track to be found in this region. This can be seen by comparing Tables 4 and 5, the latter being for a situation with the CTC and disk systems having an enlarged resolution. Table 5

Table 4: Errors on track parameters: nominal resolutions. Shown are the track parameter errors in the curvature, σ_C, the azimuthal angle, σ_{ϕ_0}, the transverse impact parameter, σ_D , the cotangent of the polar angle, σ_{cot} , and the z impact parameter, σ_{z_0}. The units are cm and radians.

p_T	η	$\sigma_C \times 10^6$	$\sigma_{\phi_0} \times 10^4$	$\sigma_D \times 10^2$	$\sigma_{cot} \times 10^3$	$\sigma_{z_0} \times 10^1$
1	0.	2.86	12.82	0.431	1.54	0.060
100	0.	1.24	1.43	0.097	0.38	0.027
1.	2.5	21.05	29.91	0.913	17.71	0.527
100	2.5	11.14	3.04	0.155	0.82	0.048

Table 5: Errors on track parameters with the CTC and disk resolution increased by a large factor (10^5).

p_T	η	$\sigma_C \times 10^6$	$\sigma_{\phi_0} \times 10^4$	$\sigma_D \times 10^2$	$\sigma_{cot} \times 10^3$	$\sigma_{z_0} \times 10^1$
1	0.	313.2	31.5	0.76	1.54	0.060
100	0.	228.0	25.1	0.63	0.40	0.028
1.	2.5	615.7	56.3	1.28	17.71	0.527
100	2.5	228.1	25.1	0.63	1.18	0.064

shows that the resolution in σ_{z_0} is almost unaffected by making the measuring errors in the outer tracker very large. In the case of σ_D there is some increase but it is due primarily to the increase in the curvature error caused by the loss of the outer tracker.

The amount of material traversed by a track as a function of rapidity is shown in Fig. 13 for the different geometries. Here we clearly see the predominance of the large path length in the barrel detector at large rapidity.

The utility of covering the elongated interaction region with the barrel detector was demonstrated in Fig. 8. When radial disks are included, geometries G4 and G5, the single track acceptance is $> 80\%$ for tracks produced anywhere along the interaction region out to

a track rapidity of ~ 2.5. For the disks, the relevant question is one of efficiency at large rapidity. Without doing a detailed simulation it is not possible to completely model the single track efficiency due to pattern recognition in the complete outer tracker of CTC plus disks. In order to evaluate what kind of efficiency can be achieved, we calculate the single track efficiency for tracks produced with a Gaussian distributed z position under different assumptions on the capability of the outer tracking system. We require some minimum number of CTC super layers (N_{ctc}) to be traversed by the track, or some minimum number of radial disks (N_{dsk}). Figure 14 shows the single track efficiency as a function of η for three cases: (1) $N_{ctc} > 2$ OR $N_{dsk} > 3$, (2) $N_{ctc} > 2$ OR $N_{dsk} > 4$, and (3) $N_{ctc} > 4$ OR $N_{dsk} > 3$. In each case the track was required to traverse at least two SVX barrel layers. These plots serve to emphasize the importance of the outer tracker performance for tracking at high rapidity. In this study we assume the efficiency as in case (1) of our model.

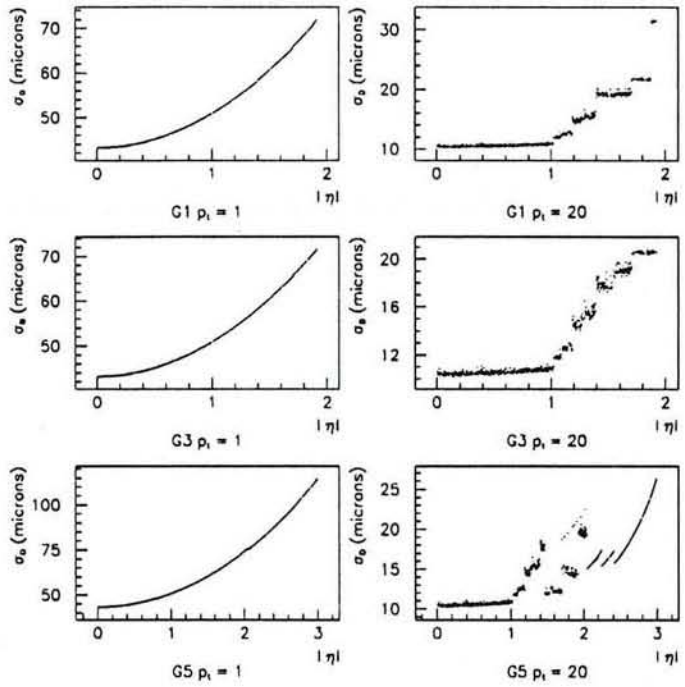

Figure 10: σ_D vs η for G1, G3 and G5 for tracks from $z = 0$. (Note horizontal scale change for G5 plot.)

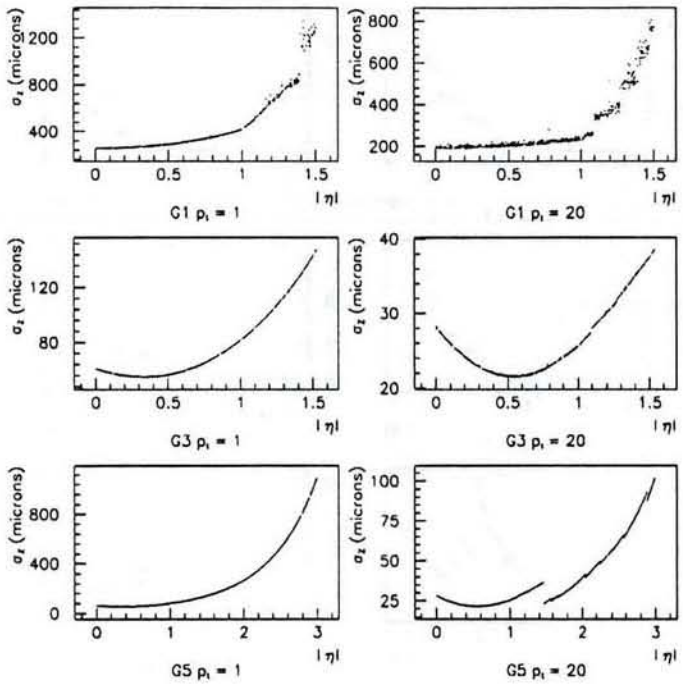

Figure 11: σ_z vs η for G1, G3 and G5 for tracks from $z = 0$. (Note horizontal scale change for G5 plot.)

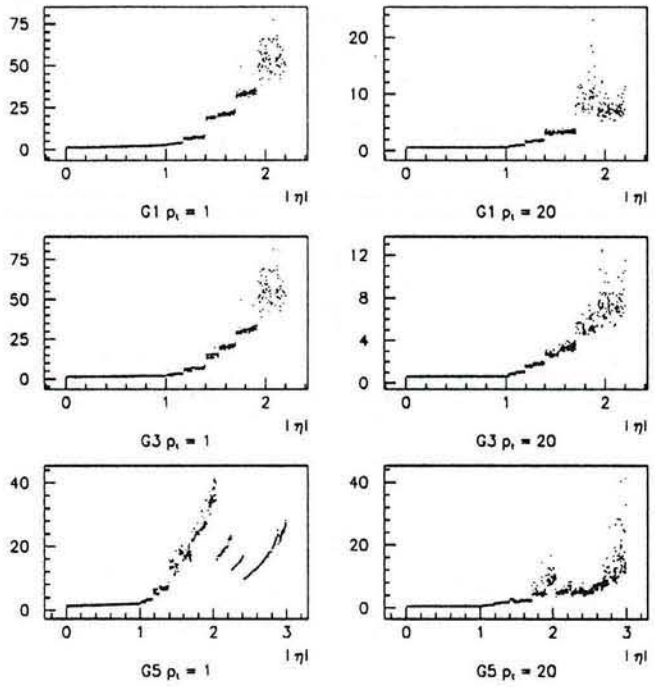

Figure 12: $\delta p_t/p_t^2/.001$ vs η for G1 G3 and G5 for tracks from $z = 0$. (Note horizontal scale change for G5 plot.)

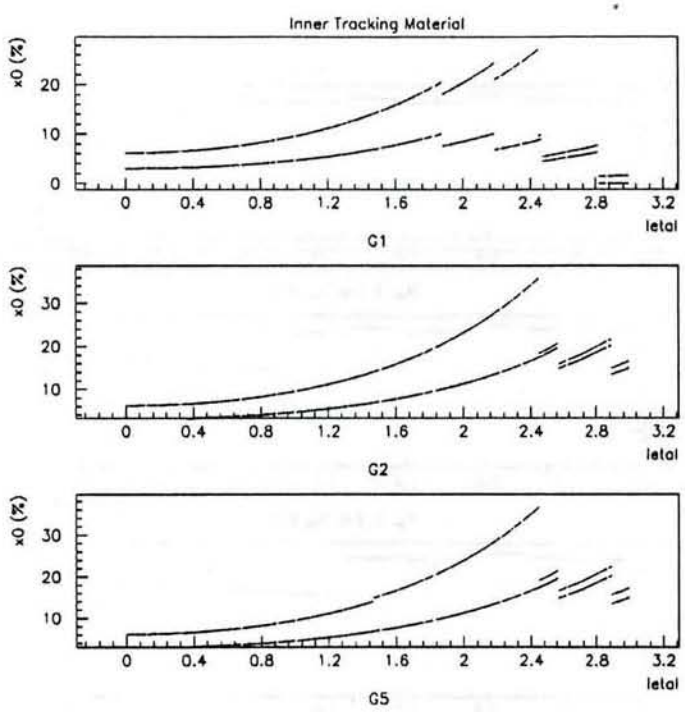

Figure 13: Material traversed vs η in G1, G2 and G5 from the SVX barrel (lower curve) and from all material preceeding the CTC (upper curve). The ordinate is in units of percent of a radiation length.

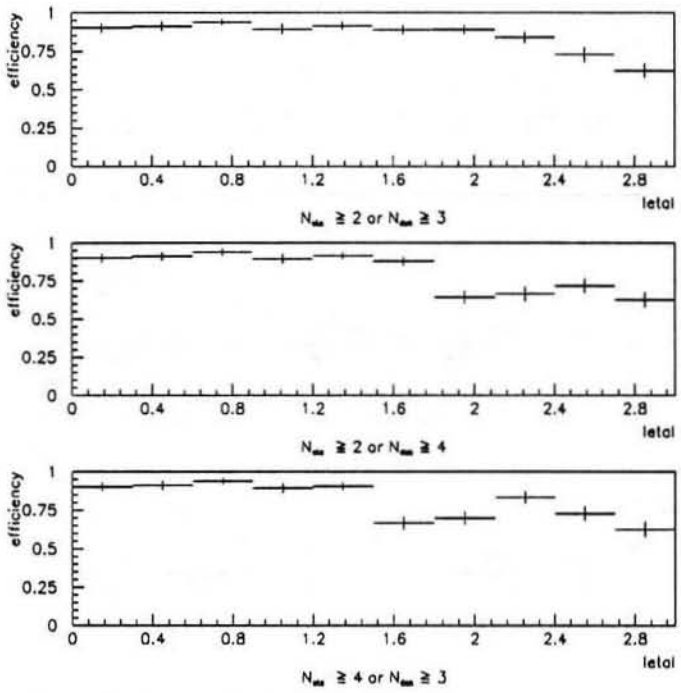

Figure 14: Single track efficiency vs η for three cases.

5 Physics Simulation

5.1 Physics Motivation

Top Physics

The discovery and subsequent study of the top quark are major goals for the collider program. Top production at the Tevatron is expected to be dominated by the production of $t\bar{t}$ pairs. In CDF, top events have been searched for with the following event signatures that require high p_T leptons plus neutrinos and jets: $t\bar{t} \rightarrow l - \nu - jets$ and $t\bar{t} \rightarrow 2l - \nu - jets$. The present lower bounds from CDF place $m_t > 91$ GeV/c^2 assuming Standard Model decay modes [6]. Within the Standard Model, electro-weak measurements limit $m_t < 200$ - 225 GeV/c^2 [7, 8]. If the top quark falls within this mass range, a top signal should be visible in both the $t\bar{t} \rightarrow l - \nu - jets$ channel and in the $t\bar{t} \rightarrow 2l$ channel with the luminosity expected this decade. The expected reconstructed event yields in CDF for the channels $e/\mu - \nu - jets$ and $e - \mu$ are given in Table 6 [8] for an integrated luminosity of 1 fb^{-1}.

Table 6: Expected reconstructed top event yields in CDF as upgraded for Run II with a 1 fb^{-1} run. The reconstruction requires $p_T(l) > 20$ Gev/c, $p_T(jet) > 15$ GeV/c, $|\eta_l| < 1$, $|\eta_{jet}| < 2$, and missing $E_t > 20$ GeV. Yields are given as a function of m_t. Yields for $t\bar{t} \rightarrow l$+4 jets events assume a b tag efficiency per event of 50%; for the e-μ channel there is no b tag requirement.

m_t (GeV/c^2)	e or μ + b jet + 3 jets	e - μ
120	1380	240
140	850	98
180	260	24
210	140	12
240	60	5

Top Discovery

The cleanest signal for top will be the observation of two high p_T leptons from the semileptonic decays of both the t and $\bar{t}$ quarks. The $t\bar{t} \rightarrow 2l$ channel has a background from the direct production of W^+W^- pairs that subsequently decay leptonically. This background exceeds the top signal for values of $m_t \geq 160$ GeV/c^2 as shown in Fig. 15 [8]. The W pair background can be controlled by adding the requirement of high p_T jets in the event, and/or by the requirement of a b tag in the event. The presence of a tagged B meson suppresses the W pair background and provides strong evidence for the top interpretation.

Because the branching fraction of $W \rightarrow e/\mu + \nu$ is 2/9, only 4/81 of the $t\bar{t}$ events decay

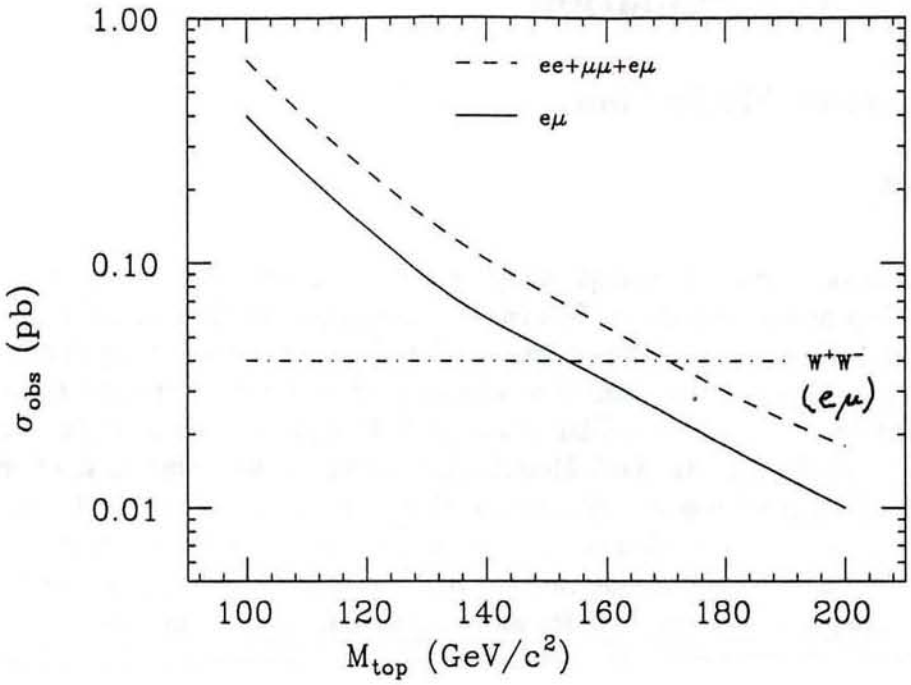

Figure 15: Cross section for high p_T dileptons from the direct production of W^+W^- pairs and from the production of $t\bar{t}$. The top production is shown as a function of the top mass: m_t. The cross sections include CDF detector efficiencies.

via the $2l$ channel. By comparison, the fraction of top events with one of the t quarks decaying semileptonically (the trigger e/μ) and the other hadronically is 24/81. The larger branching fraction for the $t\bar{t} \rightarrow l - \nu - jets$ channel is important to extend the top search to high masses. The $l - \nu - jets$ channel is needed both to search for anomalous top decays and for the measurement of the top mass. Backgrounds in this channel from $W+ \geq 3$jets are significant as shown in Fig. 16 [8, 9]. These backgrounds can be controlled by requiring ≥ 3 high p_T jets, (or ≥ 4 high p_T jets for large m_t), and by requiring a b tag.

Top Mass Measurement and Related Analyses

An excess of $2l$ and/or $l - \nu - jets$ events in CDF will provide evidence for top, and strong support for the discovery of top is the demonstration of the $t \rightarrow b$ decay. Standard Model studies, including the measurement of the branching fraction for $t \rightarrow W + b$ and the measurement of m_t, and searches for deviations from the Standard Model [10], require the largest possible data samples in both data channels: $t\bar{t} \rightarrow l - \nu - jets$ and $t\bar{t} \rightarrow 2l$.

One example of Standard Model tests is the comparison of the event rates for $t\bar{t} \rightarrow 2l$ and $t\bar{t} \rightarrow l - \nu + jets$. Deviations from the expected ratio of $2l$ to $l - \nu - jets$ events of 4/24 would signal new physics. For a b tag efficiency/event $>>1/6$, the estimated reconstructed event yields shown in Table 6 indicate that a $\sim 10\%$ statistical precision can be achieved for

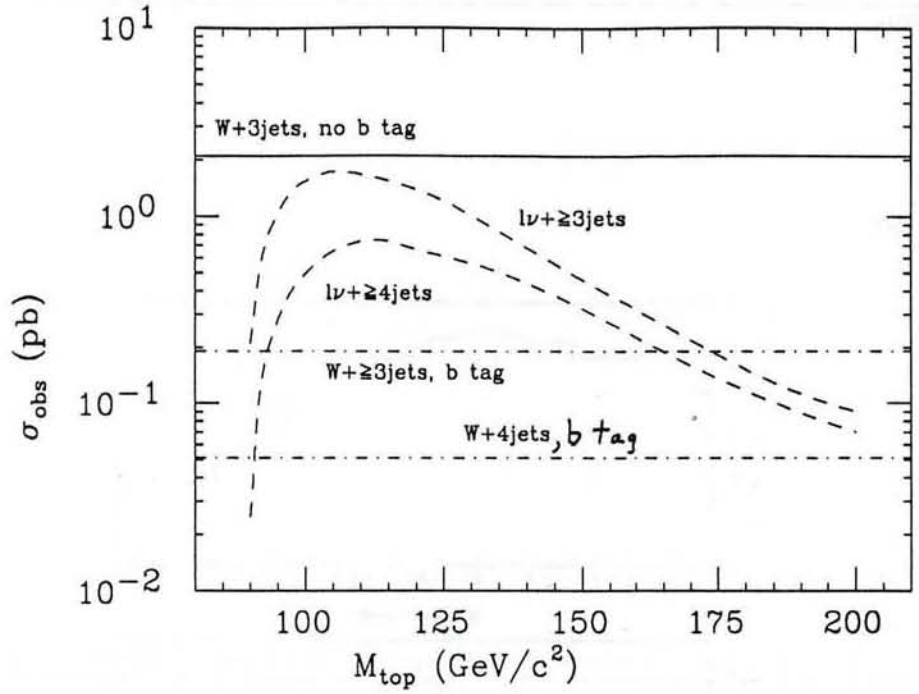

Figure 16: Cross section for $t\bar{t} \rightarrow l - \nu - jets$ as a function of top mass: m_t. The cross sections for W + njets is shown without and with a b tag. Jets and leptons were selected with (E_t, η_{max}) values ($\geq$ 15 GeV, 2.0) and ($\geq$ 20 GeV, 1.0) respectively.

this measurement for $m_t \leq 140$ GeV/c^2.

Simulation studies have been done to evaluate the measurement precision of m_t by CDF using the $l - \nu - jets$ channel. W bosons are reconstructed using 2-jet invariant mass combinations consistent with m_W and by constraining the $l-\nu$ mass to m_W. The precision on measuring m_t is limited to $\sim$ 5 GeV/c^2 from a combination of jet energy scale uncertainties, combinatoric backgrounds, and backgrounds from the underlying event [8]. The statistical precision is estimated to be $\sim$ 30 GeV/c^2 / $\sqrt{N_{ev}}$. Based on the numbers of events in Table 6 the statistical precision should not dominate the measurement of m_t unless the b tag efficiency is significantly less than 50%.

As noted above, b tagging is needed for the effective use of the $t\bar{t} \rightarrow l - \nu - jets$ events. b tagging in CDF relies on either a lepton tag (from the semileptonic decay of the b) or on the identification of a displaced decay vertex with the SVX. The lepton tagging efficiency per B is $\sim$ 10%. This almost meets the minimal requirements of the m_t and top branching fraction measurements. This efficiency is insufficient to extend the m_t measurement to the highest top masses or to effectively tag $> 1B$ per event as needed in searches for possible deviations from Standard Model decays of the top. With the SVX upgrade the tagging efficiency per B will be significantly increased. In the simulation section we present the results of a simulation of top decays to compare the b tag efficiency for the present SVX and for the proposed SVX

II upgrades.

B Physics

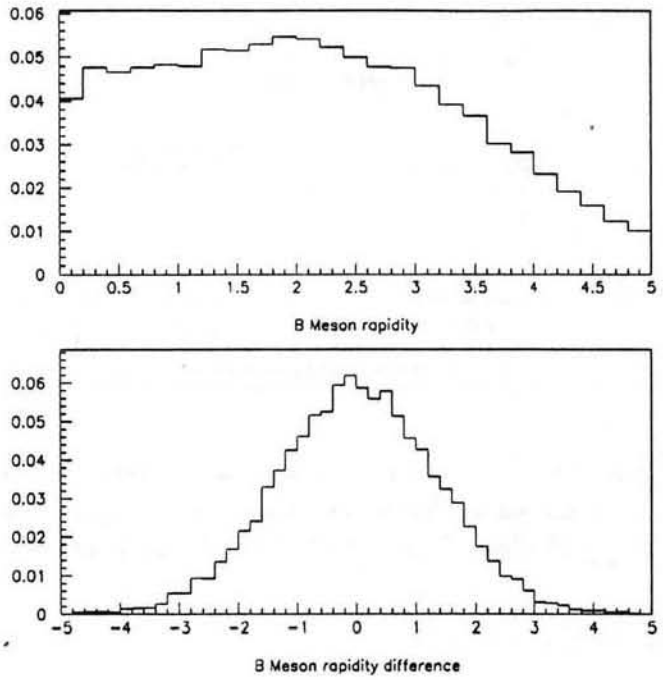

Figure 17: Rapidity distribution of B particles, and the difference in rapidity for the B and $\overline{B}$ (generated by ISAJET).

By mid-decade CDF will have reconstructed several thousand exclusive decays in ψK^+, ψK^* and other similar modes. A large fraction of these will have reconstructed secondary vertices using the SVX or SVX'. Several hundred $B_s \to \psi\phi$ decays, several tens of $\Lambda_b \to \psi\Lambda$, and a few tens of $B_c \to \psi\pi$ are expected in Run I. This is in addition to several million inclusive semileptonic B decays. These samples will allow cross section and $B\overline{B}$ correlation measurements, B spectroscopy and rare decay measurements, lifetime measurements to $< 5\%$ statistical error for B^+ and B^0, and studies of b flavor tagging. Substantial improvements to the above analysis are possible by increasing the acceptance for b flavor tagging, by providing three dimensional vertexing, and by implementing a level 2 secondary vertex trigger.

The kinematics for B's in $b\bar{b}$ events are very different from those in top events. The B's in $b\bar{b}$ events populate a broad distribution in rapidity. The rapidity correlation between the B and $\overline{B}$ is weak as shown in Fig. 17. In addition, the B's have a soft p_T distribution (see Fig. 18) with an average $p_T \sim 5$ GeV/c.

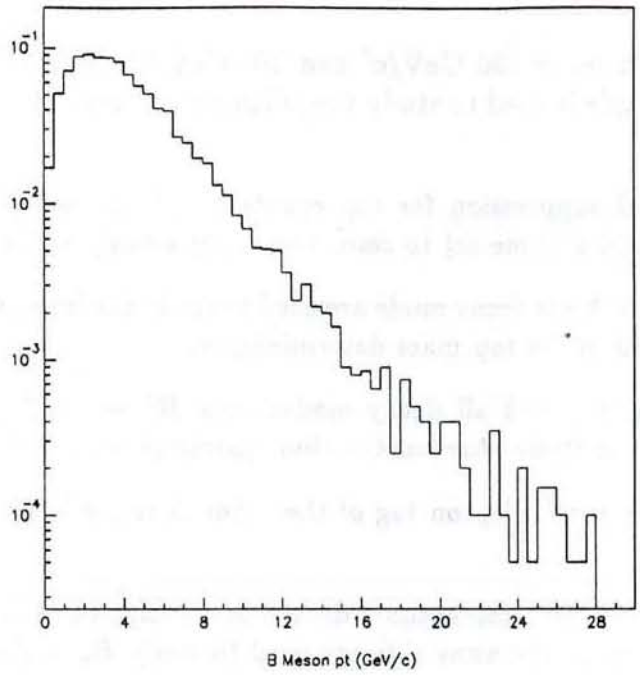

Figure 18: p_T distribution for B mesons (generated by ISAJET).

Important considerations for enhancing b physics in CDF include the following. The low p_T of the B daughter particles means that good position resolution at the vertex requires that the multiple scattering in the SVX II, and thus the material, be kept to a minimum. This requirement is also important in order to minimize photon conversion background to the inclusive electron trigger. The need to partially reconstruct both B particles for some physics topics implies that the detector should cover a large continuous rapidity range. With upgrades, CDF will have essentially continuous electron and muon coverage for $|\eta| < 3$. For the purposes of this document, we assume that CDF will have an effective tag for leptons (electrons and muons) for $p_T > 2$ GeV/c for $|\eta| < 3$. Maximizing the B signal to background for completely reconstructed decays requires good mass resolution over most of this rapidity range. Finally, while many CDF detector requirements for b physics and top physics differ, we will show that the need to provide vertex tracking over the extended interaction region at the Tevatron results in a conceptual design for SVX II that performs well for both b and top physics.

5.2 Physics Benchmarks

We use several physics measurements as benchmarks to evaluate the performance of the detector geometry options. These modes have been chosen both as generic measurements

for a vertex tracking device as well as being modes of physics interest. We have generated the following physics processes with ISAJET:

1. Top events with $m_t = 130$ GeV/c^2 and 200 GeV/c^2, with all decay modes for the t and $\bar{t}$. This sample is used to study the efficiency for tagging the b decay vertex in top events.

2. The background suppression for top events is studied using the $m_t = 130$ GeV/c^2 sample with the b lifetime set to zero, and using a sample of events with $W+$ 4 jets.

3. $t\bar{t}$ in the lepton + 4 jets decay mode are used to study the improvements in combinatoric background, and in the top mass determination.

4. Inclusive B decays, with all decay modes, and $B^0 \to \psi K_s^0$ and $B_s \to \phi\psi$ exclusive decays are used to study B reconstruction, geometric acceptance, and mass resolution.

5. The ψK_s^0 mode, with a lepton tag of the other B is used in CP violating asymmetry studies.

6. $B_s \to \ell\nu D_s; D_s \to \phi\pi$ semi-leptonic decays and exclusive $B_s \to D_s 3\pi; D_s \to \phi\pi$, both with a lepton tag on the away-side are used to study B_s mixing.

All these modes are used to evaluate the general performance of the different geometric models in terms of acceptance as well as mass and vertex resolution. The discovery of the top quark, and measurement of its properties is the highest priority of the CDF physics program. The B_s mixing and CP violating asymmetry studies are used as a relative measure of the ability of the detectors to reach the longer term b physics goals. The B_s measurement [11] requires both flavor tagging and precise vertex-momentum information to extract the time evolution of mixed B_s decays. The CP violating asymmetries require efficient lepton tagging and maximum acceptance.

5.3 Top Analysis

b Tagging Efficiency

b tagging for top decay was studied for top masses of 130 GeV/c^2 and 200 GeV/c^2. For each top mass 1000 $t\bar{t}$ events were generated for each of the three geometries, G1 thru G3, discussed in section 4.1. In addition the top sample at 130 GeV/c^2 was studied for the geometry G5. The p_T of each top quark was required to be greater than 5 GeV/c. The b tagging algorithm consisted of three cuts: (a) tracks are within a cone of radius R=0.4 in η-ϕ space centered on the generated B direction,[1] (b) tracks with impact parameter significance $\frac{D}{\sigma_D} > 3$, (c) tracks with $p_T > 1$ GeV/c. In the case of the double-sided geometries G3 and G5,

[1]We also studied the case of any three tracks within an η-ϕ cone of radius 0.4 of each other disregarding any information about the B direction (see the ϵ_3 column of Table 7.)

the impact parameter cut was replaced by a 3D displaced track cut $\sqrt{(D/\sigma_D)^2 + (Z/\sigma_Z)^2} \geq 3$. Any event with three or more tracks that passed all the cuts was taken as having a b tag.

Tracks from the 130 GeV/c^2 top data sample were used to study the effect of these cuts. The results are shown in Fig. 19 which plot the R, D/σ_D, and p_T distributions respectively for tracks originating from B decay or B decay daughters and for tracks with non-B decay origins. The G2 geometry was used for these plots. Before the cuts the ratio of the number of tracks from B decay to the number of tracks with a non-B decay origin is ≈ 0.1. The cumulative effect of the three cuts is to change this ratio to ≈ 50, a relative enhancement of signal to background of ≈ 500.

Table 7: b tagging efficiencies for $m_t = 130$ and 200 GeV/c^2. The efficiencies have a statistical uncertainty of 1.5%

$m_t = 130$GeV/c^2			
Model	ϵ_1(%)	ϵ_2(%)	ϵ_3(%)
G1	27	27	30
G2	46	44	50
G3	57	55	63
G4		45	
G5		59	
$m_t = 200$GeV/c^2			
Model	ϵ_1(%)	ϵ_2(%)	ϵ_3(%)
G1	41	41	45
G2	60	58	64
G3	68	66	73

The results for the b tagging efficiency are shown in Table 7. The three columns, labelled ϵ_1, ϵ_2, and ϵ_3 respectively, correspond to the tagging efficiencies under the following conditions: (ϵ_1) any track can be used provided it passes the three cuts, (ϵ_2) all three tracks must have a B decay origin, (ϵ_3) the same as (ϵ_1) but the Monte Carlo B direction is not used in making the R cut. The cone cut was made with respect to the Monte Carlo B direction in the case of ϵ_1 and ϵ_2. For the calculation of ϵ_3 any three tracks with R less than 0.4 of each other are accepted. Only ϵ_3 corresponds to the experimentally realistic situation. The small differences between the three cases are an indication of the effect of background tracks and of the uncertainty of not knowing the direction of the B.

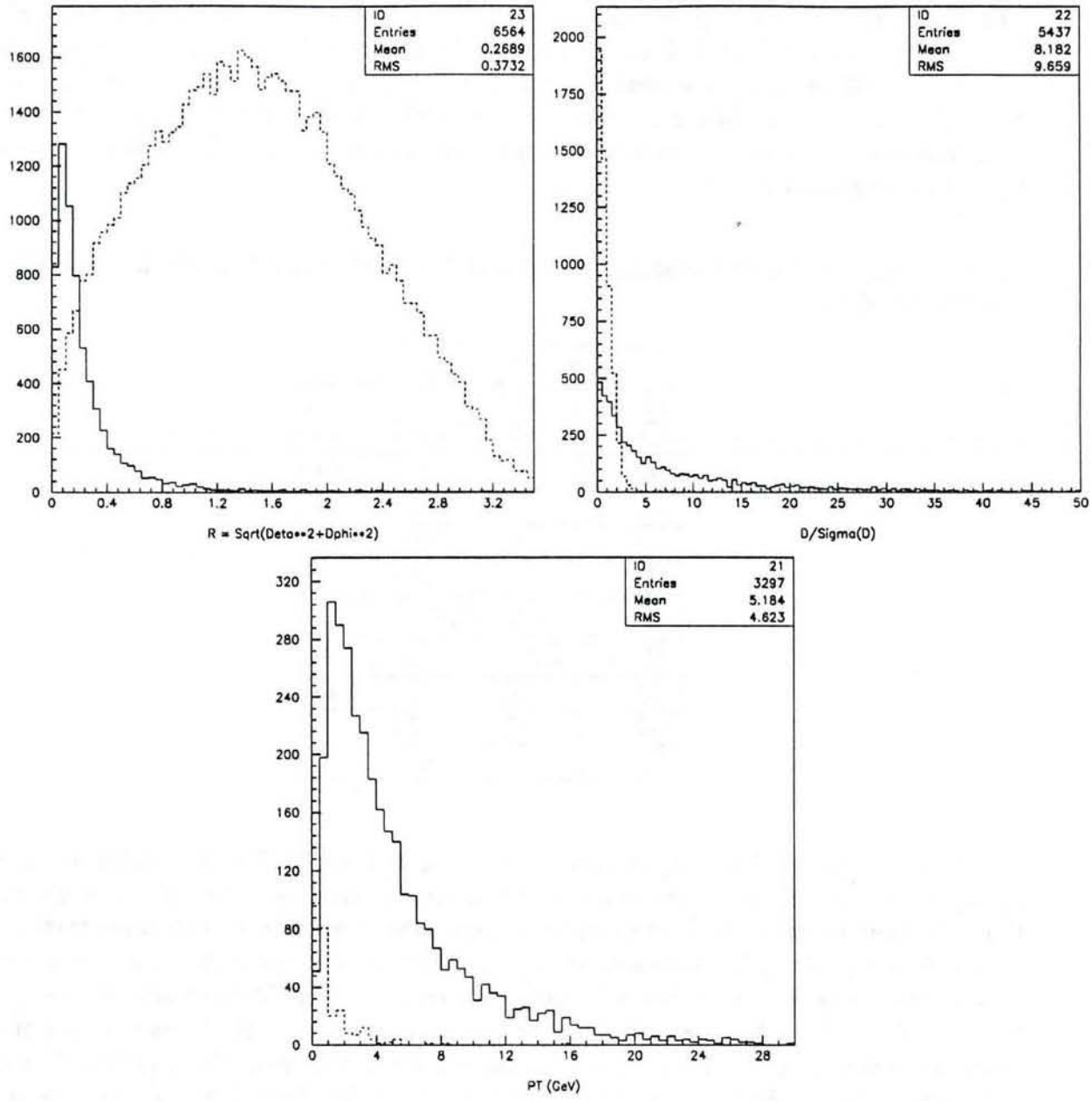

Figure 19: Shown are the distribution of ΔR with respect to the B direction, D/σ_D and p_T for tracks from B decay and B daughter decay (solid) and non-B decay (dashed).

We investigated the background by looking at the 130 GeV/c^2 top sample with the B lifetime (but not the charm lifetime) set to zero, and by studying a sample of $W+$ 4 jet events. With the B lifetime set to zero, 5% of the events are tagged due to the charm decay for model G1. For the $W+$ 4 jet sample the tagging efficiency is 0.2% but this is artificially low because there is no bottom or charm generated. To estimate the effect of this absence of b and c we considered the following. The minimum jet p_T is 8 GeV/c, and for a gluon jet an estimate of the gluon splitting into a $c\bar{c}$ pair is $\approx$ 3%[12]. If we assume 3 gluon jets per event, then 9% of the events have charm and we can expect to tag 5% of these or 0.45%. If we add the 0.45% to the 0.2%, then the background rejection factor is $\approx$ 150. Since 27% of the events produced a b tag originally, this gives an enhancement of signal to background of $\approx$ 40. These results are for 2D vertex information, and are very similar for the long barrel option G2. Depending on the analysis cuts used, we expect that even larger enhancement factors are possible with 3D vertex information.

For the models studied the biggest increase in b tagging efficiency comes from doubling the length. The effect of going to double-sided detectors is less dramatic. The increase depends on the top mass. For a top mass of 130 GeV/c^2 the b tagging efficiency increased by a factor of 1.6 in going from G1 to G2 and by a factor of 1.3 in going from G2 to G3. The corresponding factors for a top mass of 200 GeV/c^2 are 1.4 and 1.1 respectively, and this is to some extent due to the fact that the G1 efficiency is much higher for m_t = 200 GeV/c^2 than m_t = 130 GeV/c^2. It should be pointed out that we have not fully investigated all of the advantages of double-sided detectors. For example, in the case of 3D tracks it is possible to form vertices with two tracks which are true vertices, whereas, fake vertices are more of a problem with 2D tracks. This needs further investigation. Finally because of the central nature of top events, the addition of disks does not improve b tagging for top decay.

Top Mass Measurement

We have studied the impact of the SVX II design on the measurement of the top mass. The top mass can be obtained from the lepton (e or μ) plus jets channel. Because of its capability to tag one or both b jets from the produced $t\bar{t}$, the SVX II is a useful tool both in suppressing backgrounds from W plus jet events and in reducing combinatorial backgrounds. These combinatorial backgrounds, although reduced, still remain because one cannot identify with high probability which b jet is associated with the W decaying to lepton and neutrino. One can also consider to what extent the SVX II b tag will improve the mass resolution of the measurement.

We considered a sample of lepton plus 4 jet events corresponding to an integrated luminosity of one fb^{-1} and a top mass of 130 GeV/c^2. We applied the following cuts: (1) lepton $p_T > 15$ GeV/c and $|\eta| < 1.2$; (2) Missing $E_T > 15$ GeV; (3) two non-b jets have an invariant mass between 60 and 101 GeV/c^2, $E_T(j1) > 30$ GeV and $E_T(j2) > 10$ GeV; (4) b jet $E_T > 10$ GeV. Lepton plus 3 or more jets can also be considered but such a sample from pure $t\bar{t}$ events was only about 20% larger and gave no additional insight into the measurement.

We can form a top by combining the b jet with either the W decaying hadronically or

Table 8: Relative sample sizes for SVX and SVX II Stage 1 for lepton plus 4 jets for approximately 1 fb^{-1} and $m_t = 130$ GeV/c^2. The data in the two columns are from different Monte Carlo samples.

	SVX (G1)	SVX II (G3)
No b tag	1973	1936
One b tagged	524	945
Two b's tagged	56	129

the W decaying leptonically. We take the missing E_T as the neutrino p_T and obtain its z component by a W mass constraint of the lepton with the neutrino. In general there are two solutions. We considered both of them. Then the jets assigned as b jets are tried with each W. The non-b jets are required to pass the W-mass cut (cut (3) above). In order to reduce the combinatorial background, we select the combination with the minimum difference of the reconstructed top masses. Figure 20 shows the reconstructed invariant top mass from the lepton side of the event for the SVX II in three cases: Where the SVX II b tag is not used, where one of the jets has a b tag, and where two jets have a b tag. The sequence for the purely hadronic side is similar. The mass resolution remains approximately constant because the top mass resolution is determined by the jet energy resolution from calorimeters. The sequence indicates some decrease in the combinatorial effects. The number of events in each plot for both the SVX II case (Fig. 20) and the present SVX (not plotted) is shown in Table 8. The SVX II increases the single b tag efficiency by 80% and the double b tag efficiency by 130%. This will help determine the top mass with less data.

We noted that a background for a top mass measurement is W plus jet events. Without a b tag, the signal to background ratio is about 1:1 for $m_t = 130$GeV/c^2. With a single b tag, it improves to about 10:1. The double b tag should yield a cleaner signal. However, it would require a very large amount of data to make it useful. On the other hand, the $t\bar{t}$ cross section decreases rapidly as the top mass goes up. Therefore, in the case of a really heavy top, a double b tag would become much more important.

5.4 Impact on W and Z Physics

As demonstrated by the present SVX, the vertex detector improves the tracking resolution which will help the W and Z physics analysis. At present the transverse mass resolution is 4.6 GeV/c^2 for $W \to e\nu$ and 5.1 GeV/c^2 for $W \to \mu\nu$. The muon momentum resolution improves by 40% and as a consequence the $W \to \mu\nu$ transverse mass resolution will be 4.4 GeV/c^2, making it competitive with the $W \to e\nu$ channel. The improved tracking resolution will also help the Z p_T measurement.

The Stage 2 disk system will also extend the tracking coverage to the forward region, which is crucial for the W asymmetry measurement.

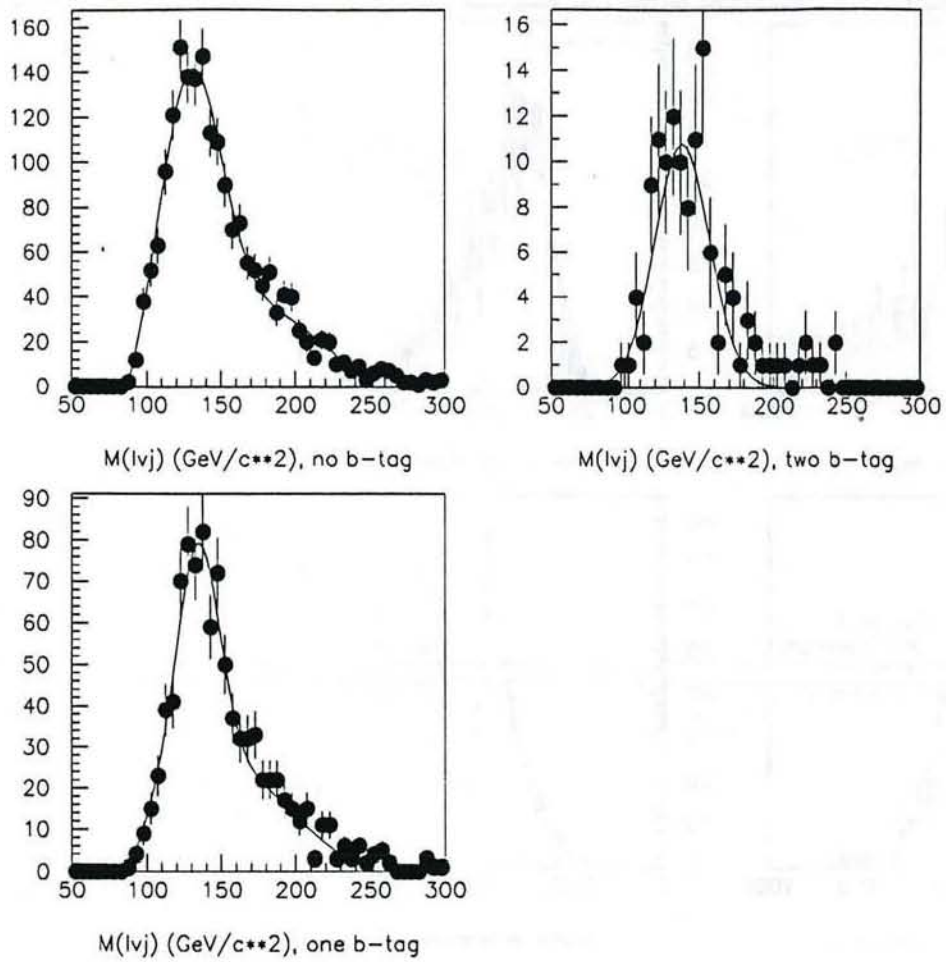

Figure 20: Reconstructed invariant top mass from the lepton side of the event for SVX II (G3) in three cases: Where the SVX II b tag is not used, where one of the jets has a b tag, and where two jets have a b tag.

The greatest improvement would be for the W' search. Without an SVX the current tracking on a high p_T muon is rather poor, making it not useful for the W' search. Figure 21 shows the transverse mass distributions from a 500 GeV/c^2 W' in the muon channel for different tracking resolutions. The first plot (upper left) is for CTC tracking only: $\sigma_p/p^2 = 0.002(\mathrm{GeV/c})^{-1}$. The upper right plot is for CTC plus a beam constraint: $\sigma_p/p^2 = 0.0011(\mathrm{GeV/c})^{-1}$. The lower 2 plots show what could be achieved with factors of 2 and 5 in the latter number. A factor of two is the least that can be expected from the SVX II. This might be the difference between a limit and a discovery.

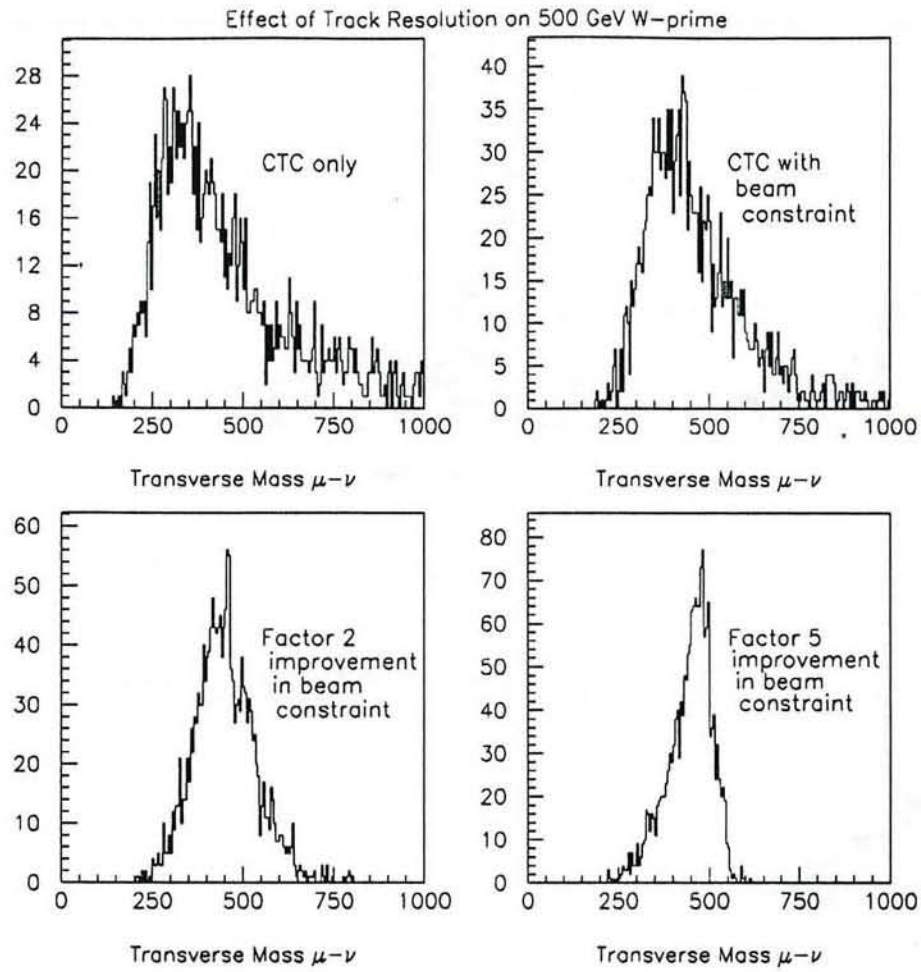

Figure 21: Transverse mass distributions from a 500 GeV/c^2 W' in the muon channel for different tracking resolutions.

5.5 B Decays

Studies were made to determine the mass and vertex reconstruction resolution and acceptance for representative B decay channels. These results are intended to indicate the acceptance and precision obtained with the geometries under consideration in a format as free as possible from constraints due to particular choices in the analysis technique.

Inclusive B Decays

In order to determine the improvement in geometrical acceptance for charged tracks from inclusive B decays for the SVX II detector, we have generated two samples of ISAJET inclusive $b\bar{b}$ production with $p_T(b) > 3$ GeV/c and $p_T(b) > 10$ GeV/c. The average B decay charged track multiplicity, including charged daughters from cascade charm decays, for these

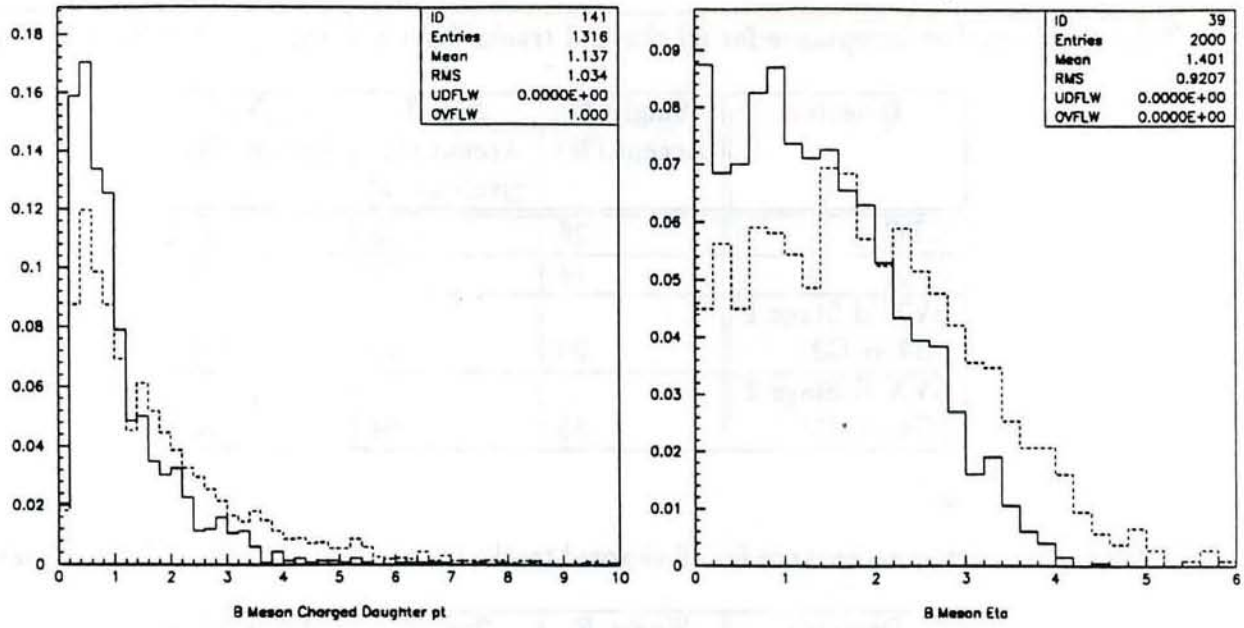

Figure 22: Shown are the B meson charged daughter p_T distributions (in GeV/c) and the B meson pseudorapidity distributions for the $p_T(b) > 3$ GeV/c (solid line) and $p_T(b) > 10$ GeV/c (dashed line) inclusive $b\bar{b}$ samples.

two samples was 4.6 tracks. The first sample gives the flatter pseudorapidity distribution and softer B meson track p_T that would be obtained for a non-triggered B while the latter is more suggestive for a triggered B meson. Figure 22 shows the B meson p_T and η distributions for the two samples. It is seen that the higher b quark p_T sample contains noticeably more centrally-produced and higher transverse momentum B mesons, as expected.

The geometrical acceptance for observing all charged tracks from a B meson was determined for the CTC, the SVX, and the SVX II Stage 1 and 2 detectors. For the CTC acceptance, the track was required to pass through the first two superlayers. For the SVX and SVX II Stage 1 detectors, the track must have been in the CTC acceptance and had at least 3 out of 4 hits in the silicon barrel. For the SVX Stage 2 detector, a disk tracking system with the inner three disks at $z = 55.0$, 62.5, and 70.0 cm and an outer radius of 27.0 cm was added to the Stage 1 double length barrel. For the case of a track missing the CTC or having less than 3 hits in the Stage 1 detector, it was checked if the track hit the first two layers of the barrel and fell within the acceptance of the inner three disks. If it did, the track was included in the Stage 2 detector acceptance. This combination of barrel and disk hits would allow the track to have useful vertexing information as well as a momentum or charge-sign determination.

Tables 9 and 10 show the geometrical acceptance for containing all charged daughters from B meson decay for the different detector elements. The first column describes the single B meson acceptance which is given as the fraction of B mesons which have all charged tracks in the detector acceptance. The second column gives the acceptance for all charged tracks

Table 9: Geometric acceptance for all charged tracks from a B meson for $p_T(b) > 3$ GeV/c.

Detector	Single B Accept.(%)	2nd B Accept.(%) given 1st B	Both B Accept.(%)
CTC	36	39	14
SVX	16	33	5.3
SVX II Stage 1 (G2 or G3)	28	34	9.5
SVX II Stage 2 (G4 or G5)	55	64	35

Table 10: Geometric acceptance for all charged tracks from a B meson for $p_T(b) > 10$ GeV/c.

Detector	Single B Accept.(%)	2nd B Accept.(%) given 1st B	Both B Accept.(%)
CTC	52	59	31
SVX	23	43	10
SVX II Stage 1	42	51	21
SVX II Stage 2	64	70	45

from the second B given that the first B was in the acceptance. The last column is just the product of the first two and gives the fraction of events which have all charged tracks from both B's contained.

Several conclusions can be drawn from the numbers in Tables 9 and 10:

1. A large increase in acceptance is seen for the double length barrel of the SVX II Stage 1 detector versus the present CDF SVX. The increase is $\approx 80\%$ for the single B acceptance and nearly 100% for both B's.

2. The double length barrel appears reasonably well-matched to the two superlayer acceptance of the CTC used here.

3. For $p_T(b) > 3$ GeV/c, the 9.5% two-B acceptance of the SVX II Stage 1 detector increases to 35% when the disk system is included. The disk system modeled here has not been optimized but this result indicates that a large increase in B acceptance can be obtained by improving the tracking capabilities in the forward rapidity region.

A second study of inclusive B acceptance was performed which required both B's to decay semileptonically with $p_T(l) > 2.5$ GeV/c. This was done for a $p_T(b) > 10$ GeV/c sample.

Table 11: Geometric acceptance for all charged tracks from a B meson for different pseudorapidity intervals of the dileptons for $p_T(l) > 2.5$ GeV/c and $p_T(b) > 10$ GeV/c.

Detector	$\|\eta(ll)\| < 1$, 21% of evts			$\|\eta(ll)\| < 2$, 61% of evts			$\|\eta(ll)\| < 3$, 92% of evts		
	1st$B$ (%)	2nd$B$ (%)	Both$B$ (%)	1st$B$ (%)	2nd$B$ (%)	Both$B$ (%)	1st$B$ (%)	2nd$B$ (%)	Both$B$ (%)
CTC	88	88	77	77	78	60	63	65	41
SVX	42	74	31	40	63	25	32	51	16
SVX II Stage 1	74	78	58	66	70	46	55	58	32
SVX II Stage 2	78	84	66	81	86	70	76	82	62

Table 12: Inclusive both B acceptance for different pseudorapidity intervals of the dileptons.

Detector	$\|\eta(ll)\| < 1$	$\|\eta(ll)\| < 2$	$\|\eta(ll)\| < 3$
	Both B (%)	Both B (%)	Both B (%)
CTC	16	37	38
SVX	6.5	15	15
SVX II Stage 1	12	28	29
SVX II Stage 2	14	43	57

The idea here was to look at the B meson acceptance as a function of the pseudorapidity of the two leptons which could have caused the event trigger. If daughter tracks from the B mesons were required in the event trigger, then it is more likely that the B meson and its other daughters were within the detector acceptance. Table 11 shows the same acceptance quantities as in Tables 9 and 10 above for different pseudorapidity ranges of the dileptons from the $B\bar{B}$ decay. The values given in this table have to be multiplied by the fraction of $B\bar{B}$ events generating dileptons in each of the three pseudorapidity ranges in order to obtain the inclusive B acceptance. This was done for the value for accepting both B's and the results are shown in Table 12. These acceptance values are significantly higher than in the study presented in Tables 9 and 10. For the dilepton $|\eta| < 2$ case, the two B acceptance for the SVX II Stage 1 detector increased from 21% for the fully inclusive sample to 28% for the dilepton sample. The SVX II Stage 2 detector both B acceptance also increased to 57% ($|\eta(ll)| < 3$) from 45% in the earlier study.

Finally, the inclusive B meson acceptance was studied for the case of only one of the B's decaying semileptonically with $p_T(l) > 2.5$ GeV/c and $p_T(b) > 10$ GeV/c. It is planned that a low p_T single lepton trigger will be used in conjunction with a secondary vertex trigger. For this reason, the average fraction of charged tracks from a B meson contained within each

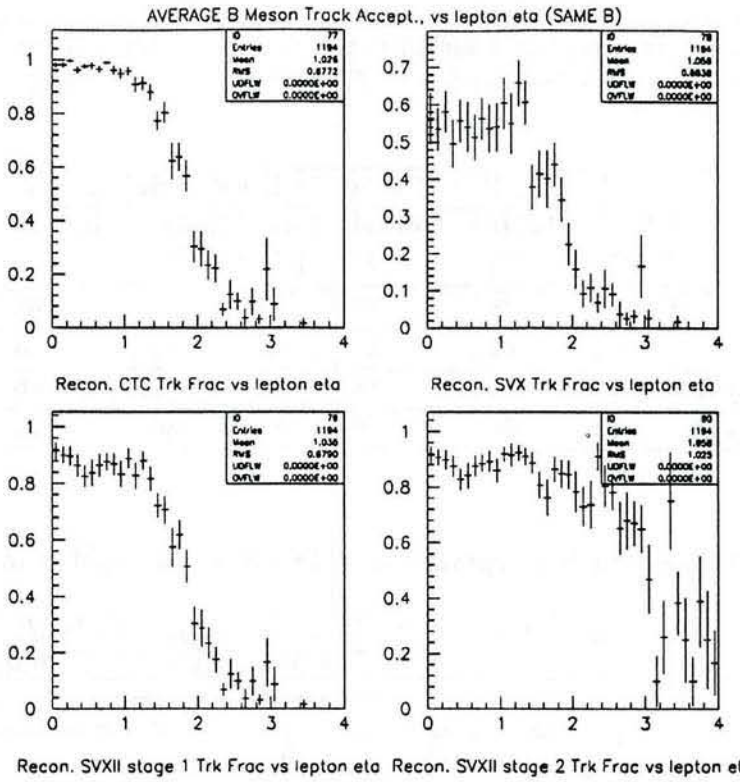

Figure 23: Average B meson charge track fraction for each detector as a function of the lepton (produced by that B) pseudorapidity.

detector acceptance was studied as a function on lepton pseudorapidity. This was done both for the B producing the lepton and also for the other B. Given a B meson average charged track multiplicity of 4.6, the mean number of tracks available to secondary vertex trigger could be estimated for the different detector acceptance and lepton η values. Figs. 23 and 24 show the average B meson charged track fraction contained in each of the detectors as a function of lepton η for the two cases of the lepton decaying from the same B and from the other B. We see that for the first case, the addition of the tracking coverage modeled by the disk system in the SVX II Stage 2 detector greatly increases the reconstructed charged track fraction in the lepton η range between 1.6 - 3.0. The fraction is greater than 75% out to $|\eta(l)| = 2$ and is still above 50% at a lepton η of 3. The reconstructed charged track fraction versus the lepton η from the other B is found to be relatively flat. This is expected from the uncorrelated nature of $B\bar{B}$ pair production.

It is seen from these studies that large increases in inclusive B acceptance can be obtained by doubling the length of the present SVX detector (SVX II Stage 1) and by the addition of tracking system (presented here as a disk system) to cover the rapidity region between $1.6 < |\eta| < 3.0$ (SVX II Stage 2). The addition of a suitable trigger, either a dilepton or single lepton + secondary vertex trigger, can also improve the acceptance and total yield of reconstructed and/or tagged $B\bar{B}$ events.

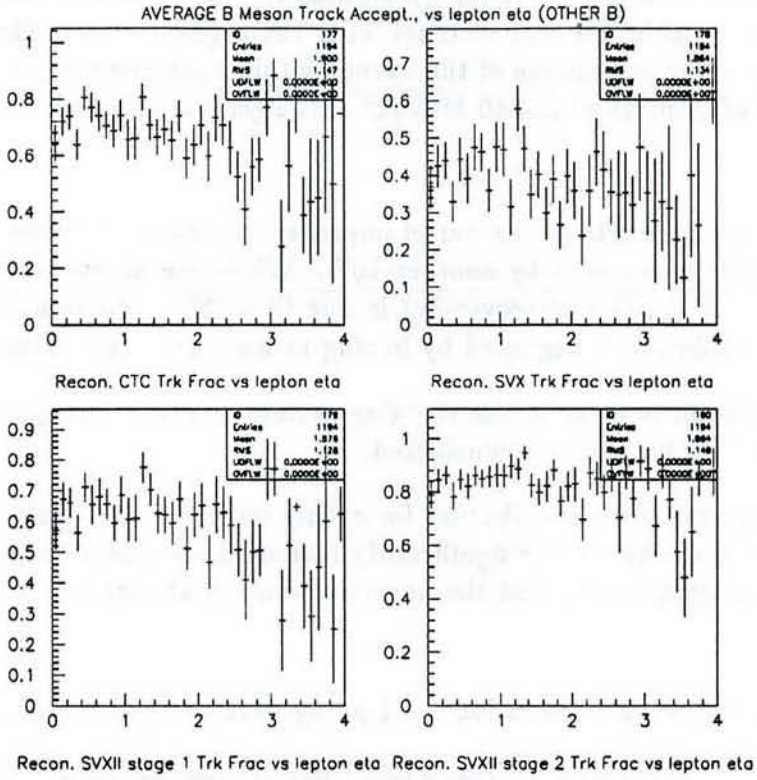

Figure 24: Average B meson charge track fraction for each detector as a function of the lepton (produced by the other B) pseudorapidity.

Exclusive B Decays

Invariant mass resolution was studied with a Monte Carlo data set of 450 $B\overline{B}$ events in which both B's decay to ψK_s^0. In this sample lifetimes of the long-lived particles were set to zero so that all decays occurred at the origin. Generated information was used to select the daughters of the ψ and K_s^0, and no requirements were placed on track p_T. To show the contribution of SVX II to the tracking system as a whole, the complete tracking system was used in the mass reconstruction. Consequently, tracks that were fit in the outer tracking system but which missed the SVX II were included. Fig. 25 shows the result; plotted is the reconstructed B invariant mass for geometries G1, G2, G3, and G5. Table 13 summarizes the obtainable widths for this channel with these geometries. The righthand column of Table 13 shows the percentage of the events within each geometry's acceptance which have a reconstructed B mass within 40 MeV/c^2 of the generated mass. The following features are evident:

1. Doubling the length of the barrel improves the mass resolution by 20%; adding barrel z readout improves it by another 10%. While the acceptance here is defined by the outer tracking, this improvement is due to a 38% reduction in the number of events whose resolution is degraded by having at least one track miss the silicon detector.

2. The addition of disks to the tracking system increases the geometric acceptance from 42% to 76% for the case considered.

3. Although the mass distribution for events reconstructed with G4 and G5 has evident tails, they are due to the significantly increased acceptance which the disks provide for low-p_T, high-η tracks, and the poorer resolution at high η.

Table 13: B mass resolution for 4-prong decay at the origin, for 5 geometries.

Model	σ_m (MeV/c^2)	Percentage of events with $\lvert m_B^{\rm recon} - m_B^{\rm gen}\rvert \leq 40$ MeV/c^2
G1	21 ± 1	31
G2	17 ± 1	35
G3	15 ± 1	36
G4	18 ± 1	53
G5	18 ± 1	53

The obtainable resolution is highly correlated with the $|\eta|$ of the track having maximum $|\eta|$. This can be seen in Fig. 26, a plot of the error on the reconstructed mass as a function of the maximum daughter $|\eta|$. In the range $0.0 < |\eta| < 2.0$, the mean error on the B mass increases from 5 to 40 MeV/c^2.

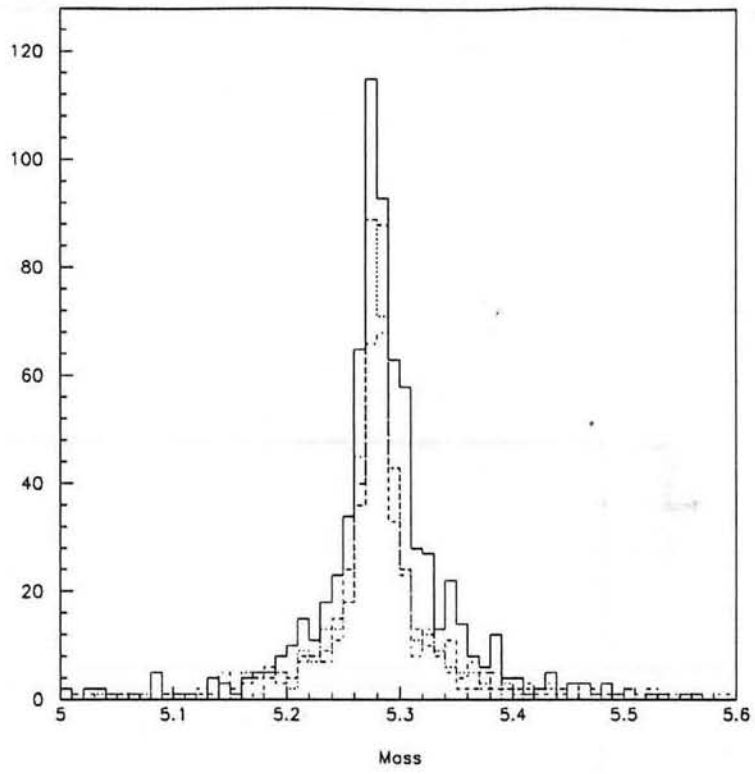

Figure 25: Reconstructed B^0 invariant mass for geometries G1(dot-dash), G2(dot), G3(dash), and G5(solid). Geometry G4 produces results which are statistically equivalent to those of G5, so it has been omitted in order to improve the figure's readability.

The decay mode $B_s \rightarrow D_s\pi\pi\pi$ with track $p_T > 350$ MeV/c is used to study the mass and vertex resolution for decays involving charm. The invariant mass distribution without vertex constraint is shown in Fig. 27 for geometry G2 and has a width of 18 MeV/c^2. The addition of a vertex constraint reduces the width by $\approx 30\%$ to 13 MeV/c^2. For geometry G3, the width is reduced to 10 MeV/c^2 for both the constrained and unconstrained vertex fits.

The study of vertex resolution includes modes with different multiplicity for both B decay through charm and direct B decay. The decay mode $B_s \rightarrow \psi\phi$ ($p_T(b) > 10$ GeV/c) with its single 4-prong vertex is an example of a direct B decay mode with possibly the best vertex resolution. Figure 28 shows a resolution of 53 microns for the tranverse decay length using geometry G1. Figure 29 shows the reconstructed transverse decay length divided by its error, i.e., the significance of the vertex separation. Figure 30 is an integral of this distribution, showing that a 5σ cut on the vertex separation is 65% efficient for this sample. Such a cut will reduce the background due to tracks from the primary vertex and retain a clean signal with good statistics.

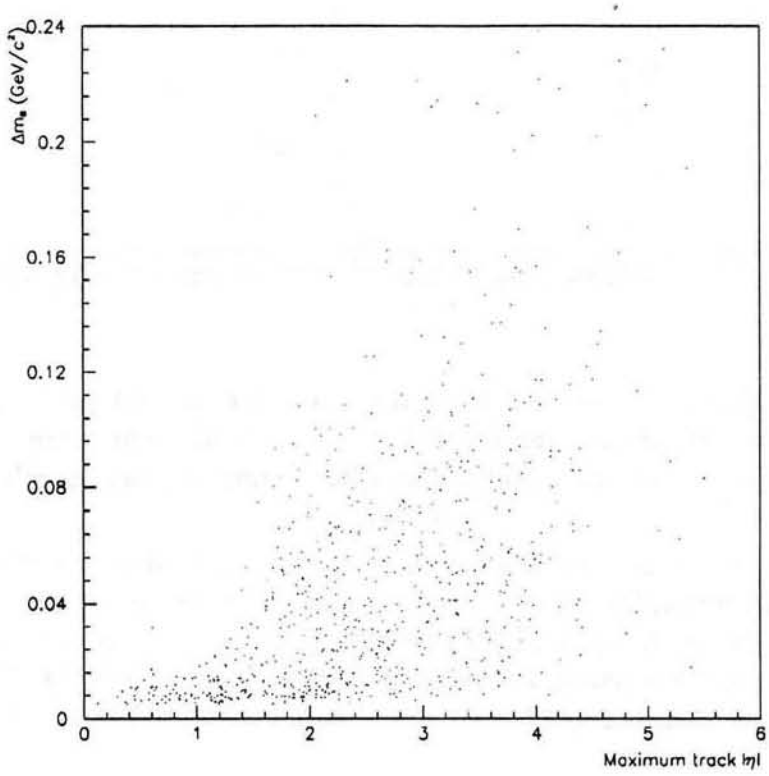

Figure 26: Error on the reconstructed mass as a function of the maximum daughter $|\eta|$.

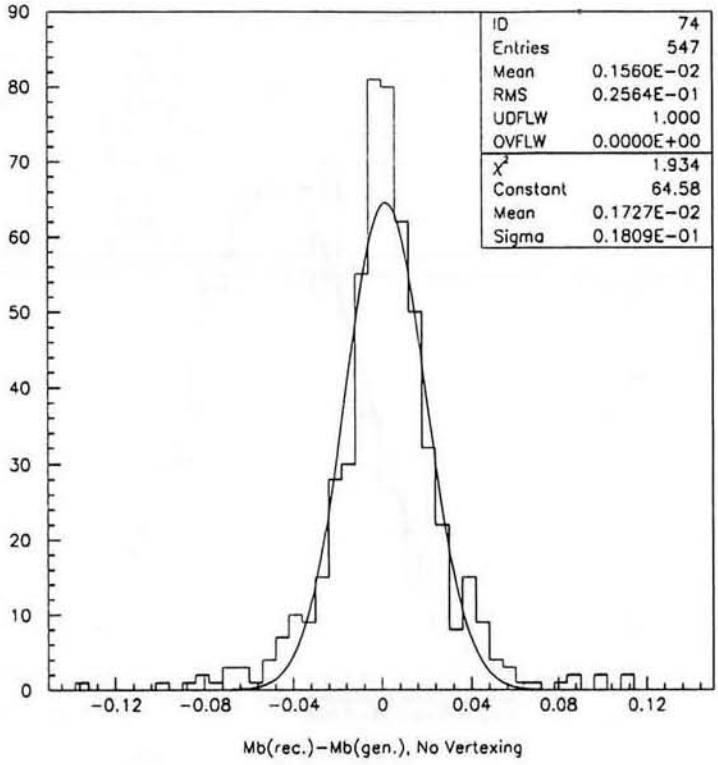

Figure 27: Mass distribution without vertex constraint for the decay mode $B_s \rightarrow D_s\pi\pi\pi$. Units are GeV/$c^2$.

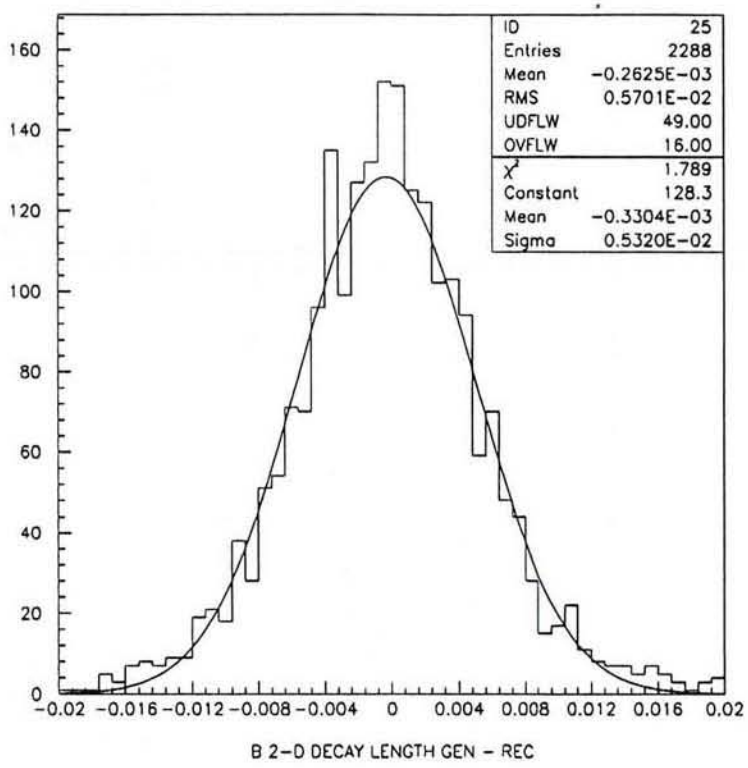

Figure 28: Transverse decay length resolution for the decay mode $B_s \to \psi\phi$ using geometry G1. The units are cm.

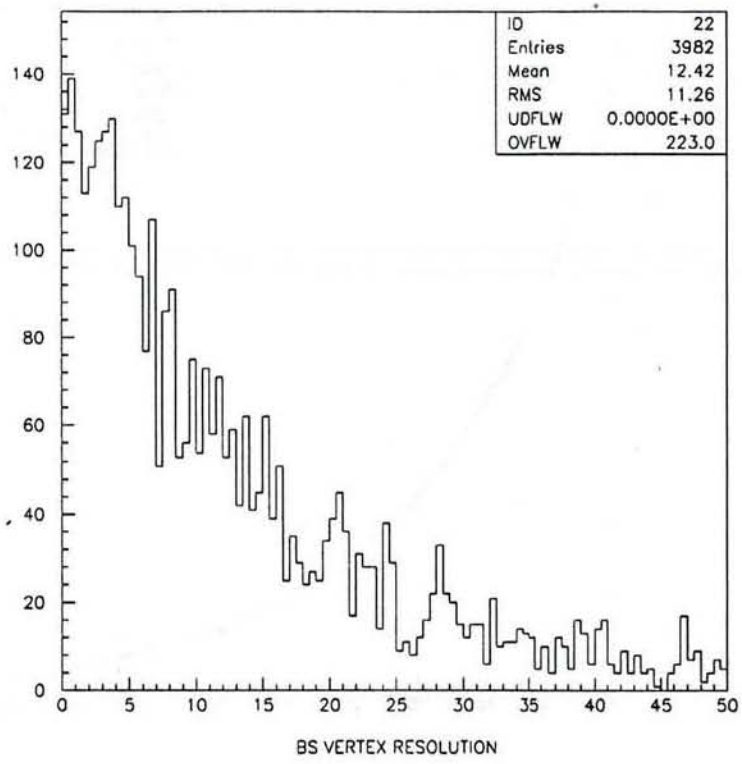

Figure 29: Transverse decay length significance for the decay mode $B_s \to \psi\phi$ using geometry G1.

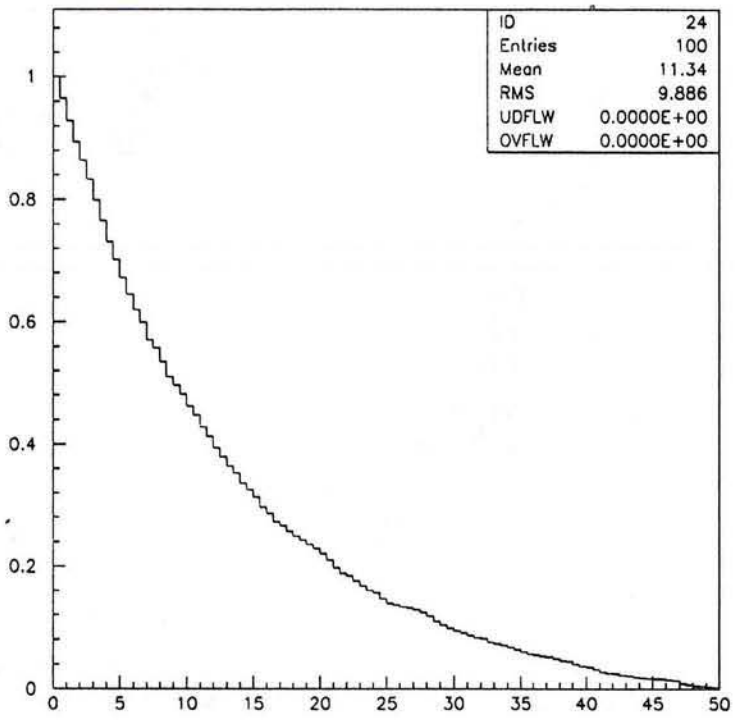

Figure 30: Integral transverse decay length significance (normalized) for the decay mode $B_s \to \psi\phi$ using geometry G1.

5.6 B_s Mixing

Introduction

The primary interest for measuring X_s is to determine the CKM matrix element $|V_{td}|$ through the relationship:

$$\frac{X_s}{X_d} = \frac{f_{B_s}^2 B_{B_s} \tau_{B_s}}{f_{B_d}^2 B_{B_d} \tau_{B_d}} \frac{|V_{ts}|^2}{|V_{td}|^2}, \quad (1)$$

where $f_{B_{s,d}}^2$, $B_{B_{s,d}}$, and $\tau_{B_{s,d}}$ are the decay constant, bag parameter, and lifetime of the B_s and B_d mesons respectively. Several common factors, including the dependence on the top quark mass, cancel in the ratio of X_s/X_d where we need only to know the quantity $f_{B_s}^2/f_{B_d}^2$ rather than $f_{B_s}^2$ and $f_{B_d}^2$ individually, for which there is much greater uncertainty [13]. Present estimates are that $f_{B_s}^2 = (1.6 \pm 0.4) f_{B_d}^2$ [14], $B_{B_s} \approx B_{B_d}$ [15], and $\tau_{B_s}/\tau_{B_d} \approx 1$ [16]. Thus, we can determine $|V_{td}|$ by measuring X_s and using the value of X_d from ARGUS [17] and CLEO [18] since $|V_{ts}|$ is constrained by unitarity to be approximately $|V_{cb}|$. $|V_{td}|$ is of course related to the CP violating phase in the CKM matrix, for which there is a great deal of interest. The unitary constraint of the CKM matrix provides only limited knowledge of $|V_{td}|$ and further improvement for a direct determination of $|V_{td}|$ requires the measurement of the top quark mass and knowledge of f_{B_d}.

The current estimate for the value of X_s has a broad range and is separated into two regions depending on the value of f_{B_d}. A value of f_{B_d} near 131 MeV is favored by many potential-model and QCD sum rule estimates while $f_{B_d} \approx 225$ MeV is suggested from lattice QCD calculations. Potential models give $f_{B_s}^2 \approx 1.6 f_{B_d}^2$ while the overall range for this quantity in various models appears to be between 1.2 to 2. The prediction for B_s mixing is:

$$X_s = (14 \pm 6)(f_{B_s}/200\text{MeV})^2. \quad (2)$$

if we assume $m_t = 140 \pm 40$ GeV/c^2 and $f_{B_s}^2 = (1.6 \pm 0.4) f_{B_d}^2$[19] where the error is dominated by the uncertainty on the mass of the top. This formula yields $X_s = 28 \pm 12$ and $X_s = 10 \pm 4$ for $f_{B_d} = 131$ MeV and $f_{B_d} = 225$ MeV respectively. In both cases X_s is large and a time integrated measurement of mixing will be saturated. Therefore, a measurement of the time evolution of the mixing oscillations is necessary.

Simulation Studies

To determine the B_s mixing parameter X_s, the decay length and momentum must be measured for a sample of flavor-tagged B_s mesons. These B_s mesons must be flavor-tagged at both production and decay in order to determine if they oscillated or not. Typically, the flavor of the B_s meson at production is tagged by the flavor of the other B meson at decay. The ability to tag the B_s at production requires good acceptance for the other B. This can lead to a mistagging dilution of the B_s sample if the other B is a B_d or B_s meson which oscillated. The B_s flavor at decay is obtained from its decay products. However, certain decay modes of the B_s are un-taggable, such as $B_s \to \psi\phi$, because the particle-antiparticle nature of the B_s cannot be determined from its daughter particles. We attempt here both

to simulate the performance of the SVX II upgrade and to identify the best way to perform the X_s measurement.

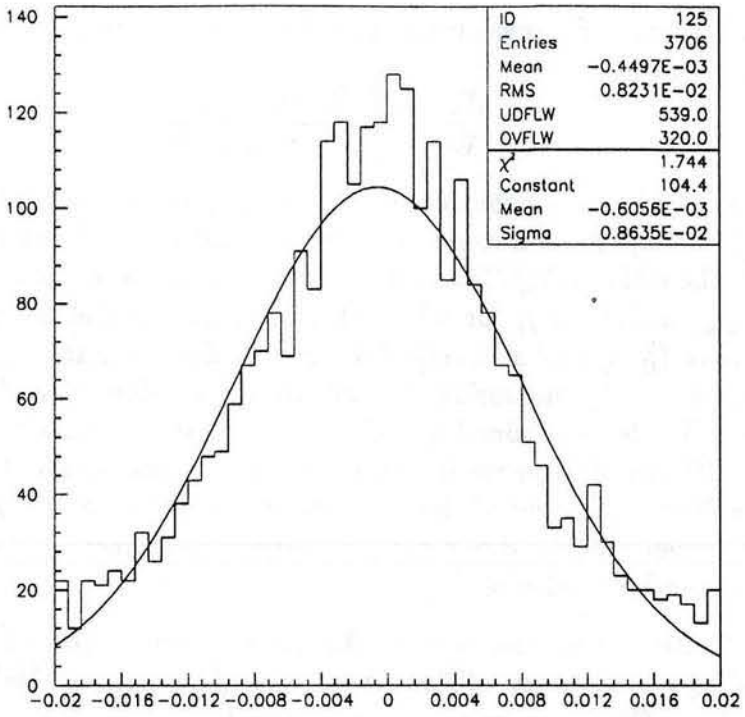

Figure 31: B_s transverse decay length error obtained by combining the ϕ and lepton in semileptonic B_s decay. The units are cm.

Two approaches are considered in determining the optimal decay mode of the B_s for this measurement. The most promising for lower luminosity is requiring the semileptonic decay of both the B_s and the other B:

$$B_s \to l\nu D_s, D_s \to \phi + X; B \to l\nu + X. \tag{3}$$

This has the advantage of being able to trigger on the two leptons at low p_T and thus forces the other B to be within the detector acceptance. For this high-rate decay mode, we initially search for the ϕ near the lepton and use it to tag the likely presence of a B_s. Depending on the p_T and multiplicity of the D_s decay, the ϕ direction could be combined with the lepton direction to yield a good measure of B_s transverse decay length. A sample of ISAJET events containing oscillating B_s mesons with $p_T(b) > 10$ GeV/c and $p_T(l) > 2.5$ GeV/c was used. Figure 31 shows that for this sample the resolution on the $\phi - l$ transverse decay length is 86 microns in geometry G1, which is almost identical to the result obtained if the D_s is fully reconstructed in the decay $D_s \to \phi\pi$. Any additional pions from the D_s decay that are associated with the ϕ vertex would also be included in order to fully or more completely reconstruct the D_s. The limiting factor for finding the proper time of the decay in a semileptonic B_s mode is the uncertainty in the B_s momentum since the B_s is only partially

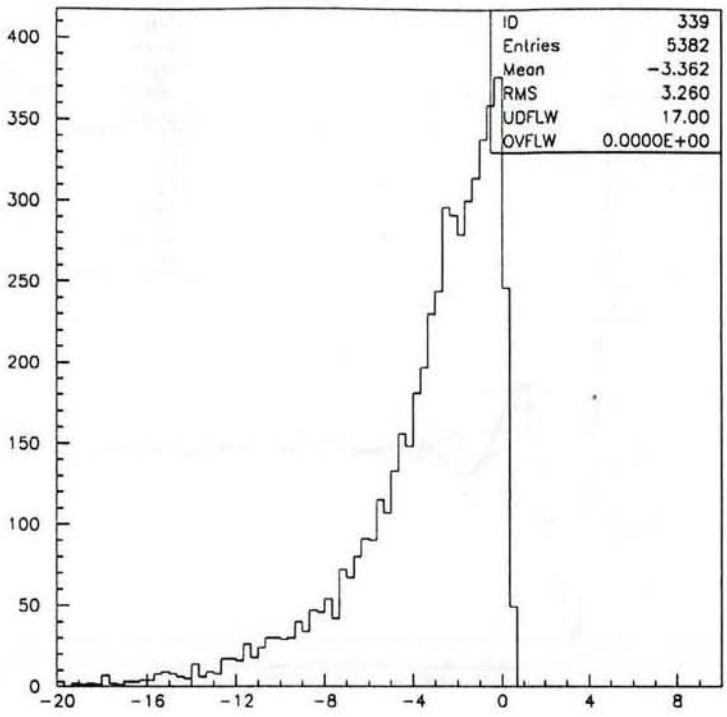

Figure 32: The difference in GeV/c between the B_s transverse momentum and the transverse momentum obtained by combining the D_s and lepton in semileptonic B_s decay.

reconstructed due to the missing neutrino or the lack of a fully reconstructed D_s. Figure 32 shows that on average the neutrino takes 3.4 GeV/c p_T in a semileptonic B_s decay. The missing p_T can be corrected using Monte Carlo simulation. Figure 33 shows the oscillation frequency plot for $X_s = 5.0$ with a perfect B_s tag and no cut on vertex separation. A clean oscillation structure is seen with $\approx$ 4000 events. A vertex cut will reduce the statistics at short lifetimes.

Using a calculation similar to that derived in Reference [20], we obtain the following estimate for the number of events, N, needed to observe a B_s oscillation signal at five standard deviation significance for a given value of X_s and proper time resolution σ_t:

$$N \simeq \frac{125}{6} X_s e^{\frac{4\pi}{X_s}} e^{\frac{(X_s^2-1)\sigma_t^2}{2}}, \tag{4}$$

where σ_t is in units of proper time. This expression includes the effect of signal dilution from mistagging due to B_d meson oscillation. From Monte Carlo studies, the proper time resolution for the semileptonic B_s decay mode is estimated to be in the range of 0.20 - 0.30 proper times. This is due to the relatively poor momentum resolution of the partially reconstructed B_s decay. Applying various kinematic cuts and using improved momentum estimators can reduce the uncertainty on the B_s momentum at some cost in reconstruction efficiency. The number of tagged and reconstructed events required is between 2000 and

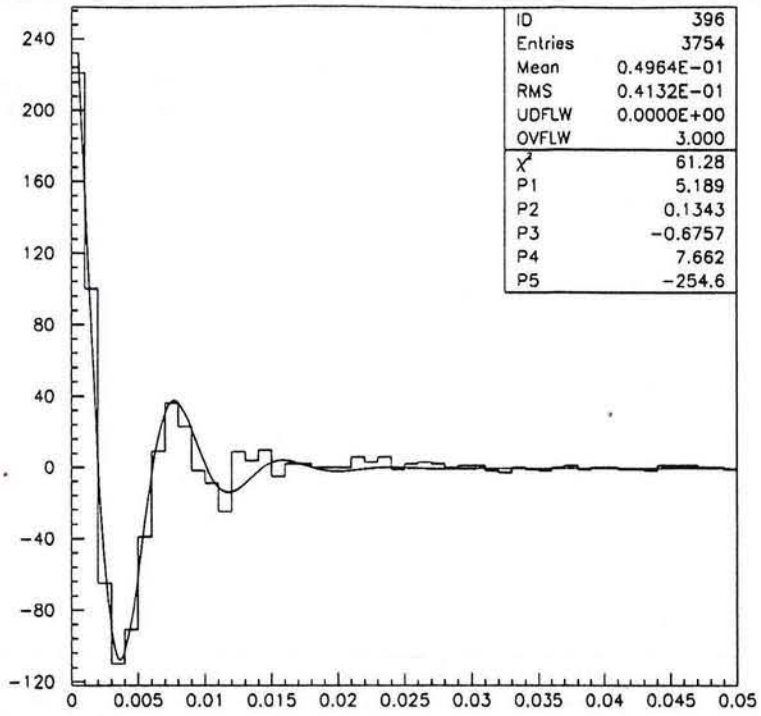

Figure 33: Oscillation plot for semileptonic B_s decay with $X_s = 5.0$. The units on the abscissa are cm/GeV/c.

5000 over the range of $4 < X_s < 7$ for the semileptonic B_s decay mode ($0.20 < \sigma_t < 0.30$).

The luminosity necessary to reach a given X_s value can be obtained by estimating the cross section for tagging and reconstructing a semileptonic B_s decay and using the above number of events necessary for a clear signal. This was done assuming a dimuon trigger with $p_T(\mu) > 2.5$ GeV/c and muon and charged particle coverage for $| \eta | < 2.0$. For the decay chain in Equation 3, we use $\mathrm{BR}(D_s \rightarrow \phi + X) = 0.10$ and assume a 15% B_s meson content of all B hadrons. Including a cut of 5σ on the significance of the $\phi - \mu$ vertex and allowing a 30% background rate for ϕ production from $B^{\pm}$ and B° decay, we obtain a cross section of 8.0 ± 4.0 pb for reconstructing and tagging a semileptonic B_s decay. Figure 34 shows the integrated luminosity necessary for measuring X_s between 4 and 7 for $0.20 < \sigma_t < 0.30$. The shape of the curves show that for small X_s values, the B_s decays before it oscillates so that more data is needed to make a measurement than for slightly larger X_s values. It is also seen that the amount of data needed is very dependent on the proper time resolution σ_t and that for $\sigma_t \geq 0.30$, the measurement becomes very difficult. The minimum luminosity required to establish X_s as different from zero by five standard deviations occurs at $X_s \approx 5$. For $\sigma_t = 0.25$ this corresponds to a luminosity 200-400 pb^{-1}.

Since it is anticipated that the semileptonic mode will have a limited X_s reach due to the momentum uncertainty in the partial reconstruction of the B_s decay, a simulation of a

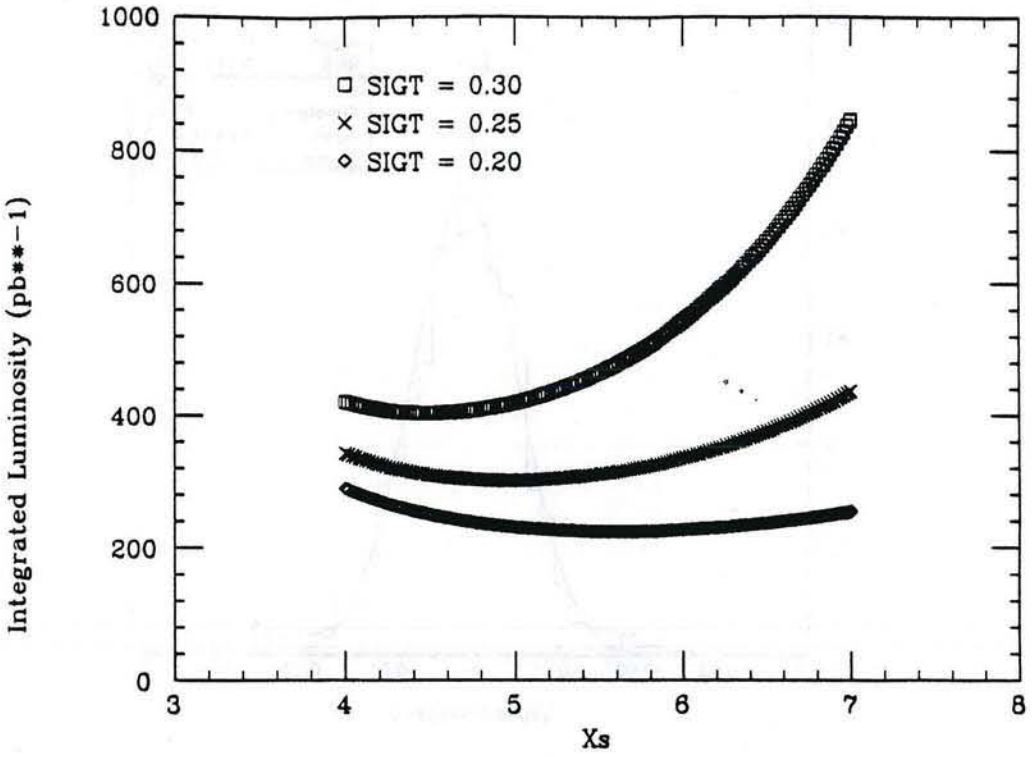

Figure 34: Estimated integrated luminosity necessary to measure X_s over the range $3 < X_s < 7$ for semileptonic B_s decay with $0.20 < \sigma_t < 0.30$.

fully reconstructable B_s decay was also studied. The disadvantages of this decay mode are that the event rate will be very small because all exclusive B_s decay modes have very small branching fractions and the reconstruction efficiency will also be lower.

As an example of an exclusive B_s decay mode, we studied $B_s \rightarrow D_s\pi\pi\pi$. The branching fraction of this mode is estimated to be 1.1%. The D_s has a 2.8% branching ratio decaying to $\phi\pi$, and half of the ϕ's will decay to K^+K^-. This kind of event will have three tracks from the B_s vertex and three tracks from D_s vertex. Since CDF does not have a secondary vertex trigger for this decay mode at this time, we have assumed that these events come from the inclusive lepton trigger, in which the lepton comes from the other B and also provides the flavor tagging.

We generated $b\bar{b}$ events from ISAJET, and selected those events with trigger B lepton $p_T > 5$ GeV/c and a B_s with the above decay mode. In order to be able to reconstruct the events, we also required all π's and K's to have $p_T > 0.35$ GeV, This decay can be reconstructed by looking for ϕ's with displaced vertices in the event, then reconstructing D_s with the tracks coming from the ϕ vertex, and finally reconstructing the B_s with tracks from the other 3-prong vertex.

Our current study was to find out what X_s range we can explore. The key in any X_s analysis is the resolution of the measured B decay time, which in turn is determined by

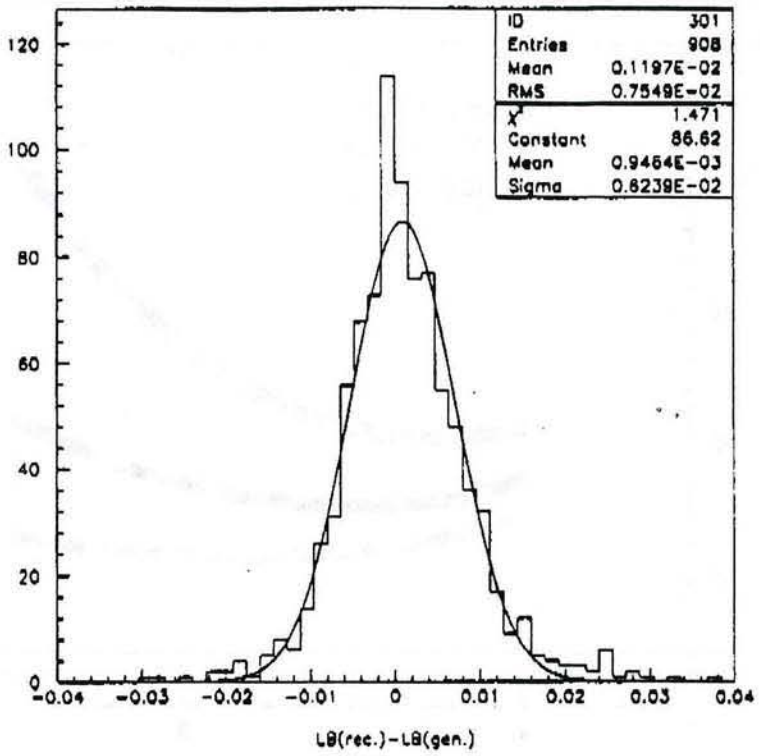

Figure 35: Resolution of the 3D B_s decay length for model G3 in cm.

the B vertex and B momentum resolution. The resolution of the decay length is shown in Fig. 35. For model G2, the momentum resolution is the same as for G3, but the 3D vertex resolution is of course much worse. However, if we project into the $r - \phi$ plane, the 2D vertex resolution shown in Fig. 36 is comparable as expected. The 2D and 3D resolutions in the proper time distribution are shown in Fig. 37. The 3D proper time resolution is about 20% better than the 2D resolution. To illustrate that the vertex resolution is adequate for measuring large X_s values, the reconstructed time-dependent oscillation plot with $X_s = 20$ for 2845 reconstructed and tagged B_s decays is shown in Fig. 38. No vertex separation cut is applied to this plot, but it shows that the vertex detector can resolve this frequency of oscillations.

To estimate the luminosity necessary to obtain such a sample of exclusive B_s meson decays, we assumed a single lepton trigger for both electrons and muons with $p_T > 4$ GeV/c. This lepton would be from the other B and its charge sign would tag the flavor of the B_s at production. Charged particle tracking and lepton triggering out to $|\eta| < 2.0$ was also required. The product branching ratio for $B_s \rightarrow D_s\pi\pi\pi, D_s \rightarrow \phi\pi, \phi \rightarrow KK$ was taken to be 2 x 10^{-4} and a proper time resolution of $\sigma_t = 0.10$ for this fully reconstructed B_s decay mode was determined from the simulation. Including the efficiency for reconstruction of the B_s and mistagging from B_d oscillations, it is estimated that at least 1 fb^{-1} of data would be needed to measure $X_s = 20$ with the SVX II detector.

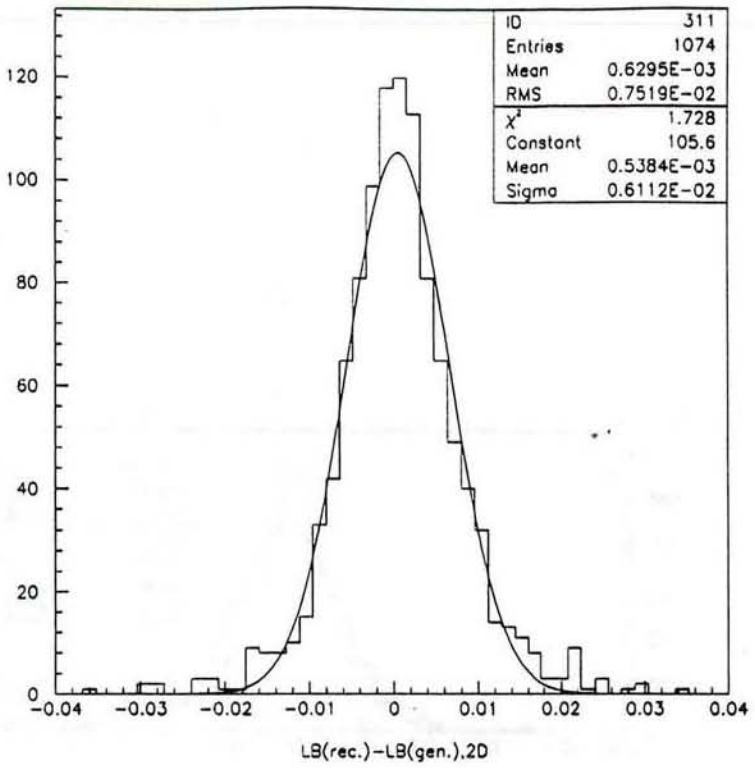

Figure 36: Resolution of the 2D B_s decay length for model G2 in cm.

These analyses do not include sources of mistagging semileptonic charm decay which will reduce the amplitude of the observed oscillations. For the fully reconstructed exclusive mode, background sources are expected to be very small. For the inclusive mode, the background (for example from the semileptonic B decays other than B_s into modes containing ϕ) could shift or skew the distribution in Fig. 38, but will not affect the frequency or the amplitude of the oscillations.

These studies are on-going and much use will be made of the present SVX data to determine better the reconstruction and tag efficiencies in the actual colliding beam environment. Improvements with the extended rapidity coverage of the disk system are also under investigation. Since this analysis requires tagging from the other B, we expect a significant improvement in acceptance when the disk system is added.

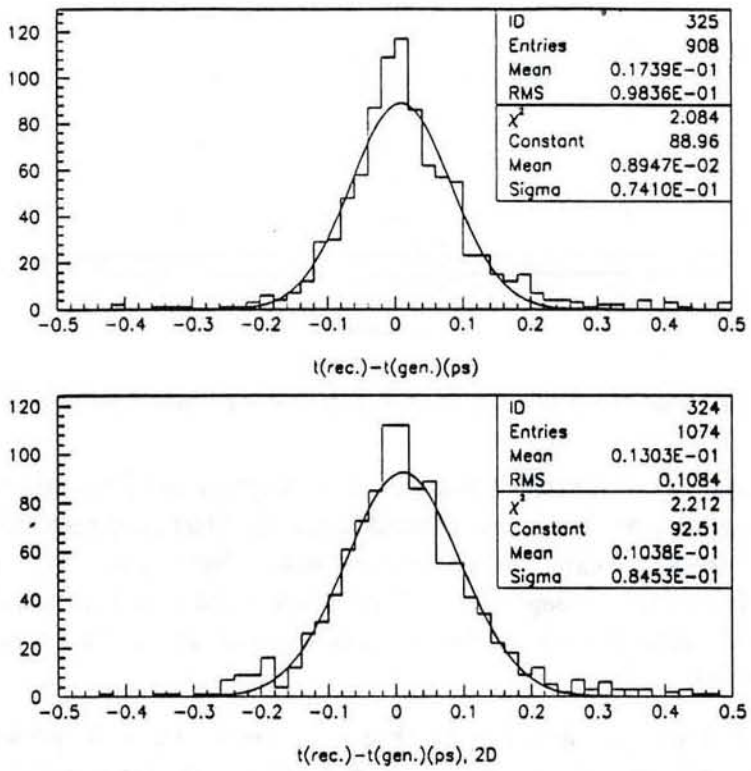

Figure 37: Reconstructed minus generated B_s decay time in picoseconds in 3D and 2D.

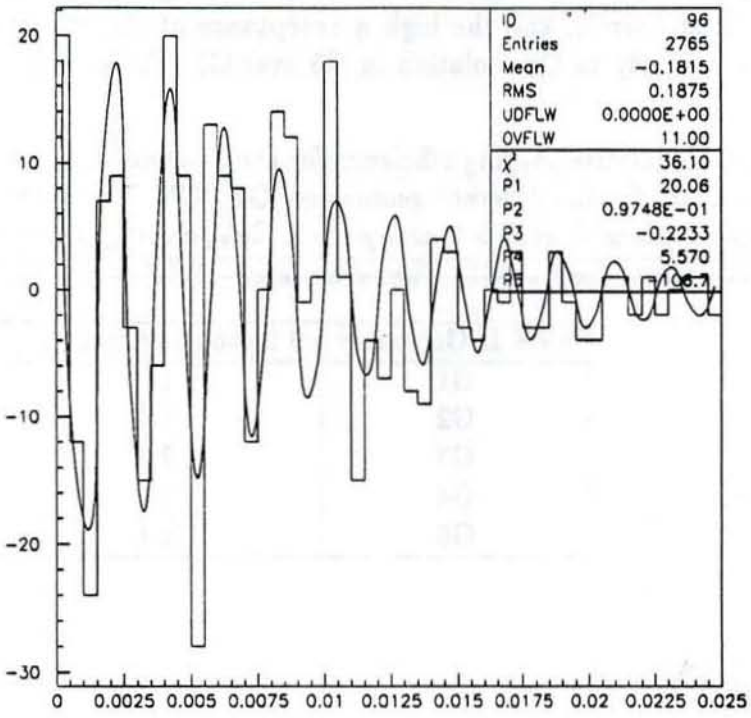

Figure 38: Oscillation plot for $B_s \to \pi\pi\pi D_s, D_s \to \phi\pi$ decay with $X_s = 20.0$. The units on the abscissa are cm/GeV/c.

5.7 CP Violation Studies

The measurement of CP violation in the B system would be a strong test of the standard model. At the Tevatron, CP violation in neutral B decays results in a net, time integrated asymmetry in the rate for $B(\bar{B})$ decays to CP eigenstates. Consequently, the measurement requires only the counting of the rates for B vs $\bar{B}$ decays. Even so, the measurement of such asymmetries presents an enormous experimental challenge. This is due to the statistics required, the small branching ratios involved, and the low p_T of the events. A key aspect of this challenge is the performance of the tracking detector, so it is important to examine the implications of our vertex detector design in this context. Our initial studies for the lepton tagged ψK_s mode indicate that there are substantial gains from both the z resolution with the double-sided barrels, and the high η acceptance of the disks, giving a factor of of four increase in sensitivity to CP violation in G5 over G1 (Table 14).

Table 14: SVX II relative tagging efficiency for the *b tag* example: $B \to e/\mu\,\nu X$, $B \to J/\psi K_s$ with $J/\psi \to \mu^+\mu^-$ for the different geometries G1 - G5. The SVX II tag requires an impact parameter significance $\delta/\sigma(\delta) > 3$ and $p_T > 2$ GeV/c for ≥ 3 leptons in the event. The tag efficiencies are normalized to G1. The errors are $\sim 10\%$.

SVX II Geometry	3 lepton tag efficiency
G1	1.0
G2	1.5
G3	2.4
G4	2.5
G5	4.1

<u>$B \to \psi K_s$ Mode</u>

The cleanest signal at a collider will likely be in the decay $B \to \psi\ K_s$, where the leptonic decay of the ψ provides a clear trigger. We wish to determine our sensitivity to CP violation as a function of luminosity. The analysis of the asymmetry is discussed in many references. [21] The statistical error on the CP violating parameter $\sin 2\beta$ is given by, [21]

$$\delta(\sin 2\beta) = 1/(\sqrt{N}D).$$

The factor N is the number of tagged, reconstructed events given by,

$$\mathcal{L}2\sigma\epsilon_{\psi K}\epsilon_{trig}\epsilon_{tag}\frac{S+B}{S}$$

and the factor D is a product of dilutions due to mixing of the B that decays to ψK_s, the

mixing of the tag, the mistag probability, and the background,

$$\frac{x_d}{1+x_d^2}(1-2\bar{\chi})(1-2w)\frac{S}{S+B}.$$

In these expressions,

$\mathcal{L}$	is the integrated luminosity
σ	is the total $b\bar{b}$ cross section
$\epsilon_{\psi K}$	is the total branching ratio and geometric acceptance for the decay $B \to \psi K_s \to \mu\mu\pi\pi$
S, B	are the signal and background
x_d	is the B_d mixing rate
$\bar{\chi}$	is the averaged B mixing probability
ϵ_{trig}	is the efficiency for triggering and reconstructing the trigger b
ϵ_{tag}	is the tagging efficiency for the second b
w	is the probability of mis-tagging the second b (excluding mixing)

The B_d mixing rate has been well measured at the $\Upsilon(4S)$ with the result, $x_d = 0.72 \pm 0.15$ [22]. The average B mixing probablility has been measured at CDF with the result $\bar{\chi} = 0.176 \pm .045$ and at LEP with the result $\bar{\chi} = 0.13 \pm .01$[23]. These numbers are very precisely known for the purpose of this measurement. Below, we estimate the b cross section and then investigate the remaining parameters which are dependent upon detector performance.

Cross Sections

CDF has measured the inclusive b cross section down to p_T=10.5 GeV/c from reconstructed B decays and, at higher p_T's from inclusive electrons [24]. Based on these measurements, we can extrapolate to lower p_T and higher rapidity and calculate the cross section for the exclusive ψ K_s decay mode.

We use ISAJET (version 6.43) to leading order to generate b events. In order to validate this method of extrapolation, we have compared the calculated cross sections as a function of quark p_T and rapidity y to the complete order α_s^3 calculation of Nason, Dawson, and Ellis (NDE) [25]. Figure 39 shows that the ISAJET p_T distribution agrees well with the NDE calculation, down to p_T's as low as 6 GeV/c. This is sufficiently low for calculating the cross section at the lowest thresholds for a ψ trigger. Figure 39 also shows a direct comparison of the shape of the b quark p_T distribution for b quark rapidity $|y| < 1$ from leading order ISAJET and NDE to the distribution measured with CDF data. The agreement in shape is good, although the low p_T behavior of the cross section is poorly constrained. In this way we normalize the ISJAET cross section to the CDF data in the following calculations.

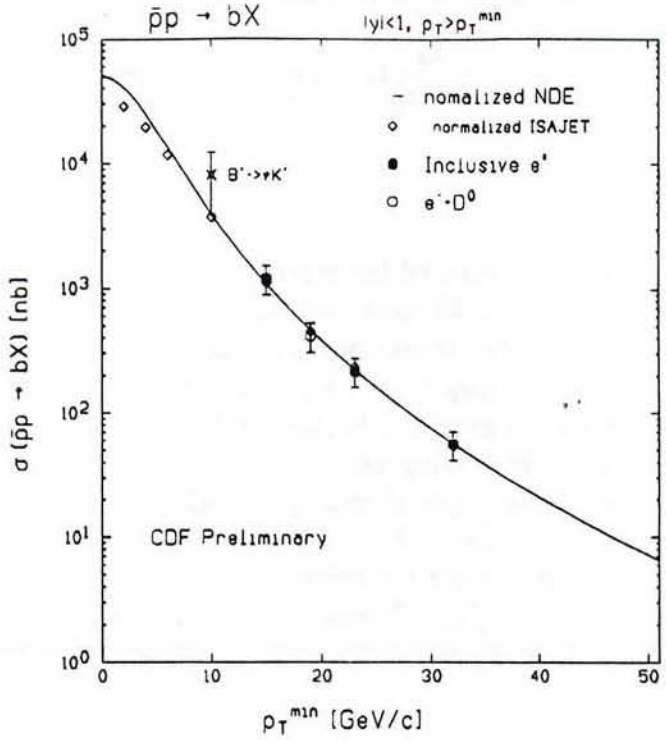

Figure 39: Comparison of the b cross section as a function of quark p_T between ISAJET, NDE, and CDF data. The theoretical calculations have been normalized to fit the data.

The leading order ISAJET cross section as a function of y is compared to NDE in Fig. 40. ISAJET compares well to the higher order calculation except perhaps at large rapidity ($y = 3$). There, ISAJET differs by as much as a factor of 1.75, although the theoretical uncertainties are large.

We have used ISAJET normalized to the CDF data to calculate the cross section for the process $b \rightarrow B \rightarrow \psi K_s \rightarrow \mu\mu\pi\pi$. The product of cross section, total branching ratio (1.34×10^{-5}), and acceptance ($\sigma\epsilon_{\psi K}$) for various acceptances is tabulated in Table 15. The muons were required to have $p_T > 2$ GeV/c and the pions $p_T > 1$ GeV/c, corresponding to realizable trigger thresholds. The cross sections include fragmentation and branching ratios. We see that the expected event rates in a high luminosity data set of the order 1 fb^{-1} are quite high. In addition, it is clear that high η tracking will significantly improve the statistics of the measurement, even given the possible over estimate of the cross section at high rapidity.

Tagging

The flavor (b quantum number) of the B that decays to ψ K_s, can be determined by the flavor of the other b in the event. As a flavor tag we consider the leading lepton (highest

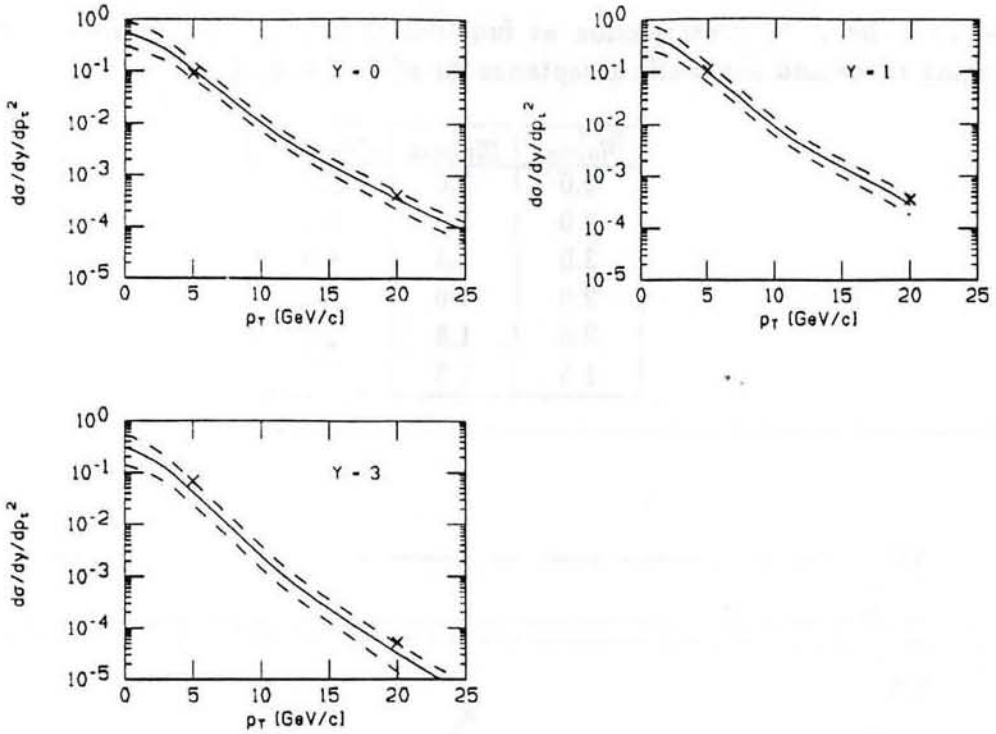

Figure 40: Comparison of the b cross section as a function of quark p_T between ISAJET(crosses) and NDE(line) for η = 0, 1 , and 3. The error bars indicate the size of the theoretical error.

p_T) opposite in azimuth to the trigger B. We then estimate the tag efficiency ϵ_{tag} and mistag probability w from a sample of ISAJET events generated in leading order. It is likely that ISAJET overestimates the strength of the correlations in p_T and azimuthal angle between the two b quarks. As an indication of the dependence of ϵ_{tag} and w on the p_T correlation, we plot in Fig. 41 the tag efficiency for the leading muon, and in Fig. 42 the corresponding mistag probability, with and without p_T cuts applied to the trigger B. The cuts are $p_T > 2$ Gev/c for each of the two muons and $p_T > 1$ Gev/c for the pions. These uncertainties in the Monte Carlo calculation underscore the importance of measuring the tagging efficiency and mistagging probability in the data now being taken with the current SVX.

The ISAJET calculation includes backgrounds from sequential (charm) leptonic decays. An additional background for a muon tag is pion/kaon decays in flight. We model this background in a simple way: we calculate the probability of decay inside of our tracking volume and consider this fraction to be detected as muons. We account for the kinematics of the decay simply by multiplying by an average momentum degredation of 80 %. No attempt is made to model the effects of the decay in flight on the track fitting. Since one might expect some reduction of decay in flight background using tracking information, this is a conservative background estimate. The resulting p_T distribution of the decay muon is very soft, and we expect that it has little effect on the tagging.

Table 15: The ψ K_s cross section as function of $|\eta|_{max}$. The cross section includes all branching ratios and kinematic acceptance for $p_T^{\mu} > 2$ and $p_T^{\pi} > 1$.

$\|\eta_\mu\|_{max}$	$\|\eta_\pi\|_{max}$	$\sigma\epsilon_{\psi K}$ pb
3.0	3.0	15.0
3.0	2.0	11.8
3.0	1.5	9.4
2.0	2.0	10.6
2.0	1.5	9.1
1.5	1.5	7.7

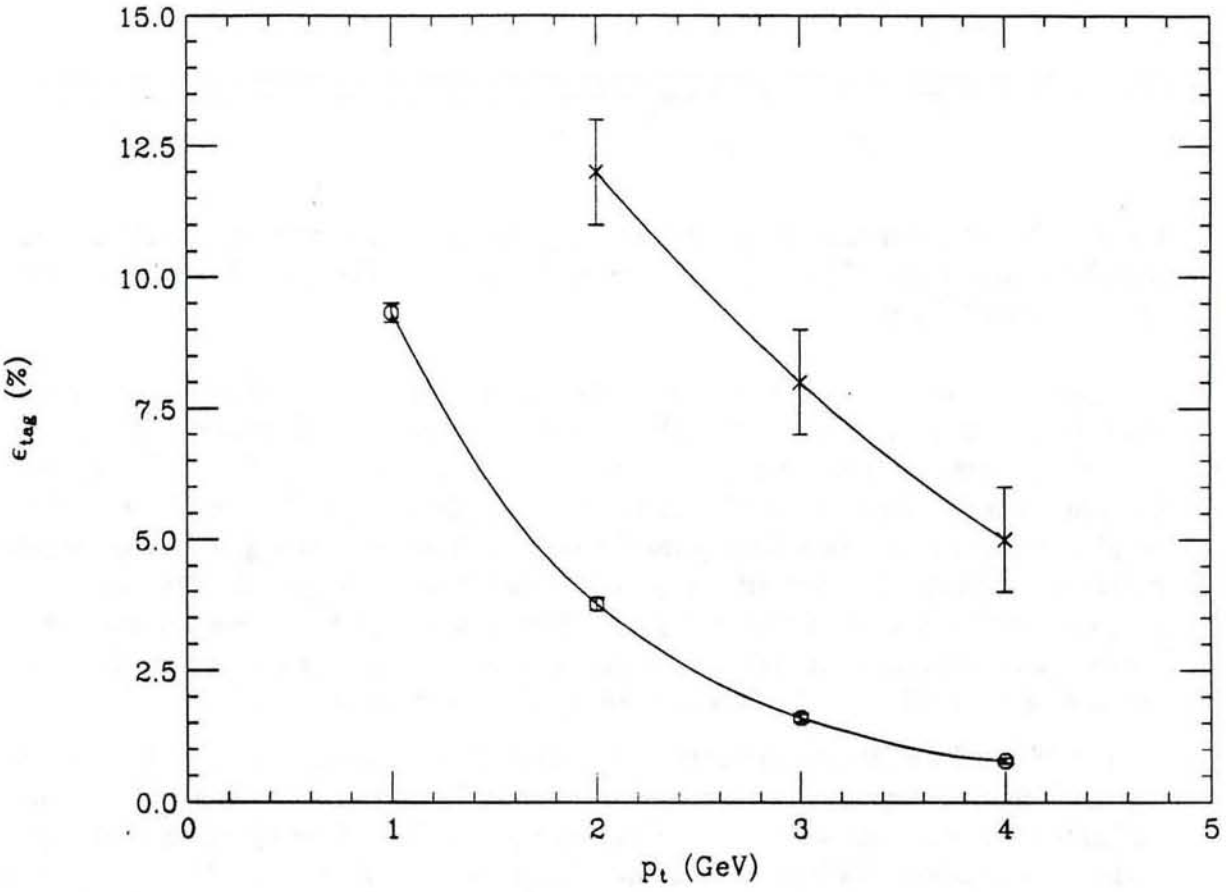

Figure 41: Flavor tag efficiency ϵ_{tag} in percent as a function of the minimum p_T of the muon from b decays. In the upper curve p_T cuts are applied to the trigger B as described in the text. No such cuts are applied in the lower curve.

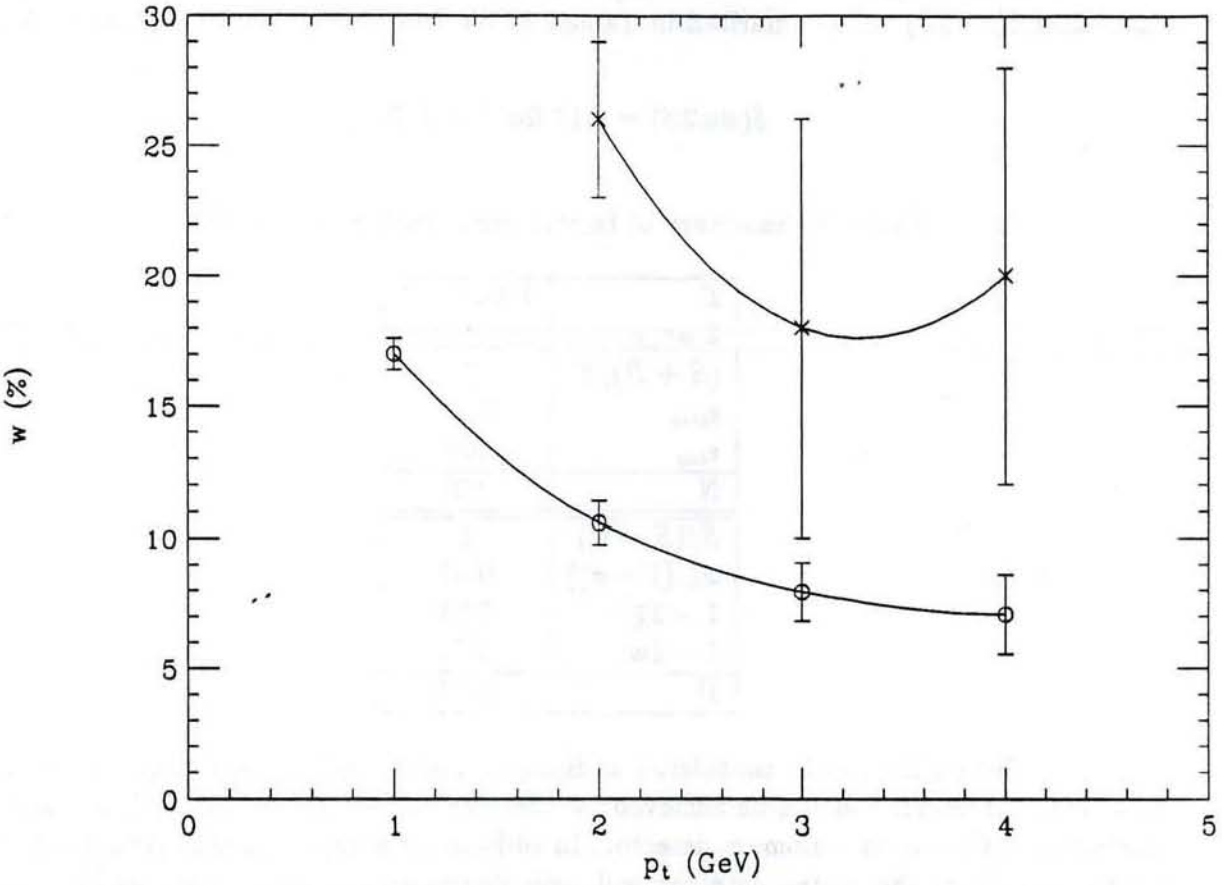

Figure 42: Flavor mistag probability w in percent as a function of the minimum p_T of the muon from b decays. In the upper curve p_T cuts are applied to the trigger B as described in the text. No such cuts are applied in the lower curve.

Sensitivity

We now combine the above results to yield an estimate of the error on the CP violating parameter ($\delta(\sin 2\beta)$). The two remaining parameters we estimate from the CDF measurement of the exclusive reconstruction of $B \to \psi K^{\pm}$ [24]. In this analysis, the ratio of signal to background was 3/1. With the vertex detector we expect a greatly improved signal to background, and so it is reasonable to expect $S/(S+B) \approx 1$ Including improvements expected in the trigger, we estimate $\epsilon_{trig} = 0.35$. The factors leading to the error on the parameter $\delta(\sin 2\beta)$ are summarized in Table 16. We find for a muon with p_T=2 GeV/c,

$$\delta(\sin 2\beta) = 0.18 \text{ for } \mathcal{L} = 1 \text{ fb}^{-1}.$$

Table 16: Summary of factors contributing to $\delta(\sin 2\beta)$.

$\mathcal{L}$	1000 pb^{-1}
$2\ \sigma\epsilon_{\psi K}$	2(15) pb
$(S+B)/S$	1
ϵ_{trig}	0.35
ϵ_{tag}	.04
N	420
$S/(S+B)$	1
$x_d/(1+x_d^2)$	0.47
$1-2\bar{\chi}$	0.74
$1-2w$	0.78
D	0.27

So far we have only considered a dimuon trigger and a muon tag. Efficient, low p_T electron identification can be achieved by effective use of CDF's high position resolution electromagnetic shower maximum detector. In addition, it is expected that precision tracking information from the vertex detector will help distinguish prompt electrons in B decays from backgrounds such as conversions. Furthermore, the planned inclusion of the shower maximum detector in the trigger will allow for an electron psi sample of comparable statistics to the muon sample. Thus, an improvement in the statistics by roughly a factor of four (triggering plus tagging) can reasonably be expected, corresponding to a reduction in the error on $\delta(\sin 2\beta)$ by a factor of two. Finally, we are exploring the possibilities for particle identification and pion-kaon separation to p_T's of $\sim$ 2.5 GeV/c.

$B \to \pi\pi$ Mode

In order to fully test the standard model mechanism for CP violation, it is desirable to search for CP violation in other decay modes that independently constrain the model.

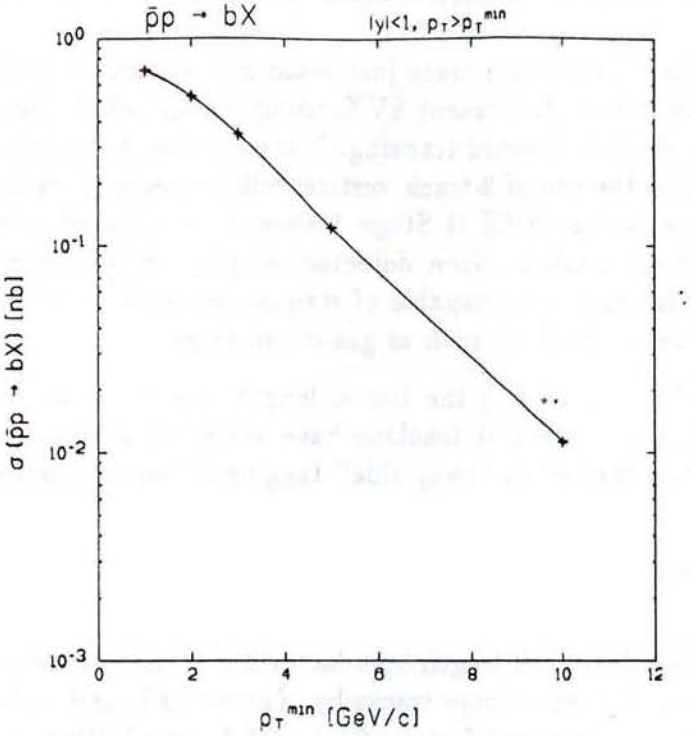

Figure 43: Cross section of $B \to \pi\pi$ as a function of the di-pion p_T threshold. A branching ratio of 1.2×10^{-5} is included. Since the $\bar{b}$ can also decay to $\pi\pi$, a factor of 2 should be used to obtain the total number of $\pi\pi$ events per unit luminosity. A smooth curve has been drawn through the calculated points.

Another such mode is the flavor changing neutral current decay $B \to \pi\pi$ whose branching ratio is expected to be about 2×10^{-5}.[26] It should be noted that this branching ratio is comparable to the product of branching ratios in $B \to \psi K_s \to \mu\mu\pi\pi$ which is 1.34×10^{-5}. Consequently, an equally powerful measurement is conceivable.

Here, one of the principal challenges is triggering. Figure 43 shows the cross section for $B \to \pi\pi$ as a function of the dipion p_T threshold including the branching ratio. Studies have shown that a dipion trigger with threshold of 2 GeV/c can be built with a trigger efficiency of $\approx 6\%$. We see that the cross section is not too steeply falling and one expects the statistics to be enhanced as the trigger efficiency improves with higher p_T. If we assume conservatively a trigger efficiency of 6% we estimate 60,000 $B \to \pi\pi$ events in a 1 fb^{-1} data set. These events can then be tagged via the semi-leptonic decay of the other B. Other challenges for this decay mode include flavor tagging and the separation of signal from combinatoric and πK background in identifying the trigger B.

5.8 Summary of Simulation Studies

These simulation studies illustrate just some of the improvements to be gained by doubling the barrel length over the present SVX, using double-sided silicon detectors, and by adding the disks or equivalent forward tracking. It is expected that additional benefits in background rejection, and in the use of 2-track vertices will be realized with the 3D vertex information. Our conclusion is that SVX II Stage 1 should be a barrel geometry, about one meter in length, with double sided silicon detectors employing 90° stereo. An upgrade path (Stage 2) would add forward disks capable of standalone tracking, either using silicon detectors or possibly another technology such as gas microstrips.

The benefit of extending the barrel length is seen in all the physics considered. The improvements due to the disk tracking have less effect on top but benefit b physics, and this is especially the case when "away-side" tagging is required because extended η coverage is essential.

In Summary:

1. Extending the barrel length by a factor 2 increases the number of top events tagged by a b vertex of three or more tracks by of order 50%, and making the barrels double-sided provides an additional factor of 1.1 to 1.3. In addition the double-sided readout will allow 2-track vertices to be used as a tag.

2. The rejection of $W+$ jets events in a top search gives a factor 40 improvement in signal to background using 2D vertexing over no vertex information. The improvement can be even larger for 3D vertexing.

3. The improved capability for identifying the b vertices provides a significant reduction in the jet-combinatorial backgrounds in studying top decays.

4. The improved momentum resolution achieved with the SVX makes the muon channel in W decay competitive with the electron channel for the W mass measurement. In addition in the W' search the improvement in the muon momentum resolution may be the difference between a discovery and a limit. The Stage 2 disk upgrade is needed for the W asymmetry measurement.

5. A large increase in B acceptance is achieved by doubling the barrel length, and a further increase of comparable size is achieved by adding disks for forward tracking. For single B decays the combined increase is about a factor of 3 over the present SVX. For accepting all the tracks from both B's the combined increase is a factor of 5.

6. Requiring a 3σ impact parameter cut on all three leptons, the acceptance for the lepton tagged ψK_s sample increases by 50% when the length of the present SVX is doubled, and the addition of the disks gives a further 70% increase. For these impact parameter cuts, a double-sided detector gains an additional 60% in acceptance.

7. The mass resolution improves with the addition of SVX information, with a 3D measurement providing a further improvement over 2D. The mass resolution begins to degrade with track pseudorapidity above $|\eta| = 1.5$.

8. The vertex resolution of the barrel system allows the efficient isolation of B decay vertices and the detailed measurement of the B decay distribution, even for modes including cascade decays through charm.

9. Our initial estimates of the capability of SVX II to measure B_s mixing and CP violation show that CDF will be able to provide significant results for these challenging measurements.

In conclusion the long barrel double-sided SVX II Stage 1 detector will be a powerful tool for the exploration of high p_T physics, and for extending the b physics capabilities. The evolution toward a more comprehensive b physics program will be accomplished in part by the addition of forward tracking in Stage 2.

6 SVX II Mechanical Engineering and Design

6.1 General description

The SVX II detector will be arranged in three identical barrel modules mounted symmetrically with respect to the interaction point (Figure 44). Each barrel will cover a region approximately 34 cm long in z, and will consist of four radial layers of detector ladders. Each ladder will consist of four silicon detectors mounted together into a single mechanical unit, and wirebonded electrically in pairs which are read out at each end of the ladder.

The ladder support structure will maintain detector-to-detector alignment to within ± 5 microns in the r-ϕ direction and provide sufficient stiffness and thermal stability to eliminate gravitational and thermal mechanical bowing. The maximum amount of intrinsic bow in the ladder support structure after construction will be kept to less than 50 microns and be measured to an accuracy of $\pm$ 10 microns. A tight tolerance on the radial uncertainty of the detectors is important for the orthogonal stereo angle double-sided detectors used in SVX II, since for tracks at large incident angles, there is a strong coupling between the radial and z position uncertainties. The z position uncertainty in the placement of the detectors during the ladder construction process will also be $\pm$ 10 microns. All of the ladder designs we are pursuing will be able to achieve these tolerances.

The ladders will be arranged in wedges in a 12-sided geometry. Each wedge will span slightly more than 30 degrees, and in the present design the wedges are staggered in radius with respect to each other in order to provide a small amount of overlap. This is shown in Figure 45. This staggered radius geometry will simplify the barrel construction and will allow additional overlap between neighboring wedges compared to the SVX and SVX′ detectors. The optimum mechanical length of the individual silicon detectors is still being explored. With four detectors of 8.5 cm length in each barrel, the total SVX II detector length will be 1.020 meters. The SVX II barrel geometry is shown in Figure 46.

In SVX, laser-drilled holes in the hybrid circuit boards at each end of the ladder were used to define a reference line to which the silicon detectors were aligned with a 5 micron accuracy. The same approach will be taken with SVX II, except that the reference feature will be masked onto the hybrid, and the hybrid will be mounted on the silicon surface. This design will achieve less dead space between the neighboring barrels than in SVX. The SVX dead space between barrels was 4 cm whereas the goal for SVX II (including space for readout cables) will be 1.5 cm or less.

Overall construction tolerances for SVX II will be similar to those achieved in the construction of SVX. A flex test of a layer 1 ladder from SVX revealed an equivalent "specific stiffness" of the composite (see Table 17), and a theoretical center deflection of 12 microns. The SVX II ladder design is 8.5 cm longer than SVX and the ladders may need to be somewhat stiffer, but the 50 micron bow limit should be achievable with either of the two ladder designs being considered below.

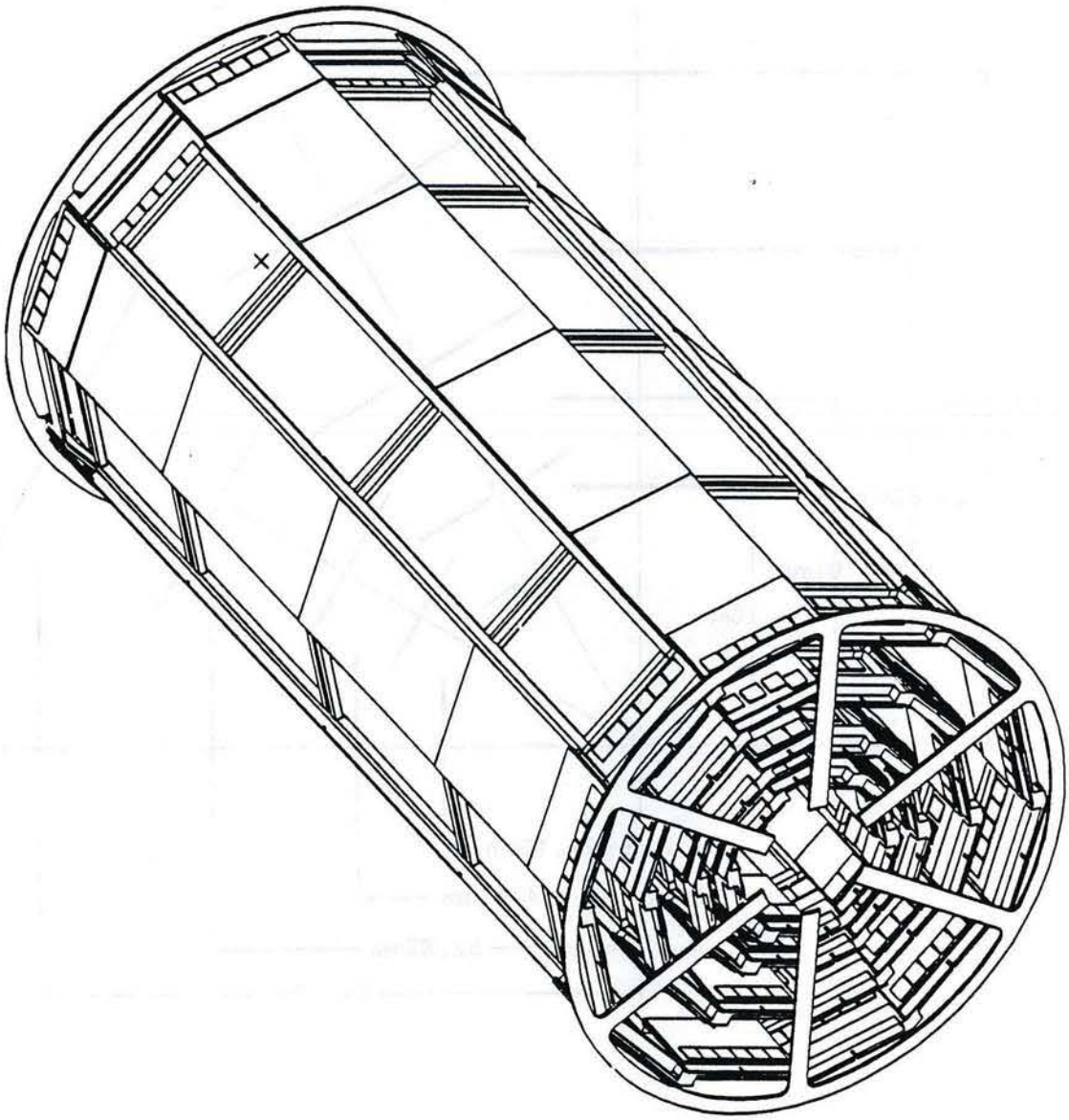

Figure 44: The CDF SVX II detector.

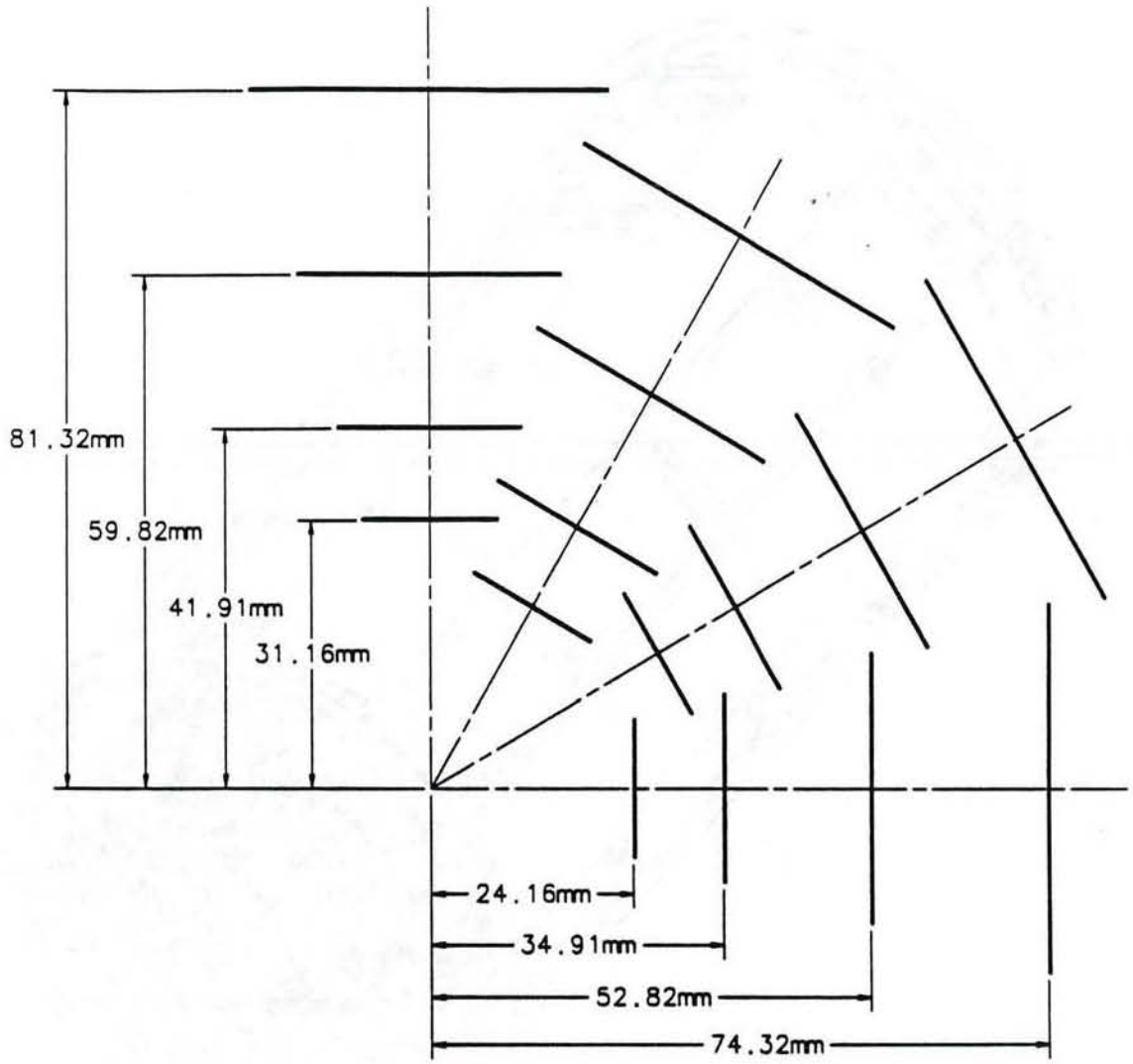

Figure 45: The staggered radius geometry in one quadrant of the SVX II detector.

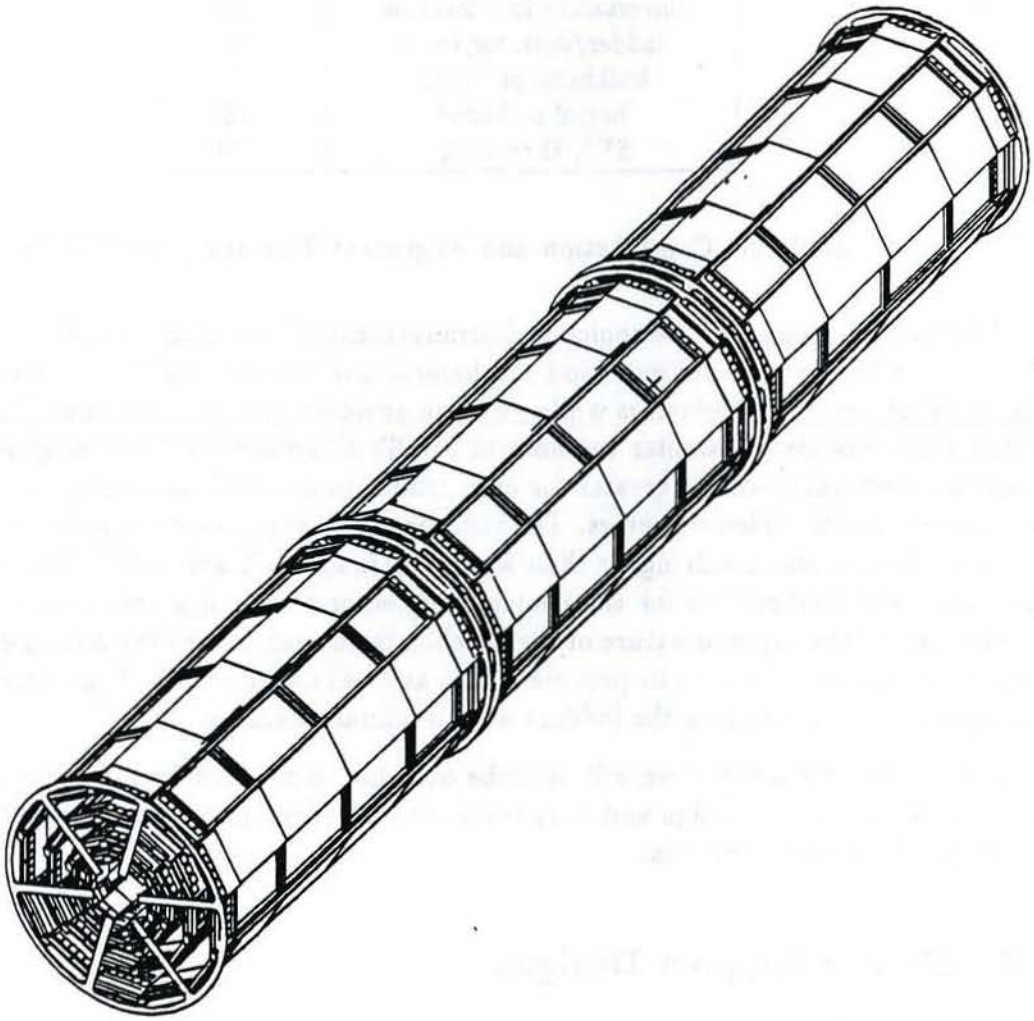

Figure 46: SVX II barrel geometry.

Quantity	Tolerance
detector thickness	± 10 micron
detector-to-detector alignment	5
maximum bow	50
uncertainty in bow	10
uncertainty in z location	10
ladder/detector twist	25
bulkhead precision	15
barrel to barrel	200
SVX II to CTC	200

Table 17: Construction and Alignment Tolerances for SVX II

The main challenge for the choice and arrangement of materials for the internal structure of SVX II is the need to achieve good mechanical and thermal stability in the location and alignment of the silicon detectors while using an absolute minimum amount of material. The design requirements are similar to those of the SVX, however the power generated by the front-end electronics will be greater for each ladder because of the additional channels read out from the double-sided detectors. The radiation dose expected during the detector lifetime (up to 1 Mrad) is also much higher than was the case for SVX and SVX′. This high radiation dose will have implications for the choice of detector electronics and structural materials. Finally, due to the exposed nature of the wirebonds on each side of the double-sided detector ladders, it will be necessary to provide a safe and reliable method of constructing, testing, mounting, and dismounting the ladders with minimal handling.

In the following sections we will describe our plan to proceed from the experience gained in the SVX mechanical design and construction to a design appropriate for SVX II, including all of the above considerations.

6.2 Ladder Support Designs

As described before, the silicon detectors are attached together and supported by a low-mass structural support. This support serves not only to combine the four silicon detectors together into a ladder structure, but also to hold the silicon flat by helping to remove any local bowing produced in the detectors during processing. The two support designs presently receiving serious consideration are:

1. Single-piece edge rails, as used in the Los Alamos design for the SDC silicon tracker;
2. Rohacell/Carbon Fiber Reinforced Plastic (CFRP) composite ladders, as used in the SVX and SVX′.

In both designs we have the option to edge bond the silicon detectors together at their ends in order to join them during assembly into a single mechanical unit. This edge bonding might provide sufficient strength to the detectors to perform the wirebonding prior to attaching the ladder support structure. This is not absolutely necessary in all assembly scenarios, however. The epoxy edge bond, if used, would help to provide stiffness at the joint for the wirebonding and would allow the wafer assembly to be moved after wirebonding and before attachment of the support structure.

Given the two sided wirebonding requirements of the SVX II, the alternative to edge bonding the silicon is to support the detectors on a vacuum fixture for the first side wirebonding, then affix the ladder support structure and wirebond the other side. We have found experimentally during the assembly process for SVX that with careful attention to the process used in gluing together the ladders, much of the residual bowing that may be present in a particular silicon detector can be taken out during the ladder construction. Consequently, careful attention to this step will be required. The final fabrication method will be determined by performing the appropriate tests with the wirebonder to become more familiar with its capabilities and detector support requirements.

In the SVX construction, the silicon load was transferred through the ladder to the readout hybrid and then to the bulkhead. At no point was the silicon part of the load bearing structure. For the SVX II, however, with the double sided detectors and associated front-end electronics, the silicon and hybrids become an integral part of the support mechanism due to the fact that the hybrids are mounted directly on the silicon. Extensive modeling and testing will be conducted to ensure that this will not induce excessive stresses in the silicon.

Edge Rail Design

The edge rail design consists of a rectangular CFRP piece being bonded to the side edges of the silicon detectors during the ladder construction (Figure 47). The stiffness of the ladder depends on the cube of the height of this rail, which for the materials we are considering, will lead to an edge rail height of several millimeters. This design must accomodate such relatively large rails between silicon layers without interference and with sufficient mounting clearance.

The rails will most likely be attached after the wirebonding is performed on both sides. As described above, either edge bonding or the appropriate fixturing will be required to achieve the double sided wirebonding since it is unlikely the wirebonder head could get close enough to the silicon edge to bond the outer pads with the rails already attached. Prototyping work has begun to determine the feasibility of edge bonding the silicon detectors together. A vacuum chuck has been built and attempts are underway to perform these edge bonds. The first effort will be to learn how to successfully epoxy edge bond the detectors and then to measure the reliability and strength of the bonds under mechanical and thermal loads as well as after radiation exposure.

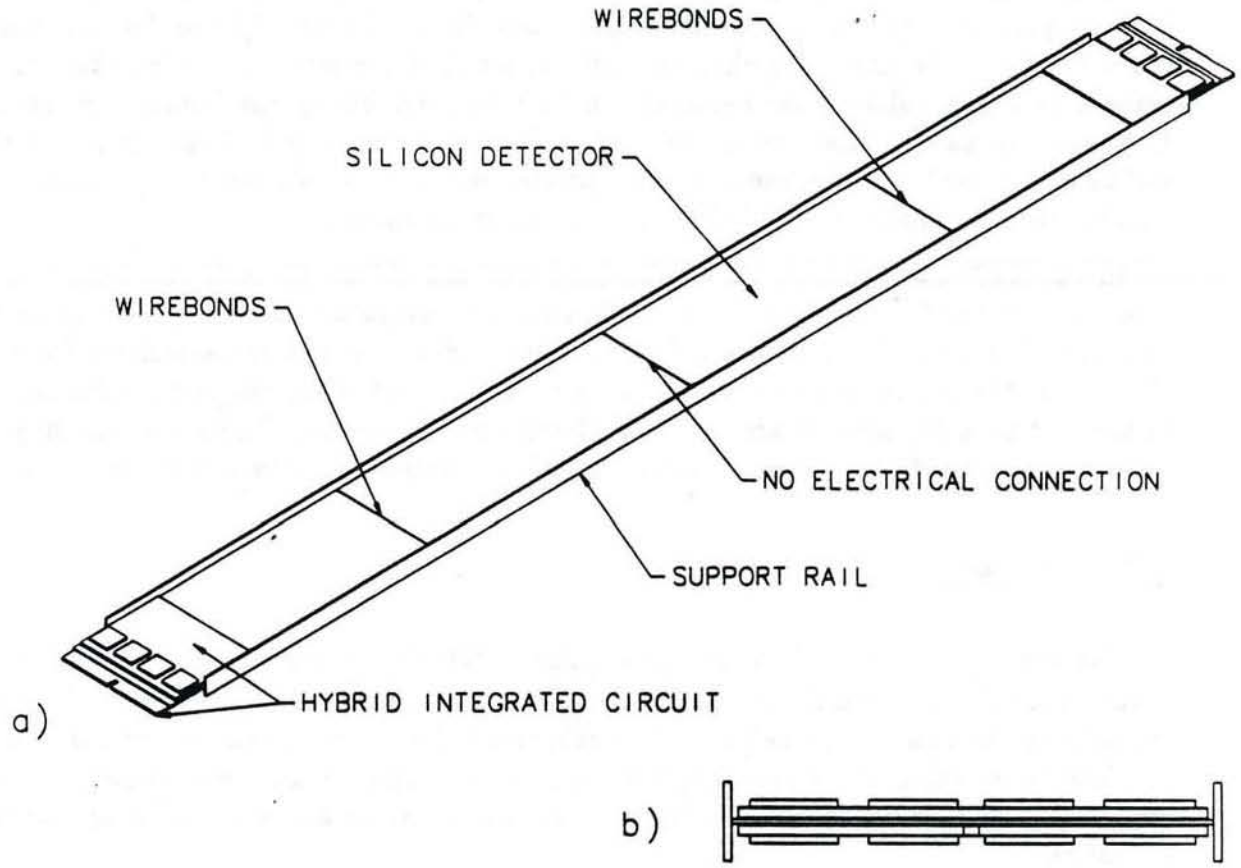

Figure 47: (a) Schematic and (b) cross-sectional views of the SVX II edge rail ladder design.

A second vacuum chuck will be built to hold the edge rails and enable gluing the silicon to them while maintaining a 90 degree angle. These rails will be mechanically tested for adherence to the above mentioned specifications. In addition, the experience of the Los Alamos group in developing the edge rail ladder design for the SDC silicon tracker will be used extensive in evaluating its usefulness for the SVX II detector.

Composite Ladder Design

The composite SVX-style ladder (Figure 48) is the second support option being considered. The materials to produce this ladder are the same as used in SVX, but the design is slightly different. The CFRP would need to be recessed to enable cutting away portions of the Rohacell to provide clearance for the wirebonding. The ladder would stop short of the end of the structure and, as in the rail design, the silicon/hybrid would carry the load to the bulkhead.

This support, if mounted only on one side of the silicon, would be mechanically asymmetrical, i.e. not the same on the top and bottom of the silicon itself. This could lead to thermal distortions if the operating temperature is different than that of the fabrication temperature, a condition which could well occur. In order to avoid this condition, the ladders could be built of materials whose composite coefficient of thermal expansion (CTE) is matched to that of the silicon. This was done reasonably successfully in SVX.

Alternatively, the support could be designed to be lighter weight and mounted on both sides of the silicon. One side of the ladders would be affixed to the silicon immediately after the wirebonding stage for the first side. The ladder would then be flipped, and with proper fixturing, the second side would be wirebonded. Prior to constructing full-scale prototyping fixtures, an analytical approach to composite structures is being developed to assist in determining the most suitable ladder composite structures. The analytical calculations are being verified by flex testing different combinations of composite cross-sections.

Materials

A list has been compiled (see Table 18) giving properties of interest for several candidate materials for the ladder structure. The specific stiffness has been determined, where possible, by flex testing the material at Fermilab. The ladder material must have a high specific stiffness and the appropriate geometry to achieve the above stated construction and alignment tolerances.

The SVX ladder was a composite structure made of carbon fiber and polyimide foam which exhibited an equivalent specific stiffness and flexural modulus of elasticity given in Table 18. Due to the increased length of the ladders in SVX II, investigation of variations on this design are being pursued.

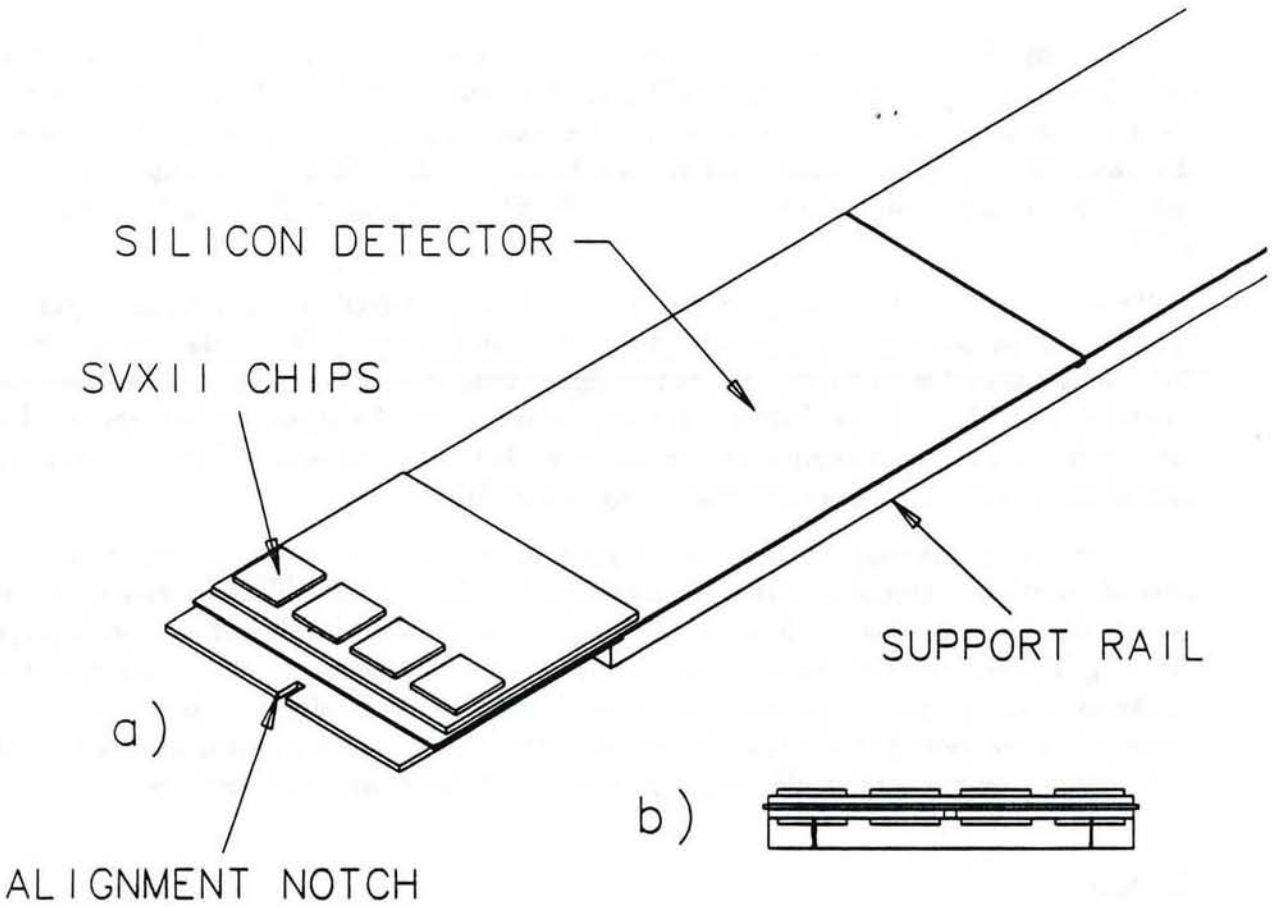

Figure 48: (a) Close-up and (b) cross-sectional views of the SVX II composite ladder design.

Table 18: Material Properties

Materials	Specific Stiff. (10^7 cm)	Radiation length (cm)	CTE (ppm $\frac{1}{^\circ C}$)	Thermal cond.($\frac{W}{m\ ^\circ C}$)	Flexural Mod. (10^9 Pa)	Dens ($\frac{kg}{m^3}$)
SVX rails	49.7	208	?	?	10.4	213
Beryllium	160	35.4	11.6	180	290	1840
B/Epoxy 5521	97	21.6	4.5	?	190	2000
Silicon	57.4	9.37	2.6	129	131	2330
CFRP	60-180	28	≈ 0	4.9	100-300	1600
Aluminum	25.4	8.89	23.6	168	68.9	2700

Studies are underway as described below to investigate the performance of this design as a function of the choice of composite materials, dimensions, and placement in order to meet the increased stiffness requirements for SVX II.

The ladder material must not only have a long radiation length, but must remain stable in a high radiation environment. The selected ladder material will be thoroughly tested for mechanical stability under such conditions.

Compatibility with the surrounding environment will be thoroughly checked. Various epoxies and bonding agents will be used in the construction of SVX II. These materials will be checked for outgassing and purity to ensure compatibility with the silicon detectors and front-end electronics.

Thermal stability must be assured for our design as well. Materials with a low linear coefficient of expansion near that of silicon can be used in the rail supports in order to reduce thermal stresses in the silicon. The addition of a thin insulating layer between the silicon and the hybrid and good thermal contact between the hybrid and the bulkhead will channel the heat from the front-end electronics away from the silicon and into the cooling system.

6.3 Bulkhead structure

The bulkhead structure has to mechanically support the ladders, provide a suitable and stable structure for ladder alignment, and act as the cooling interface for the front-end electronics. The best material for such support is beryllium because it is light weight, has a high radiation length, and can be machined to tight tolerances.

In the SVX design, each bulkhead was machined from a single piece of beryllium stock, which was stress-relieved several times by annealing during the machining process in order to achieve the best possible results. Precisions on the order of 12 microns or less deviation from the ideal were typically achieved. This is well within the requirements for SVX II.

The basic design of the SVX bulkhead was an array of radial spokes which supported and connected the circumferential support ledges for the four silicon layers. An aluminum cooling tube was glued to the beryllium bulkhead for each layer. In order to improve the thermal contact between the cooling channel and the electronics for SVX II, we are instead considering a number of designs which have cooling channels machined directly into the material of the bulkhead. An example of such a design is shown in Figure 49. The channels in each bulkhead would be fed by small tubes on the reverse side, and closed at their front surfaces by cap rings which would be brazed on, sealed, and tested. This avoids having to glue a channel of different material into the bulkhead, thus minimizing thermal stress and improving thermal contact. Because the cooling load per detector will be approximately double that in SVX, this is an important consideration. Further details on cooling needs are discussed below.

Alignment reference features will also be incorporated into the cooling channel support members in the bulkhead for use during the ladder installation and alignment survey. In order to achieve the best possible accuracy, these will be arranged so that all of the precise machining can be done on one face of the bulkhead only, after removal of non-crucial material from the reverse face in preparation for this step.

SVX II Heat Load

Table 19 gives the expected heat load for the SVX II. At 2 mW per channel, the expected power generated by the front-end electronics is 256 mW per chip. To introduce a factor of safety into the cooling design and to account for other elements on the hybrid, we have used a larger number of 400 mW per chip. The heat load for SVX II is reported in Table 19.

The cooling will be provided with water pumped through tubes (aluminum or beryllium) in direct thermal contact with the electronics. Complete thermal analyses and modeling are being performed.

The chip power density (1.1 Watt/cm^2) is high enough to be of concern, but within the domain of water cooling schemes. Water in the laminar flow region in a cooling channel of modest dimensions will provide enough heat transfer to cool the electronics and maintain the alignment of the structure. The anticipated heat load of 270 Watts per barrel can be removed while maintaining a temperature rise of $\leq 1\ ^{\circ}C$ within the water coolant by a flow rate of 64 grams/second. To keep the flow in the laminar region, the minimum cooling channel dimensions for this flow rate are on the order of a few square millimeters. Careful selection and routing of flow channels will enable minimization of the channel dimensions. For instance, layer number 4 has 36% of the total heat load. By splitting the flow into two

Table 19: SVX II Thermal Load per Barrel

Layer #	r-ϕ chips per ladder end	r-z chips per ladder end	Total load per ladder end (W)	Total per layer (W)
1	2	2	1.6	38.4
2	3	3	2.4	57.6
3	4	4	3.2	76.8
4	6	4	4.0	96.0
Total power per barrel				270 Watts

branches, a rectangular channel of 1 mm by 5 mm would provide both sufficient heat transfer surface area and a sufficient hydraulic diameter. Further thermal analysis will be performed to optimize the location and dimensions of the bulkhead members and cooling channel from the point of view of the total mass inventory.

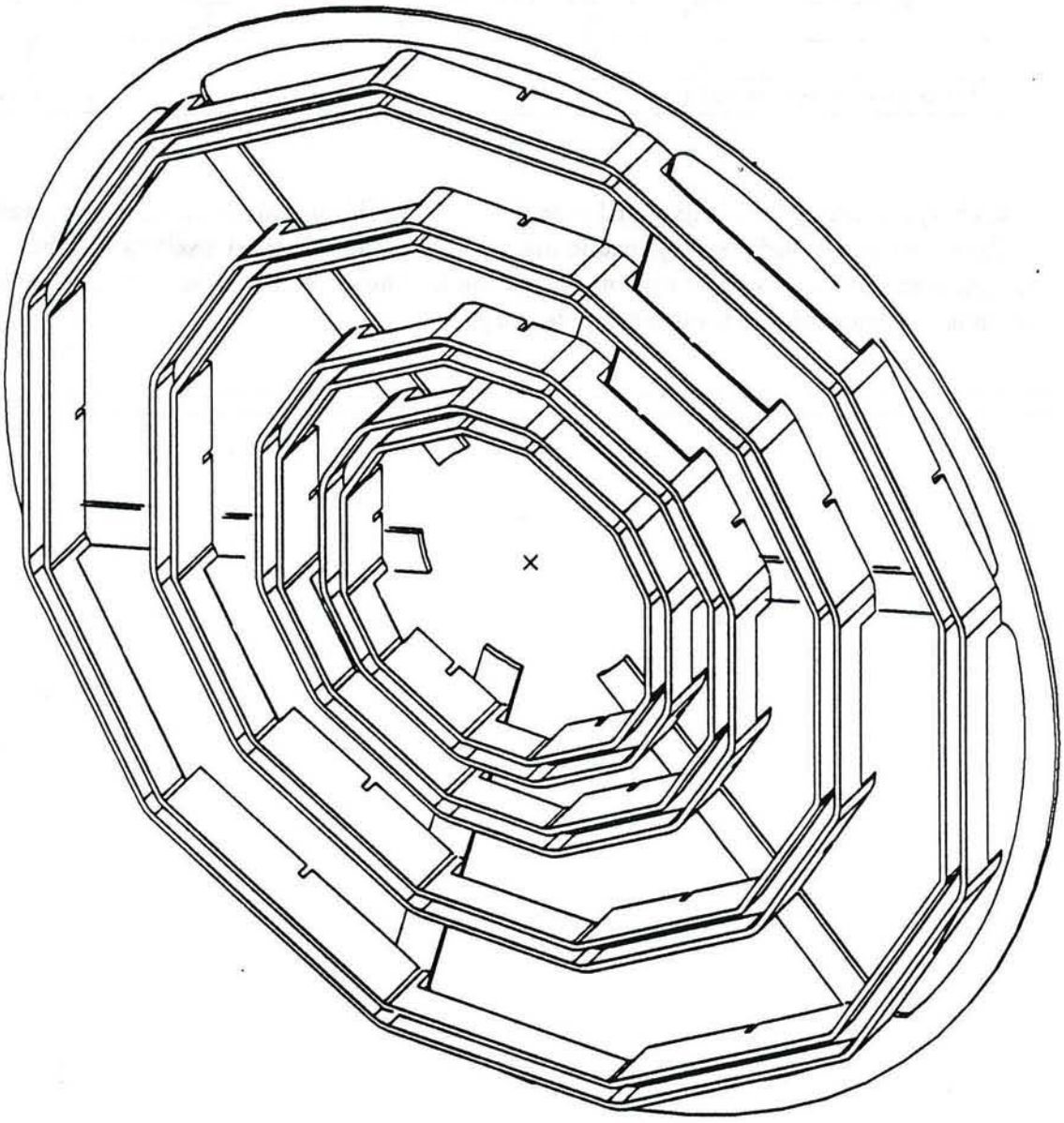

Figure 49: SVX II bulkhead design, showing the cooling channel integrated into the ladder mounting ledges before the cap rings and feed tubes are attached.

6.4 Hybrid Mechanical Considerations

Each front-end readout package will consist of a mechanically-supporting, thermally-conductive dielectric substrate with an electrically conductive pattern, two or more active SVX II readout chips, and several passive surface mount capacitors to provide bypassing and power filtering. The complete package with active and passive components attached is referred to as a Hybrid Integrated Circuit (HIC).

Each end of a ladder will have two such HICs mounted directly to the top and bottom surfaces of the silicon. Since the readout density on each of the four barrel layers is approximately the same for each layer, more SVX ICs are needed on the outer layer ladders. However, the hybrid design is very likely to be the same (or very similar) on each side, r-ϕ or r-z, of the silicon detectors for each layer. Thus only four (or at most eight) variations of a similar hybrid design are required. For any of the possible substrate options for these hybrid circuits, thermal contact with the cooling channels is an important design issue.

Hybrid Substrate Options

There are a number of packaging and interconnection variations that will provide solutions for the SVX II readout needs. Three packaging proposals and two interconnection schemes are being considered: (1) Thick Film, similar to that used in the SVX and SVX′, (2) Laminated Composite, and (3) Thin Film technology.

The thick film substrate designs used in SVX and SVX′ had approximately 15 layers of fired conductive and dielectric material. The packaging density involved 150 micron paths on a 300 micron pitch. To provide signal isolation and crosstalk reduction, signal routing was placed under the IC device sites within the substrate.

An alternative laminate packaging option uses a multilayer kapton film as both substrate and readout cable. Here, all connective metallization is patterned on kapton polyimide film, and this film is laminated onto a thermally conductive substrate whose primary function is to provide for mechanical and thermal support. An obvious advantage of this packaging is the absence of a connector between the hybrid and the subsequent readout cable. The kapton laminate film can be designed to be thinner where the ICs are placed in order to improve thermal performance. Alternatively, windows could be made in the kapton at the IC sites so that the ICs can be mounted directly on a supporting thermally conductive substrate. The kapton routing density that can presently be achieved is 125 micron paths on 250 micron pitch.

The third packaging option is for a multilayer polymer thin film design that would take advantage of photolithographic pattern generation to provide for high density, high performance connection of the active and passive components on the hybrid circuit. Current practical technologies can achieve a routing density of 75 microns on 150 micron pitch. This would be approximately four times the density of the present thick-film design. A hybrid

circuit appopriate to the SVX II could thus be achieved in approximately four to six layers. Current limits on this technology are approaching this number of layers.

6.5 Readout Cables and Routing

Connection between the electronics and the external data acquisition system was achieved in the SVX via laminated copper/kapton cables. These 23-line cables interconnect the hybrids on a parallel bus structure with additional driver cards for the readout. A similar system could be used in the SVX II. In this case, either the thick or thin film hybrid designs will require an appropriate scheme for connecting to the readout cables.

An alternative readout scheme also being pursued uses an optical interface between the hybrid circuits and the driver card. The current view is that each readout chip will have a serial output through a locally mounted LED optical transmitter, with one serial optical data link for each of its ICs plus two optical clock and trigger function receivers per hybrid.

Routing of the optical cables could be somewhat simpler than for the all-copper/kapton design since there would be only one serial optical output per chip. This optical line could be routed directly between the readout IC and the driver card (if any), or to an optical/analog interface. Both designs are proceeding at this time.

6.6 Prototyping/Testing

Several aspects of the engineering of the mechanical system as described above are beyond the initial conceptual stage and are already being subjected to tests in the laboratory to refine features of the design. These are described below.

Si Edge Bonding

As mentioned previously, we are pursuing the edge bonding of silicon detectors. A vacuum fixture has been built to hold two detectors while a heater is suspended above the bond to cure the epoxy. If successful, edge bonding the detectors could provide a means of temporarily holding them together for wirebonding.

Once the edge bonding technique has been perfected and is repeatable, we will aluminize some silicon test pieces near their edges in order to be wirebonded. These metallized surfaces will act as the pads and provide us with a surface to microbond. If the temperatures attained during the edge bonding are excessive to the point of damaging the metallized surface, we may learn this important fact prior to edge bonding actual silicon detectors.

Ultimately the goal is to derive a method of fabricating the ladders to be used in SVX II. Silicon edge bonding could provide a temporary structure, allowing wirebonding on one or both sides prior to affixing support rails.

Edge Rail Prototyping

The edge rails are constructed of carbon fiber reinforced plastic. A fixture will be built to hold the rail while the silicon is bonded to it. These prototypes will be flex tested to determine how they conform with theory, and provide useful information in the design iteration process.

Whether the silicon will require to be first edge bonded has yet to be addressed. It may be possible, with the proper fixturing, to perform the wirebonding while the silicon is held only in a vacuum fixture. The support rails would be attached after the wirebonding is completed. The other option is to determine if it is feasible to wirebond after the rails have been attached to the silicon by studying the operating characteristics of the wirebonder head.

Composite Structure

Several prototype composite rail supports based on the SVX ladder are also being pursued. Fixturing has been fabricated to produce three styles of composite structures. These will be flex tested to determine the CFRP modulus. This process should provide sufficient information to design a new ladder which will meet the stringent requirements of the SVX II.

The final ladder design will, to a great extent, be determined from the results of the prototype testing. In addition to the flexural strength of the structure, the fixturing and handling of the ladder during the fabrication process are important.

By building the centroid of the support structure at the same location as that of the silicon, thermally induced bending moments (in theory) can be made to be less important. If it is not possible to build a symmetrical cross section, the CTE of the support ladders must be near that of the silicon to minimize thermal stresses. Regardless of the support design, stresses in the silicon will be reduced by attempting to match the CTE of the support with that of silicon.

Materials chosen for the ladder will require radiation testing. The materials will be irradiated and tested for changes in their mechanical properties.

6.7 Support of SVX II within the VTX

Since the SVX II will consist of three mechanical barrel units instead of the present two, it will be necessary to split the VTX along a different boundaries than the present center gap at $z = 0$. Our present plan is to assemble the VTX in three sections, with the SVX II residing primarily in the central section of the VTX. Two options have been identified which meet the requirements for support of the cable pathways and cooling lines and still provide sensible

methods for installation and removal. These will be pursued with appropriate engineering support within CDF so that a decision between them can be reached.

The first method calls for separation of the VTX into asymmetric pieces, one of which will hold just one module of the SVX II, and the other holding the remaining two. In order to permit cables to be dressed properly to the outside, the larger of the VTX modules would be itself split into two sections, with a temporary gap at the extreme end of the SVX modules. These two sections would be assembled together prior to installation into the experiment.

The second method would place all three SVX II barrel modules together as one unit mounted into a central section of the VTX which would be just long enough to carry that unit. This would be more attractive from an installation and maintenance point of view, but would involve extended sections of SVX II and VTX cables which would have to be supported (at least temporarily) by external means during installation and removal of the remaining VTX end sections.

The design for both of these options is proceeding, with a decision to be made within the next year.

7 Silicon Microstrip Detectors

7.1 Description of the Detectors

The barrel of the SVX II will be constructed from double-sided detectors made with high resistivity n-type bulk silicon of thickness 300 μm. The exact dimensions of these rectangular devices depend upon the barrel layer in which they are located, but a typical device has an active area which is between 10 and 20 cm^2. The electrical specifications will be guided by research being carried out by the DELPHI and CLEO collaborations and by our experience working with prototype detectors.

The $r-\phi$ measurement will be made with the p-side. On that side, charge will be collected by longitudinal strips with 25 μm pitch. The 5 μm-wide implant strips will be capacitively coupled to each other, and alternate ones will be read out. The strips will be coupled to the readout by a thin (typically 0.2 μm) layer of silicon dioxide and an aluminum electrode. To minimize the capacitance of the side, the aluminum strip will be as narrow as possible while guaranteeing electrical continuity and while maintaining sufficient capacitance to the implant strips. Polysilicon resistors will be used for biasing because of their radiation resistance.

The z measurement will be made by transverse strips on the n-side. As with the p-side, the strips will be AC-coupled to the readout, the biasing will be polysilicon, and the implant and aluminum strip widths will be minimized.

The SVX II mechanical design will be simplified by reading out both sides of the detector at the same edge. We plan to use the "double metal" technique, in which each n-side transverse aluminum strip (the "first metal") is coupled by an aluminum via through a relatively thick insulator to a longitudinal metal strip (the "second metal") which lies on the detector surface. In an alternative to the double metal technology, signals from the transverse strips can be routed to the readout chips with an adhesive Kapton foil bearing copper laminated strips.

The details of the design of the ohmic side strongly affect that side's capacitance. In the case of the double metal technology, the ways to minimize the capacitance are by reducing the second metal's linewidth (and hence the overlap area with the strips of the first metal) and by maximizing the amount of dielectric between the two metals. At present the material with the best dielectric properties (in particular, radiation resistance) is polyimide.

The presence of positive charge at the Si-SiO_2 interface makes it necessary to isolate the strips on the n-side. This is because the positive charge attracts electrons in the bulk to the interface, where they spread out under the influence of the positive voltage on the n^+-strips, effectively short circuiting the strips. Manufacturers use two methods for isolating the n-implants—field plates and p-implants. We are presently investigating the capacitance, radiation hardness, and ease of operation of both in order to choose between them.

Two readout pitches–111 μm and 166 μm–result naturally from the use on this side of 85

mm-long detectors and an integer number of readout chips (with 128 channels per chip). In the preferred design, Layers 1, 3, and 4 will have 166 μm n-side pitch, and Layer 2 will have 111 μm n-side pitch, with all channels being read out. We will also investigate detectors with the pitch of the implants at half the values listed above, but with alternate channels read out. The use of 90° stereo strips with these pitches on a rectangular detector naturally results in the assignment of multiple sense strips to the same metal strip. The multiplexing ambiguities can lead to reconstruction of unphysical tracks known as ghost tracks. The detector pitch and dimensions are being selected so that the ghost tracks are identifiable with the aid of the pointing resolution of the outer tracking.

7.2 Technical Issues Shaping the Design

The parameters of the SVX II detector which have the greatest impact on its physics capabilities are its acceptance and position resolution. In turn the position resolution is related to the detector signal-to-noise ratio. The acceptance of the proposed geometry of the SVX II has been discussed elsewhere in this document. Extensive work is underway to simulate and measure the resolution and capacitance of silicon devices similar to the one whose properties are outlined above. This work is described below.

Z Resolution

It has been shown earlier that good resolution in z can impact the SVX II physics capabilities. In particular, simulations have indicated that the following can be expected upon replacement of a G2 geometry detector by a G3 geometry detector (with z resolution varying between 20 and 50 μm over the range in angles 0–1.35 radians with respect to the normal):

1. The efficiency for B tagging of top improves from 50% to 63% (for $m_{\rm top} = 130$ GeV/c^2) and from 64% to 73% (for $m_{\rm top} = 200$ GeV/c^2).

2. The relative tagging efficiency for events containing two B's, where one decays via $B \rightarrow e$ / μ ν X and the other decays via $B \rightarrow J/\psi\ K^0_s(J/\psi \rightarrow \mu^+\mu^-)$, improves by 60% for an impact parameter significance cut of 3σ and a p_T cut of 2 GeV/c on all three leptons.

These estimates were made following Ref. [4]. The values used in the SVX II simulations are shown in Figure 9. We have continued this study [4] to the cases of strip pitch, readout strip pitch, and large track angles of interest to SVX II [27].

The software package is based on code written by V. Luth [4] to simulate the response of a 300 μm-thick detector to charged tracks which traverse it at angles of incidence between 0.0 and 1.4 radians from the normal. Strip pitches of 73, 111, and 166 μm, and strip pitches of

73/2, 111/2, and 166/2 μm but with readout pitches of 73, 111, and 166 μm are considered. Results are shown for signal-to-noise ratios of 12 and 18 to 1. In the simulation, tracks are thrown for each angle of incidence under consideration such that a width in the center of the detector of one readout pitch is evenly illuminated.

Each track is propagated through the detector by slicing the detector horizontally into several virtual layers, typically 10 per 100 μm of silicon traversed, and depositing charge in each according to a Landau distribution with an average of 80 e^-/hole pairs per μm. As this charge is drifted through the detector, it responds to effects of diffusion, applied bias voltage, and magnetic fields. The charge is then collected on the strips. Gaussian random noise is added to the strips. To simulate detectors with both readout and non-readout strips, the diffusion pitch is halved, and the charge collected on the strips which are not read out is shared equally by the adjacent readout strips.

Three types of readout are considered: analog, in which all strips above a given threshold are read out and pulse height information is stored; digital, which is similar to analog without the preservation of pulse height; and nearest neighbor logic, which is similar to analog but which in addition requires readout of subthreshold strips neighboring those which pass the threshold cut. The preservation of analog information permits charge division, thereby improving z resolution on oblique tracks in detectors with intermediate (non-readout) strips.

Three clustering algorithms are considered. In analog clustering, channels are compared sequentially with a threshold. A cluster begins with the first channel encountered which exceeds the threshold and ends when a channel is encountered which does not exceed the threshold. Digital clustering uses the analog clustering algorithm with digital readout of the SVX II data. Finally, in predictive clustering we use the knowledge of angle of incidence, α, to predict the number of strips in a cluster. This could be obtained from extrapolation of a VTX track, for example. For our simulations the number of strips in the predictive method is required to be at least 3. Clusters are then identified by maximizing the summed pulse height in a "window" of this width and requiring that the sum of the pulse heights within the window must pass a threshold cut.

The centroids of the tracks in N-channel clusters are calculated according to several weighting schemes [27]. The algorithm that is least sensitive to the track angle, α, is a variant of the weighted mean, that we call central averaging:

$$\langle z \rangle = \frac{z_1 \mathrm{PH}_1 + z_N \mathrm{PH}_N + (\sum_{i=2}^{N-1} z_i) \times \langle \mathrm{PH} \rangle_{\mathrm{inner}}}{\sum_{i=1}^{N} \mathrm{PH}_i},$$

where PH_i is the pulse height on the ith strip and the average pulse height for the central strips:

$$\langle \mathrm{PH} \rangle_{\mathrm{inner}} = \frac{\sum_{j=2}^{N-1} \mathrm{PH}_j}{N-2}.$$

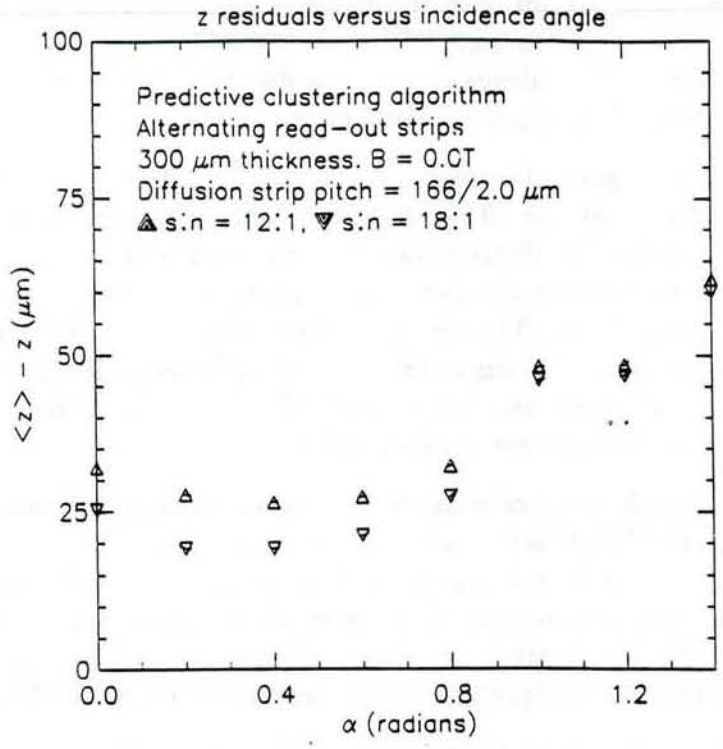

Figure 50: Expected z resolution using the predictive clustering algorithm and central averaging for the proposed SVX II double sided detectors. The scatter reflects the statisticaal error in the study.

The $i = 2$ to $i = N - 1$ terms reduce sensitivity to Landau fluctuations which dominate the resolution at large values of the track angle.

Our studies suggest that the following is one attractive choice for optimizing the detector resolution. Choose a 166/2.0 μm diffusion strip pitch and read out alternate diffusion strips only. (The interleaved strips are biased and capacitively coupled to the readout strips, but are otherwise ignored.) Keep only channels that pass a 25% minimum-ionizing pulse height cut, with the proviso that readout channels adjacent to those passing this cut are kept. Record the pulse height information. Predict the size of a "window" of strips, based upon an estimate of the incidence angle of the track, and position the window where it subtends the maximum pulse height. Calculate the centroid of the window using a pulse height weighted average where the average pulse height is used to weight the inner strips. The resolution obtainable with these parameters is shown in Fig. 50.

This result predicts somewhat increased z resolution from that shown in Fig. 9.

Capacitance

The detector parameters which determine the signal-to-noise ratio of the charge collection are the leakage current and the capacitance to ground of the strips. The work on the prototype amplifiers indicates that in order to achieve a signal-to-noise ratio of 12:1, the capacitance of the strips must be less than 30 pf. We wish to identify the electrical features which are the primary contributors to the capacitance in order both to extrapolate to our final design and to modify the design as necessary to achieve our required signal-to-noise ratio.

The following estimates are based on measurements of existing devices at Santa Cruz [28] and at LEP by the DELPHI group and on calculations by Ikeda *et al.*[29] The result is that, while the p-side capacitance is understood, the n-side capacitance remains difficult to estimate. We will test prototype structures to decide on the final technology.

One of the major uncertainties is the effect of ionizing radiation on the capacitance due to the build-up of fixed charge in the oxide. The calculations of Ikeda *et al.* show that there is a significant increase in the capacitance as the fixed charge at the oxide-silicon interface increases from 10^{10} to 10^{12} holes/cm^2. In unhardened MOS devices, charge densities of 10^{12} holes/cm^2 are typical of doses of 1 megarad, but this number is very dependent upon the type of oxide. Preliminary results from Santa Cruz indicate that this is not a significant problem on the p-side. This is reasonable, since the holes are the primary source of the problem, and they drift away from the interface on the p-side. The holes drift toward the interface on the n-side, however. Until we have experimental data, we will ignore the effect on the p-side but use the calculations of Ikeda *et al.* to include it on the n-side.

The results summarized here are estimates for an n-type bulk with a resistivity of about 5000 ohm-cm, a thickness of 300 μm, and implants which are capacitively coupled to the readout system. As an example consider a Layer 4 ladder. It is read out by six chips on each side and is 17 cm long, 3.84 cm wide and has 768 and 1700 strips on the p- and n-sides respectively. The pitch (p) of the strips is 50 microns on the p-side (ϕ) and 110 microns on the n-side (z).

The capacitance to ground of the p-implant on the cathode side of the detector depends primarily on the ratio of the metal width to the pitch (w/p) when p $\ll$ the thickness (t). C. Levier at UC Santa Cruz [28] has measured a set of Hamamatsu detectors with a 50 μm pitch and a variety of widths. The results have been fit to a straight line

$$C_I(\mathrm{pf/cm}) = 0.6 + 1.7 \cdot (\frac{\mathrm{w}}{\mathrm{p}})$$

Using this model, the capacitance of the p strips of the standard prototype with $w/p = 0.1$ is 0.93 pf/cm or 16 pf for a 17 cm detector.

This number agrees well with the calculations of Ikeda *et al.*,[29] who have calculated values for 5 μm wide strips on a 50 μm pitch using PISCES IIB with and without the intermediate floating strip. Their result is important because it shows how to scale the capacitance for the presence of a floating strip and for a variation in the fixed charge. They find that the change in the capacitance due to a floating strip is not large. In the Santa Cruz

paper it appears to be an increase of about 10% - 20%. It seems likely that this increase is primarily due to the fraction of the gap which has been shorted out by the electrode, i.e., an effective increase in w/p. The change may be greater for wider implants.

We feel that we will be able to exceed our target for signal/noise on the p-side. There is much less experience with n-side devices. Although we can learn from the experience of other groups, we will order prototype devices to make our own measurements. The DELPHI group at LEP is the first group to try the double metal scheme. Although the capacitance of the first prototypes delivered to DELPHI was so high that they were unusable, a substantial R&D project with suppliers has now resulted in usable devices (although the devices have yet to be delivered). Our ladder is larger than theirs, however, and it behooves us to take all steps to minimize the capacitance.

On the n-side, the effective source capacitance of one readout channel is a network with 3 types of elements:

1. Junction capacitance to the p-side, C_J,
2. Interstrip capacitance of the n strips, C_I,
3. 1st metal to 2nd metal overlap capacitance, C_m.

The first two components are similar to the p-side effects. On the n-side the interstrip capacitance depends upon (1) the mechanism used to isolate the n strips, (2) the total length of strip grouped to one readout channel, (3) the ratio of the width of the strip to the pitch, and (4) the fixed charge at the oxide-silicon interface. The latter is important because it tends to enrich the surface with majority carriers and reduce the resistance between strips. It is the major reason that some mechanism must be used to isolate the strips, and it is the reason why a sophisticated program like PISCES IIB must be used to calculate the charge distributions.

The Ikeda *et al.* calculations indicate that the interstrip capacitance is 30% larger for the p-channel isolation than it is for the field effect isolation, and that the p-channel devices are much more sensitive to the fixed charge. On the other hand, Micron Semiconductor has had good performance with p-channel isolation devices produced for OPAL. We are ordering prototypes of both isolation schemes for evaluation.

To obtain a budget for the metal-to-metal overlap capacitance, we first estimate the junction and interstrip components. The junction capacitance per unit area is the same as the junction capacitance on the p-side, and since the same area is being subdivided into the same number of readout channels, it has the same value, $C_J = 0.16 \cdot L(\text{cm})$ pf. This gives 2.72 pf for $L = 17$ cm. Our standard prototype uses field effect isolation for the n-strips. The measurements from the DELPHI prototypes are consistent with a value of 1.1pf/cm for our geometry. The total interstrip capacitance depends on the ratio of number of strips on the n-side to number on the p-side, the length of n strips and the capacitance per unit

length,

$$C_I = \frac{1700}{768} \cdot 3.84\text{cm} \cdot 1.10$$
$$= 9.35\text{pf}$$

This is smaller than the value on the p-side because the pitch is much larger. According to Ikeda *et al.*, we would expect a 30% larger number for p channel isolation. The sum of these numbers, 12pf, leaves a maximum of 18pf for the overlap capacitance. If the 12pf increases to 18pf due to radiation, the overlap capacitance must be less than 12pf to keep the total under 30pf.

The VTT devices tested by DELPHI had overlap regions between the strips of the "first metal" and the strips of the "second metal" of 5 μm by 18 μm separated by 1 μm of silicon dioxide with an ε_o of 4. If we treat the region like a parallel plate capacitor it results in C_m = 3.2 ff. (This can be reduced with thicker insulator and by using an insulation with small dielectric constant.) The total overlap capacitance is :

$$C_M = (N_n + N_p) \cdot C_m = 7.9\text{pf}$$

When DELPHI used this model they found that the estimate was small by a factor of three. No explanation for this factor of three is presently available, so to be conservative we wish to allow for this same effect. While 8 pf is usable, 24 pf will exceed the budget. This number can be reduced by using a thicker oxide.

Clearly the uncertainties are large and must be resolved by measurements. It seems likely that we can achieve an adequate signal/noise on both the n- and p-sides. The most important variable is the thickness of the oxide. We have asked the manufacturers to make devices with 2 microns of silicon oxide and up to 5 microns of polyimide. In the meantime we are measuring devices obtained from DELPHI.

7.3 Prototypes

Vendor Options

Double-sided silicon microstrip detectors are being planned or installed at nearly every major storage ring and collider experiment operating today, including OPAL, ALEPH, DELPHI, L3, and CLEO. As a result, there are at least 3 vendors (Hamamatsu, SI, and Micron) with experience in meeting the technological challenges that these devices pose.

We have made contact with the vendors and have been apprised of their production capabilities. Orders for prototypes will be placed with two of the three. Both vendors will be asked to make a mask which will provide 2 full-length Layer 1 detectors and 2 half-length Layer 2 detectors. The four detectors will have all the n- and p-side combinations of strip

pitch that interest us. Using these we can determine the pitches that are optimal for the production detectors with minimum investment in prototype masks.

Both of the Layer 1 and one of the Layer 2 detectors will have 50 μm pitch on the p-side. The remaining Layer 2 detector will have 25 μm pitch on its p-side, so that operation with intermediate sense strips which are not read out can be studied. Both of the Layer 2 detectors will have 111 μm pitch on their n-sides. Each of the Layer 1 detectors will have a different pitch on its n-side–83 and 166 μm. The other parameters of these prototypes will be as described in the first paragraph of this section.

Evaluation

A test bench has been set up for studies of the properties of these prototypes. The detectors will be mounted on custom-designed boards for operation with readout chips. The test facility includes an SRS/SDA system to operate the chips and digitize the data. The detectors will be exposed to beta-radiation provided by a Sr-90 source. A scintillator will provide the trigger, and there is an option for cutting on the beta energy and varying the impact angle of the radiation. Measurements will be made of the front-back charge correlation, n-side interstrip resistance, signal/noise for the p- and n-sides as a function of track angle, and cluster size and pulse height distributions. Capacitance measurements such as those which are already underway will be carried out as well. Following exposure to a gamma source the detectors will be re-examined for noise increase due to trapped charge in the oxide.

8 Front-End Design

In this section, we describe the current status of design and prototyping efforts for the front-end readout chips for SVX II. The goals for this effort are to produce a suitably radiation-hard chip with low noise and adequate gain bandwidth which can be used with the 132 ns bunch spacings expected in the late part of the decade with the Tevatron.

At present the design of the readout chip for SVX II has reached the prototype stage at both LBL and Fermilab. It is expected that the final chip will be a collaborative effort between the two groups. There is a memorandum of understanding which has been negotiated between the two laboratories and detailed discussions are currently in progress to define the exact activities of the two groups. Physicists from both CDF and D0 are responsible for agreeing on the detailed specifications of the readout chip. Below we summarize the present status of the design work by both groups. We begin with a brief summary of what is known about the expected occupancy in the SVX II detector based on the present SVX experience and from a Monte Carlo study.

8.1 Occupancy Study

We studied the expected occupancy for the proposed SVX II using the ISAJET Monte Carlo and a simple geometrical model. To check that this method would yield reliable results, we first used a similar model for the present SVX and compared the occupancy predicted by the Monte Carlo with that observed in our current data set. A "nearest neighbor" readout method as used for the real data sample was modelled for both the SVX and SVX II Monte Carlo samples. In this method, all hit channels over threshold are read out, along with the nearest physically adjacent channels. For the Monte Carlo samples, channels were considered to have been hit if they contained charge deposition greater than or equal to 0.15 times that expected for a minimum ionizing particle.

For the current SVX, the occupancy was determined by the combination of noise signals and true charged tracks. We refer to the occupancy due to true charged tracks as the "physics" occupancy. In the real data, when we demanded that there be at least one fully reconstructed track in the SVX, we observed a total occupancy of $\sim 6.7\%$. The occupancy observed when there were no tracks reconstructed in the SVX, on the other hand, was $\sim 5.7\%$. One can see that the physics occupancy is of order 1%, and that the total occupancy in the present SVX is dominated by noise signals.

To study Monte Carlo events in a physically interesting sample, we used an ISAJET model of $t\bar{t}$ production. Since the multiplicity of this Monte Carlo sample is approximately 3 times larger than the data sample used above, we expect a physics occupancy for the present SVX about 3 times larger also. In fact we observed in the model an occupancy of 2.6%, which is consistent with this expectation.

For the SVX II design, there are two features which will affect the occupancy. First,

the detector will be about a factor of two longer, which means that it will be sensitive to a larger number of charged tracks per event. This effect would tend to increase the observed occupancy. Second, however, there are 3 barrels rather than the present two, and each barrel will be subdivided electrically into two regions. This increases the number of read out regions to 6, which would tend to lower the occupancy by a greater factor. Using the same ISAJET $t\bar{t}$ Monte Carlo sample, we in fact observed an occupancy of only 1.3% overall with the SVX II geometry.

A breakdown of the expected occupancies for SVX II as determined from this study is shown in Table 20. Significant variations exist across the barrels, and across the layers of each barrel. As expected, the greatest occupancy will be for the center barrel at its innermost layer. Since the readout takes place on a wedge-by-wedge basis according to the present plan, layer-dependent variations will be less important to the front-end and DAQ system design than the overall numbers shown in the first column of the table. These estimates are for occupancy in the ϕ readout. For the z readout the physics occupancy will be higher due to the larger cluster size for angled tracks.

Table 20: Simulated SVX II occupancy broken down by barrel and layer.

Barrel	Overall Occupancy	Layer 0	Layer 1	Layer 2	Layer 3
± 1	2.0%	3.7%	2.5%	1.9%	1.2%
± 2	1.2%	2.2%	1.5%	1.1%	0.7%
± 3	0.8%	1.5%	1.0%	0.7%	0.5%

8.2 LBL Chip Design

The LBL design for the SVX II readout chip will be fabricated in the UTMC radiation hardened 1.2 micron process. The principal features of the SVX II chip compared with the original SVX chip are as follows:

- Faster analog signal path - settling within 130 ns for the upgraded Tevatron.
- Continuous time analog signal path (no reset cycle necessary).
- Double sample capability (AC coupled detectors presumed).
- An analog pipeline of programmable depth (16 deep for up to 2 us of delay @ 130 ns).
- Only a single clock during acquisition (CMOS or balanced positive ECL).
- On-chip analog to digital conversion.
- Digitally programmable threshold for sparse readout.

- Complete digitization and readout option (no sparse).
- Faster all-digital sparse readout (>20 MHz).

For the LBL design prototype chips containing all of the critical function blocks of the SVX II chip have been designed and tested or are presently in fabrication (HP 1.2 micron). These include:

- A preamp prototype chip containing several variations, all with continuous time reset.
- A 16 deep analog pipeline prototype chip with double sample readout capability.
- A complete parallel analog to digital conversion sub-block prototype chip.
- A super-fast sparsifying readout prototype chip using a novel asynchronous method.

The preamp prototype chip has returned from fabrication. A summary of early test results is given in Table 21 below.

Table 21: Test results for a preliminary version of the LBL SVX II chip.

Source Cap.	Feedback	10-90% Rise	Gain	Noise
33pF	100fF	72 ns	11.5 mV/fC	2700 e
33pF	30fF	138 ns	35 mV/fC	1600 e
10pF	30fF	77 ns	31 mV/fC	1000 e

These measurements were taken at a supply voltage of 5 V, and a power consumption per channel of 1 mW. The figure for input noise is an approximation for a double sample with a period of 132 ns. More detailed measurements are in progress.

8.3 Fermilab Chip Design

The study of an advanced readout chip (ARC) for silicon strip detectors has also been continuing for some time at Fermilab. The work has included design and fabrication of numerous test chips containing subcircuits for a complete 128 channel readout device. The device being developed is designed to match the Fermilab colliding beam characteristics with beam crossing intervals between and 132 ns and 400 ns. The main features of the ARC are as follows:

- Operation at a high interaction rate.
- Low noise, power, and mass.

- Operation with double sided detectors.
- Pipelined storage for a level 1 trigger.
- On board, highly parallel and rapid digitization.
- Data sparsification.

The front-end design being pursued at Fermilab uses a high speed switched capacitor integrator and amplifier which is resettable within the constraints of the beam structure. A switched capacitor approach was used instead of a real time front-end to avoid problems associated with the tail of the signal pulse from earlier interactions affecting subsequent buckets. The design has an analog storage cell pipeline for each channel to provide the necessary buffer for the CDF level 1 trigger. After a level 1 trigger there is a separate low power ADC for each channel. This approach permits the use of a digitally set common threshold for data sparsification.

The chip does not overlap data acquisition and readout cycles, thereby avoiding digitization noise during data acquisition. Resetting the front end amplifier is done only during the long interval between super groups, not after each beam crossing, The design is being developed in two parts: (1) the integrator and amplifier design, and (2) the analog storage, ADC and data sparsification.

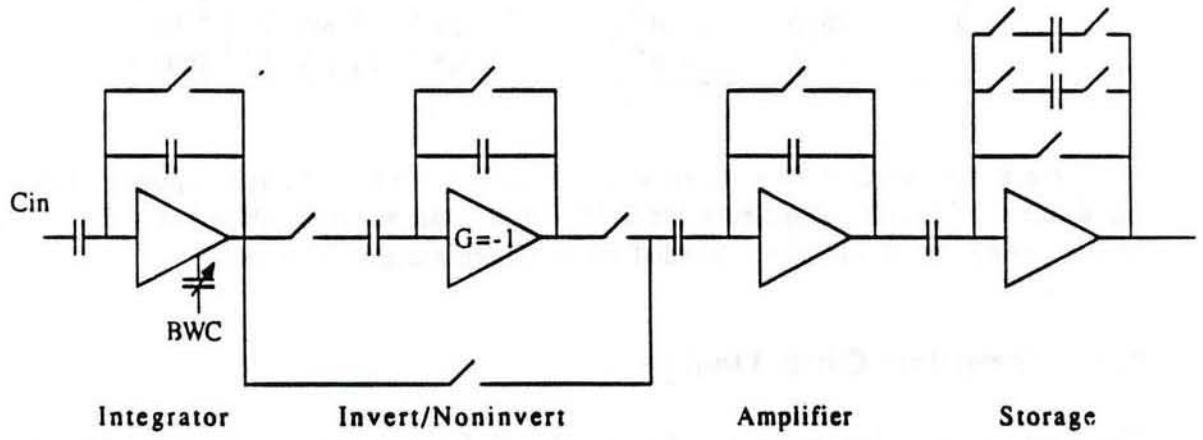

High Speed Switched Capacitor Front End block Diagram

Figure 51: Schematic of the SVX II front-end analog section.

A schematic of the most recent version of the front end integrator, amplifier and storage system is shown in Fig. 51. The integrator has a programmable gain bandwidth so that the signal to noise and risetime can be tuned to the beam crossing interval of either 132, 200

or 400 ns. This feature can also be used to tune individual chips to compensate for process variations in response time. The integrator is followed by an inverter so that the chip can be used with a bidirectional input. This is necessary for double sided detectors, since the signals from the two sides have opposite polarities. This prototype version had only a few storage cells.

The production version will require at least 16 cells, and preferably 24. The front-end power is approximately one milliwatt/channel. Because the integrator will only be reset during the intervals between super groups, the front-end integrator has a large dynamic range of ±400 fC. However, the amplifier preceeding the storage section is reset between every beam crossing, so that an appropriate double-correlated sample reflecting only the charge integrated for the desired beam crossing is stored in the successive analog storage cells.

Risetime measured at storage output for
different switch combinations (BW settings)
with: Cin = 10pf Qin = 10 fc.

	BW setting					
Trace	S1	S2	S3	S4	0-99%	10-90%
Top	0	0	1	0	108 ns	56ns
Center	1	0	0	1	182 ns	86ns
Lower	1	1	1	1	270 ns	128ns

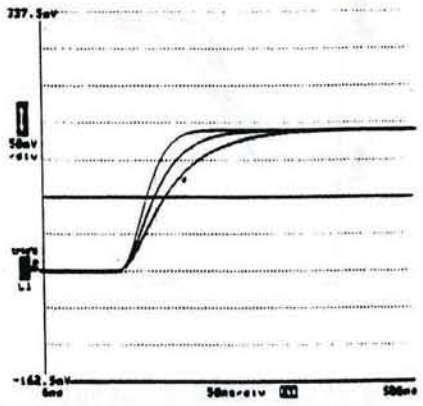

Figure 52: Risetime measured at the storage output for different integrator bandwidth settings with C_{in} =10 pf and Q_{in} =10 fC.

The risetime responses of the chip for input capacitances of 10 and 30 pf are shown in Figs. 52 and 53, respectively. Integrator/amplifier performance measurements for the various risetime and input capacitance settings are shown in Tables 22 and 23. All of these results are based on tested implementations in a 2 micron CMOS process through MOSIS.

Both prototype analog storage chips and ADC's have been produced and tested. They have now been combined into a single test prototype consisting of 8 parallel channels of analog pipeline four cells deep followed by an offset compensated comparator and ADC. A

Risetime measured at storage output for different switch combinations (BW settings). with: Cin = 30pf Qin = 10 fc.

Trace	BW setting S1	S2	S3	S4	0-99%	10-90%
Top	0	0	0	0	115 ns	61ns
Center	0	1	0	0	184 ns	88ns
Lower	0	1	1	0	294 ns	137ns

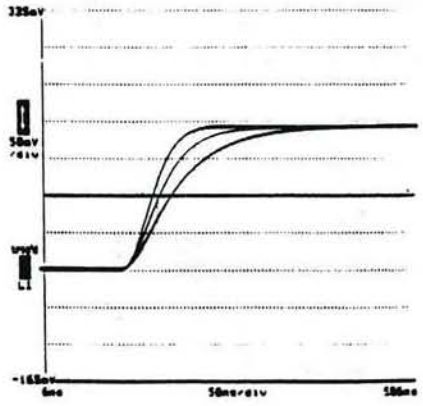

Figure 53: Risetime measured at the storage output for different integrator bandwidth settings with C_{in} =30 pf and Q_{in} =10 fC.

Table 22: Integrator plus amplifier performance for an input capacitance of 10 pf.

Integrator + Amplifier Performance

Cin	T sample	Pol	10-90%	Gain	Pattern	Noise
10p	400ns	+	129ns	19.0mv/fc	DCS	960e
10	200	+	86	18.8	DCS	1080e
10	150	+	56	18.9	DCS	1210e
10	400	-	132	18.3	DCS	1030
10	200	-	93	18.1	DCS	1130
10	150	-	64	18.3	DCS	1220
10	150	-	64	18.3	MDCS	1530

Table 23: Integrator plus amplifier performance for an input capacitance of 30 pf.

Integrator + Amplifier Performance

Cin	T sample	Pol	10-90%	Gain	Pattern	Noise
30p	400ns	+	137ns	19.1mv/fc	DCS	1720e
30	200	+	88	19.1	DCS	2050e
30	150	+	61	19.2	DCS	2220e
30	400	-	146	18.4	DCS	1730
30	200	-	95	18.3	DCS	1950
30	150	-	69	18.3	DCS	2180
30	150	-	69	18.3	MDCS	2330

Power (Integrator + Inverter + Amplifier)	1.17mw/ch
Integrator range	+ or - 300 fc
Linear output range	30 fc*

* Has been improved.

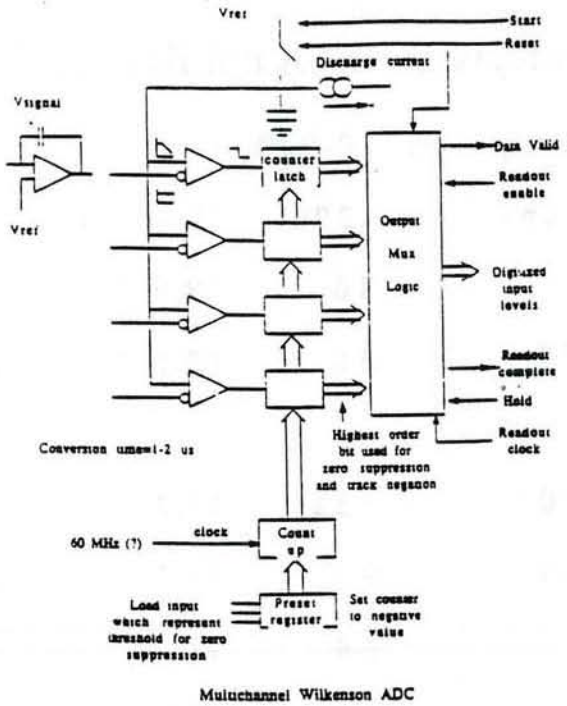

Figure 54: Schematic of the multichannel Wilkenson ADC to be used in the SVX II chip.

schematic of the ADC is shown in Fig. 54. The multi-channel ADC allows for the simultaneous digitization of many channels. A digitally applied threshold voltage is used for data sparsification. We plan for a 7-bit ADC with a digitization speed of $\leq 1.5\mu s$.

The initial test results on the analog storage/ADC performance are very encouraging. Variations in offset and gain for every cell of every channel on an eight channel device were checked. Maximum offset variation between cells on any given channel is less than 1.5 mV or 0.15 of the least significant bit (LSB). Maximum offset variation between any cells on two different channels is 4.0 mV or 0.4 LSB. Since the variation in offsets between all 24 cells is 4 mV or less, it is estimated that 4 mV is equal to $\pm 2\sigma$, which means that the RMS offset variation is about 1 mV or 0.1 LSB. The maximum gain difference between cells on a given channel was found to be 0.4 % or 0.4 LSB. The maximum gain difference between channels was found to be 0.5 % or 0.5 LSB. The cell and channel gain differences suggests that capacitors of the chip are matched to better than 0.5 %. The maximum gain variation between cells on two different channels is 0.8 % or 0.8 LSB.

The linearity of the combined analog storage and ADC was also very good. The maximum error over the seven bit range was found to be $\pm$ 3 mV or $\pm$ 0.3 LSB. It is interesting to note that placing the ADC converter on the chip with the integrator circuit should reduce the inherent gain variation due to integrator capacitor variations caused by process variations. Normally gain variations between runs of 20 % can be expected. Because of the capacitor matching measurements previously presented, effective gain variations could be reduced to

about 0.5 %.

9 Radiation Damage

The luminosity of the Main Injector presents serious requirements for the radiation hardness of the detectors, the electronics, and the materials used in the design. All components and materials in the final design will be tested for radiation damage at doses above those expected.

The design luminosity for the Main Injector is 5 to 6 $\times$ 10^{31} $cm^{-2} \cdot s^{-1}$ giving 600 pb^{-1} for a data run of 10^7 seconds at full luminosity. Our plan is to design for a total integrated luminosity of 2 fb^{-1}. Based on studies and experience with SVX we estimate that this corresponds to a dose of 1.0 Mrad at the inner radius of the detector, and 0.2 Mrad at the outer radius. This agrees to within a factor of two with the estimates of Ellison [30] of 0.25 Krad/pb^{-1} at 2cm from the beam. These doses correspond to a particle flux of 4 $\times$ 10^{13} particles/cm^2/fb^{-1}.

The components at greatest risk are the electronics and the silicon strip detectors.

Electronics

The front-end data acquisition ASIC must be manufactured in a radiation hard process. We plan to use the same UTMC foundry used to manufacture the SVXH chip. The major problems generated by radiation damage in MOS circuitry are due to threshold shifts and increased noise in the analog signals. The SVXH chip was tested at Berkeley up to 2 Mrads with a Co60 source. The threshold shifts were less than 0.1 volts and the noise increased by less than 20%. These measurements are in agreement with those on a previous version and we feel confident that the new electronics will be hard enough to last through a 2 fb^{-1} exposure.

Silicon Strip Detectors

Detectors suffer damage from both ionizing radiation and nuclear reactions. The ionizing radiation generates charge and traps in the surface in much the same way that it does in MOS circuitry. This affects the surface leakage currents and increases the capacitance between the strips. Studies by a Hammamatsu-Nagoya collaboration [31] and by U.C.Santa Cruz [32] with Hammamatsu detectors show that the effect of ionizing radiation on the p-side can be reduced by minimizing the ratio of strip width to strip pitch (w/p). They find a 30% increase in the capacitance after a dose of 500Krad for w/p=0.4 but the increase extrapolates to zero at w/p=0.2. On the other hand measurements by Masciocchi *et. al.* [33] on an unbiased detector which was a prototype in the RD20 program for LHC show a uniform increase of about 30% after 1MRad. These disagreements indicate that we must carefully evaluate the products of each vendor.

There is less information about the n-side and the effects of radiation depend upon the type of isolation used. U.C.Santa Cruz has measured devices with p-implant isolation [32] and find that both the capacitance and the change of capacitance with a dose of 2MRad is minimized by using wide implants. Their best result was with a 24 micron p-implant and a 50 micron pitch which showed no measurable increase in the capacitance after a dose of 2MRad. However the capacitance was 1.6 pf/cm, substantially larger than that on the p-side. There is no published data for double sided devices using field effect isolation on the ohmic side but calculations by Ikeda [29] indicate that, if the oxide is 'rad-soft', the interstrip capacitance may increase by 50% at doses of about 1 Mrad. This would have a significant effect on the signal to noise ratio and needs to be verified experimentally.

Nuclear interactions are a potentially more serious problem: They cause both increased leakage current and, eventually, type inversion. There have been many studies of the increase of leakage current as a function of neutron dose but it is difficult to know how to translate these numbers to the collider enviroment. The increase in leakage current has been measured by CDF to be 0.14 na/Krad/cm for doses up to 15Krad and, again, this agrees to within a factor of two with the estimates of Ellison [30] based on the damage coefficients measured at Los Almos [32]. Since the CDF measurement was made on the beam pipe of the Tevatron collider, it has the right mixture of particles. If this effect is linear, it implies the leakage currents will increase to 2.4 microamperes at a dose of 1 Mrad. Assuming an integration time of 132ns, the shot noise will be $\sim$ 1,100 electrons. This will begin to compete with the Nyquist noise associated with the detector but should be tolerable.

10 Data Acquisition System

The SVX II DAQ is designed to be compatible with the upgraded CDF trigger and DAQ planned for Run II [34], and to be capable of working with eventual higher-speed upgrades which could be proposed. For Run II, the trigger system is intended to handle up to 5kHz of level 1 accepts into the level 2 trigger. Since the SVX II is designed to digitize and readout in response to a level 1 accept in ≤ 5 μs, it is compatible with this requirement. The high speed of the SVX II readout is also required for compatibility with a level 2 displaced-track trigger processor (SVT) discussed in the next section.

Two options are under study for the data acquisition system for the SVX II Stage 1 detector. Both options make extensive use of fiber optics to reduce electromagnetic interference and to speed the readout of the data for use by the level 2 trigger processor. The intention is to develop a DAQ including the front-end chip which is common as far as possible to both CDF and D0.

The first option, which we call the "direct fiber" option, is designed to replace as much as possible of the present SVX port-card system. The digitized sparse data from each 128 channel front-end chip would be read out serially on a single dedicated optical fiber connected directly to a low power LED driver. These drivers would be located either on the detector ladder hybrids immediately adjacent to the front-end ICs, or at the periphery of the detector bulkheads. The system would be highly parallel in that a separate data return optic driver and fiber would be provided for each front end IC. Fourteen bits of information would be transferred serially over each data return fiber: 7 bits for the channel address and 7 bits for the ADC. The bits in this design are clocked off the chip at a rate of 53 MHz using the accelerator clock. Trigger and control signals would be transferred over a single fiber connected to clusters of chips (4-10) also located at either the ladder hybrids or at the periphery of the detector bulkheads. The trigger and control signals as well as the data return fibers are self clocking using a technique known as pulse width modulation (see below).

The second option, called the "HDI-portcard" option, follows the portcard system of the present SVX but replaces the cables from the portcard to the trigger room with parallel high-speed optical links. Each portcard would control all 28 front-end ICs in a single wedge, so there would be a total of 72 port cards in the system. A high-density copper interconnect (HDI) between the portcard and the local cluster of ICs would permit the local cluster to return data at a rate of 7 bits of channel address and 7 bits of data every 18 ns, for a total 53 MHz rate. The sparse data from each chip in the cluster would be presented to the interconnect bus sequentially. At the portcard, the 14 parallel bits of address and data would be sent over a set of 8 low power optical fibers at a 106 MHz rate to the trigger room. In the other direction, trigger, clock, and control information would be sent to each portcard using two fibers, one for trigger and control and one for clock. The port-card would decode this serial information and send it on to the front-end ICs over the hybrid interconnect.

The principal differences between these two options are in the interface with the front end ICs. The rest of the DAQ system is largely common to both approaches. Below we

discuss the two different front end interfaces separately.

10.1 Direct Fiber Option

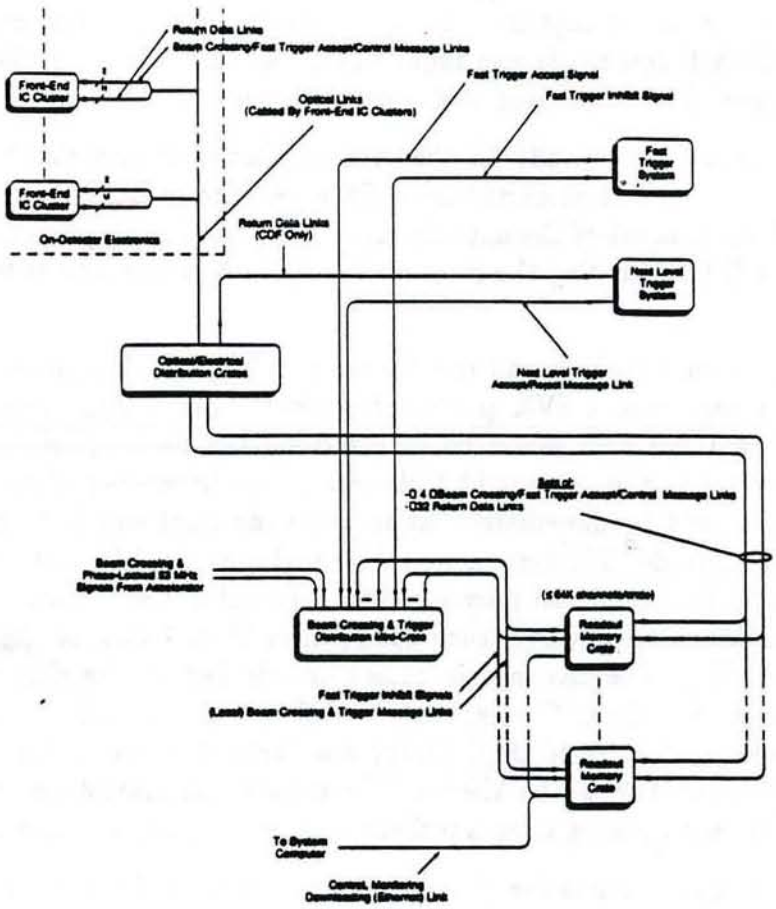

CDF & DO Silicon Strip Upgrade
IC Cluster, Serial Readout Implementation
System Block Diagram
Version 3.0

Figure 55: Single front-end low-power optics readout implementation.

The system block diagram for the implementation of this option is shown in Fig. 55. Major blocks in this figure will be briefly described below.

Front-End IC Clusters

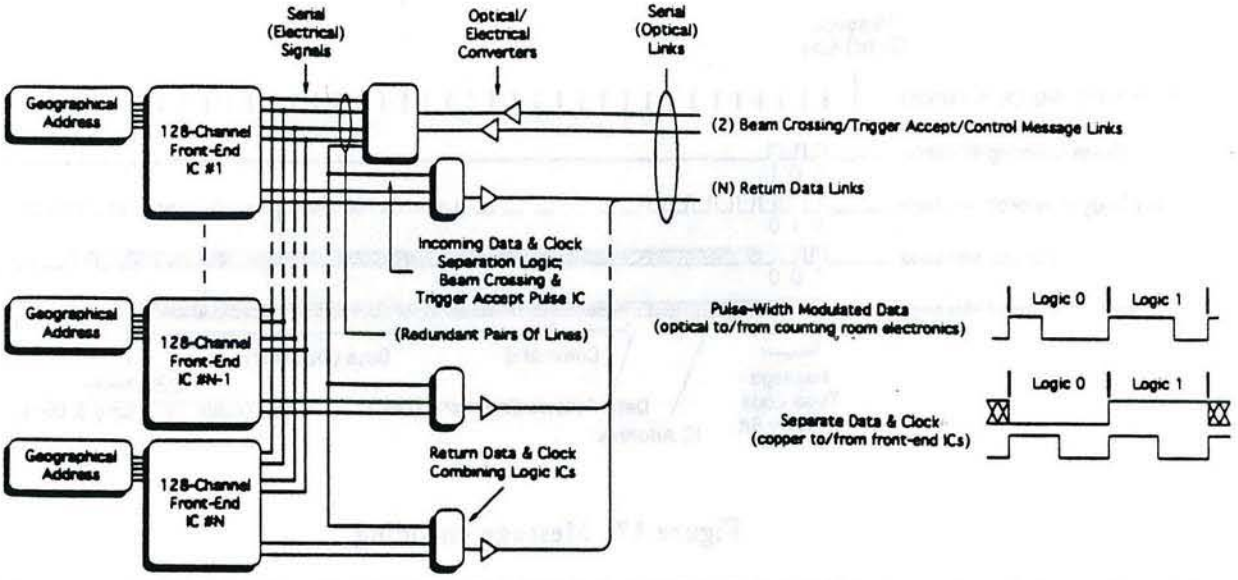

Figure 56: Low-power optics interface to IC cluster with N ICs.

Front-end IC clusters are logical groups of 128-channel silicon strip ICs, optical to electrical and electrical to optical converters, and minimal other logic needed to control, monitor, download the ICs as well as read data from the ICs. For each of the 72 wedges there are a total of 15 ϕ-data 128-channel ICs and 13 z-data ICs. This topology leads to either two, four or eight clusters per wedge. For example, in the four cluster per wedge configuration corresponding to one cluster per layer, the first (outer) cluster has 6 ϕ and 4 z ICs, the second cluster has 4 ϕ and 4 z ICs, the third cluster has 3 ϕ and 3 z ICs, and the fourth (inner) cluster has 2 ϕ and 2 z ICs.

The first or top IC cluster and the second or lower IC cluster shown in Fig. 55 contain N and M 128-channel ICs respectively. The pair of fast trigger accept/control lines entering each IC cluster are each used both to send fast trigger accept signals from level 1 and to download data and control information to the ICs. One of these lines is used for redundancy, in case of component failure in the first line. The N–IC cluster has N return data lines, one per 128-channel IC and the M–IC cluster has M return data lines, again one per IC. A schematic of the optical links to an N-channel cluster is shown in Fig. 56.

Figure 57 illustrates one method for encoding the various messages including beam crossings and performing simultaneous resets to all 128-channel front-end ICs within a cluster. Front-end ICs are responsible for decoding beam crossing messages, fast trigger accept messages and command messages. Although 16 bits of data are shown, data can vary in size with each command. The front-end IC must also decode one or two broadcast addresses as

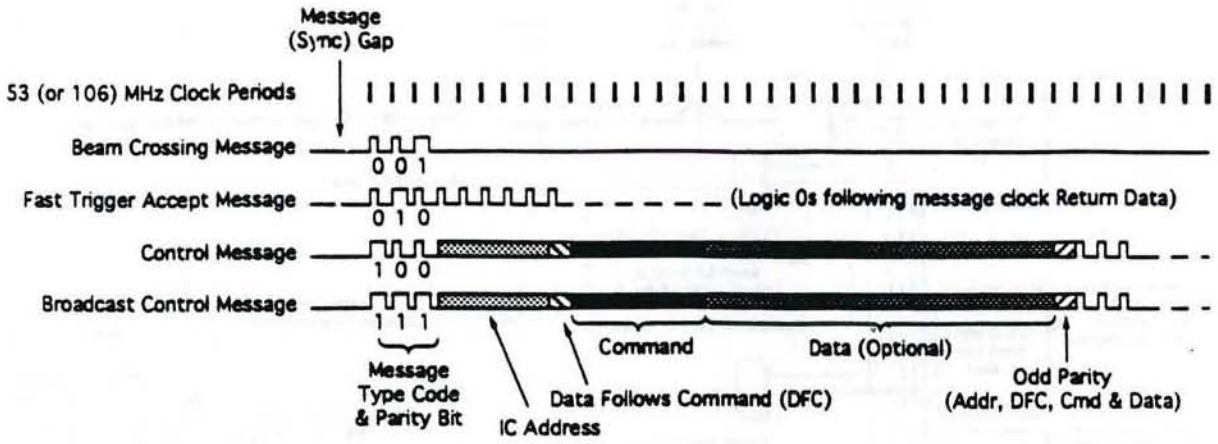

Figure 57: Message encoding

well as its own address.

In the data-taking (analog acquisition) mode, signals are present on the the fast trigger accept/control links when beam crossing messages are received. Signals are also present during the time between the receipt of fast trigger accept messages and a time shortly after the level 2 accept/reject message. These signals are always transmitted during the time that the front-end circuits are in the non-data-taking mode. This eliminates digital noise from incoming signals in the analog portions of the front-end chips.

Optical/Electrical Distribution Chassis

The optical/electrical distribution chassis serve the purpose of providing an easily-maintained, modular location to house the optical links which connect the front-end ICs to counting-house electronics. All conversions of links from differential copper to optical and optical to differential copper are performed in these chassis. Fast trigger accept/control signals to the front-end IC clusters are duplicated as necessary in these chassis. In the CDF system, these chassis also fan out return data links to the SVT and other portions of the level 2 trigger system.

Fast Trigger System (Level 1)

The silicon strip readout electronics interface to the level 1 trigger by accepting (and if necessary inhibiting) fast trigger accept messages. Fast trigger accept messages are fanned

out to readout memory crates via the Beam crossing & Trigger distribution crate. When any readout memory module is nearly full, it asserts a local fast trigger inhibit signal, which is passed through the system. Care must be taken to insure that the readout memory module asserting its local fast trigger inhibit signal has enough memory to continue taking data until triggers are actually inhibited, and that no further data are being transmitted to the module.

Level 2

A similar control system is used in level 2. Messages are used to either read out event data stored in readout memory modules (accepts) or to clear out event data memory from rejected events (rejects). In the CDF system, ϕ data are transmitted to the level 2 trigger system.

Readout Memory Crates

The readout memory crates house modules which are used to hold event fragment data from the 128-channel silicon-strip detector ICs. These modules are also used to transmit fast trigger accept and control messages. In addition to the readout memory modules, these crates each house a module used to accept or inhibit fast trigger signals from the level 1 system. The readout memory crates also contain a VME-bus CPU module used to interface the crates with the rest of the data acquisition system.

10.2 High-Density Interconnect Portcard Option

This is the second option which is being investigated for the SVX II DAQ. Since it has many features in common with the system described above, we only describe the features which are different. Figure 58 shows the block diagram for this option.

Interface To 128-Channel Front-End ICs

Figure 59 illustrates the interface between the port card and front-end 128-channel IC cluster. This interface is divided into two physical media: the port card readout bus, and the High Density Interconnect (HDI) bus. The HDI has yet to be designed in detail.

The bus interface between the ICs and the port card implements the following signals: bidirectional data bus, read/write signal, protocol handshake signals, beam crossing clock, digital readout clock, fast trigger signal, etc. The ICs handled by a port card are divided in clusters as determined by the silicon planes. It is anticipated that buffering will be required to isolate the capacitive loading provided by a cluster of ICs (assuming that the driving capacitive of the front-end ICs is limited).

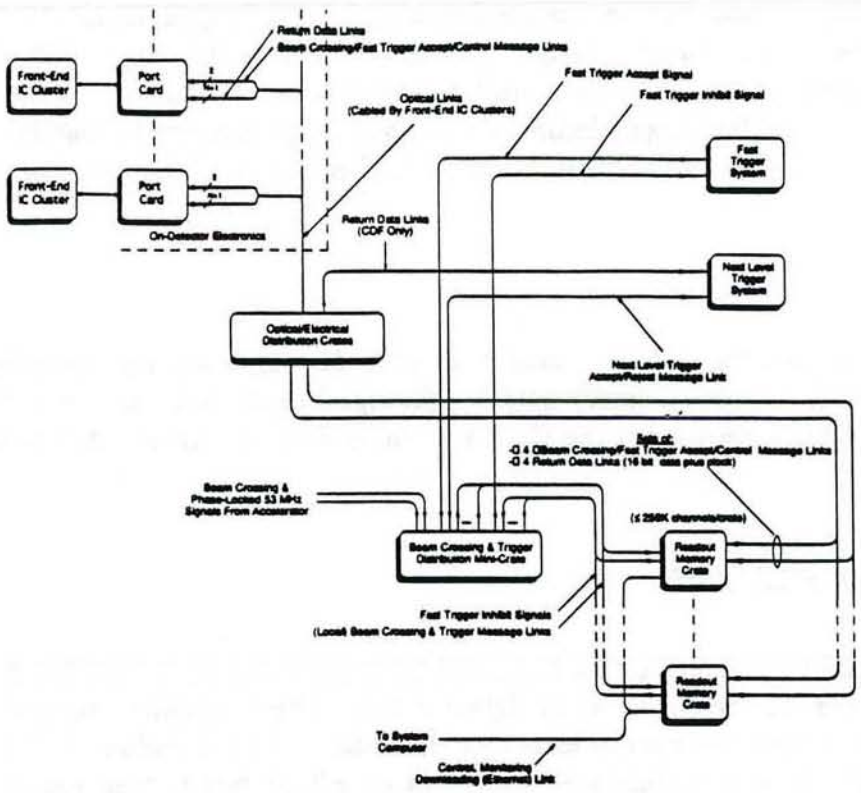

CDF & DO Silicon Strip Upgrade
IC Cluster, Port Card Readout Implementation
System Block Diagram
September 25, 1992

Figure 58: CDF Upgrade Port Card Implementation

There are two scenarios that need to be addressed. In the first case, buffering is performed at the hybrid and a single readout port card bus (cable) is used. This scheme requires the implementation of separate buffer enable signals, or that decoding be implemented at the hybrid. The second case moves the buffers to the port card, but multiple cables have to be implemented. For this description we will use the second option with two cables.

High-Density Interconnect Readout Bus

The HDI holds a number of front-end ICs which are wire bonded to the silicon strips and to the HDI bus and connected to the port card readout bus. The signals mentioned in the previous section are implemented on the HDI. In addition the HDI provides power, ground and geographical addressing for the front-end ICs. The number of geographical addresses

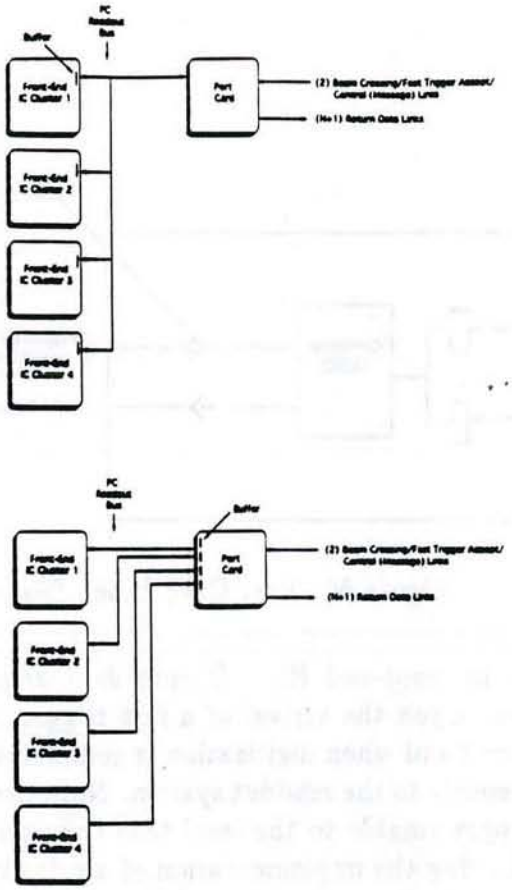

Figure 59: Port Card and Front-End IC Interface

will depend on the clustering and buffering implemented, for the system considered it will be between 3 and 4 lines.

Port Card

The port card is a centralized controller that handles a cluster of front-end ICs under the command of the readout system. This device implements two bidirectional ports, one to communicate with the readout system and the other to communicate with the front-end ICs. Note that the port card provides the protocol conversion between the readout system and the front-end ICs. The port card uses the fast trigger/control link to receive control, fast trigger and beam crossing messages. The control messages are intended for initialization of the front-end ICs. The beam crossing messages are used to generate the accelerator beam crossing signal given the 53 MHz accelerator clock.

During the initialization phase the port card receives commands from the system to

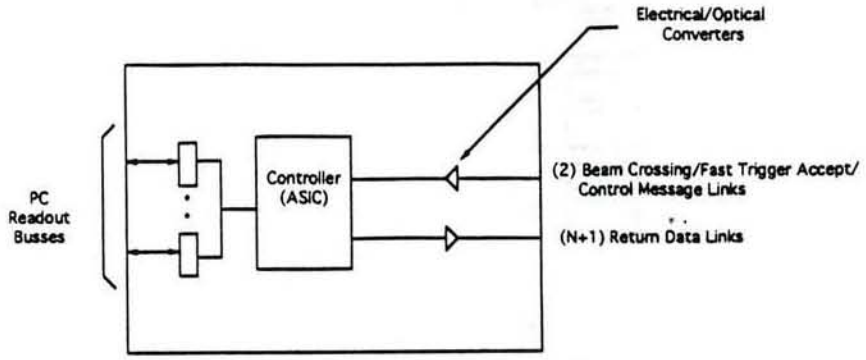

Figure 60: Port Card Block Diagram

control and download the front-end ICs. During data acquisition it receives trigger and beam crossing messages. Upon the arrival of a fast trigger message the controller requests the digitization of an event and when digitization is completed it reads out the digitized data and transmits simultaneously to the readout system. Note that for CDF the controller on the port card should be programmable to the level that the user can specify the readout order of the front-end ICs, allowing the implementation of a priority scheme. The implementation presented here assumes that the return data link is made of eight 106 Mbit/sec links (i.e. 106 Mbytes/sec). Figure 60 shows a block diagram of the port card.

Port Card Communication Ports

The port card implements two unidirectional communication ports to form a duplex communication scheme with the readout memory module. Both of the ports are synchronous to the 53 MHz system clock. The first port is the incoming data which is implemented in one serial data line. Messages received by the port card are encoded serially on this line using the protocol shown in Fig. 57.

The outgoing data port is one byte wide to support the readout rates imposed by the Next Level Trigger System. For this application the digitized data and channel ID uses 14 bits. Then the channel information is transmitted in two consecutive transfers with the two upper bits used to specify the data being transmitted.

11 Triggers

11.1 B Triggers

The inclusive b cross section at the Tevatron collider is $\sim 60\mu$b resulting in the production of $\sim 6 \times 10^{10}$ B's in a 1 fb^{-1} run. Although this cross section is large, an important goal of the Tevatron physics program is to search for B physics processes that represent only a tiny fraction of the total B yield. Triggering must select B candidates from the $\sim$ 1000 times larger total inelastic trigger cross section for CDF, while maintaining a high efficiency for the most interesting B events. CDF B triggers will typically require combinations of high p_T leptons and in some cases evidence for a separated vertex in the event. The trigger thresholds discussed here are somewhat speculative, but appropriate in light of the rate of improvement in DAQ and trigger technology.

At this time the exact capabilities and details of these upgrades, especially for muons, remain to be defined. At the trigger level the p_T threshold limitation is set by the desire to limit the Level 1 + Level 2 deadtime to $\leq 5\%$. In the absence of Level 1/Level 2 pipelines, a Level 2 decision time of 10 μsec limits the Level 1 accept rate to $\leq$ 5 KHz. Even with this restriction, trigger studies indicate that it should be possible for CDF to run a Level 1 dimuon trigger with $p_T(\mu)$ thresholds of $\sim$ 2 GeV and Level 1 dielectron trigger with $p_T(e)$ thresholds of $\sim$ 3 GeV at luminosities of 5×10^{31} cm^{-2}sec^{-1}. Level 1 single lepton trigger thresholds should be possible with $p_T(e/\mu)$ of $\sim$ 7 GeV, and with the inclusion of Level 1/Level 2 pipelines Level 1 single lepton thresholds could possibly be reduced to $p_T(e/\mu)$ of $\sim$ 4 GeV.

The CDF trigger options will provide efficient triggers for a large number of important B physics studies including rare B decays (for example $B \to l^+l^-$ and $B \to l^+l^-s$), production of B_c (studied through decays including: $B_c \to J/\psi\pi^+$, $B_c \to J/\psi l^+\nu$, $B_c \to J/\psi D_s$ [with $J/\psi \to l^+l^-$]), as well as all studies requiring a B tag (for example $b\bar{b} \to (B \to l\nu X)(B_s)$ and $b\bar{b} \to (B \to l\nu X)(B_d \to J/\psi K_s)$). The 2 GeV dimuon trigger has an efficiency of 15-20% for $B \to J/\psi$ decays, and future secondary vertex triggers for 2-body B decays (for example $B^0 \to \pi^+\pi^-$) are estimated to have an efficiency of $\sim$ 6%. The single lepton trigger, with $p_T \geq 4$ GeV, is estimated to have a B efficiency of $\sim 0.5\%$; this includes the 0.22 branching fraction of $b \to e/\mu$. With these efficiencies, CDF will obtain substantial B physics data samples from a 1 fb^{-1} run. As an example, the number of triggered and reconstructed events expected for the production of B_c in the channel $B_c \to J/\psi(\to \mu^+\mu^-)\pi^+$ is $\sim$ 500 assuming B_c production is $\sim 10^{-3}$ of the b cross section, and the $B_c \to J/\psi(\to \mu^+\mu^-)\pi^+$ branching fraction of $\sim 10^{-4}$.

For non-J/ψ modes, triggers based on secondary vertices will be increasingly important. The capability of using impact parameter information obtained from the vertex detector at the trigger level will be of fundamental importance for any experimental program centered on b physics in a hadron collider environment. Some of the decay channels that are interesting for the study of CP violation will be virtually undetectable at the Tevatron without an

impact parameter trigger (e.g. $B \rightarrow \pi\pi$). Other interesting decay modes (e.g. $B \rightarrow \psi K_s$) can be selected by the requirement of one or two leptons in the final state but will also benefit from an impact parameter trigger in terms of a better rejection factor against background and higher statistics on tape.

11.2 Secondary Vertex Trigger

The Silicon Vertex Tracker (SVT) is a secondary vertex trigger processor based on associative memories under development by the Pisa group in CDF. [1] It is designed to reconstruct tracks in the Silicon Vertex Detector (SVX) and Central Tracking Chamber (CTC) with enough speed and accuracy to be used at trigger level 2 to select events containing secondary vertices from b decay. Simulations have shown that the proposed tracker is effective and the performance is adequate for operating with CDF at luminosities up to 5×10^{31}. Prototypes of critical hardware components have been successfully tested and we are now ready to begin construction of a system that will be operational during Collider Run II.

The typical use of SVT will be in coincidence with some other L2 trigger. For example we would ask for a single muon above some Pt threshold and an impact parameter d significantly different from zero. The impact parameter cut will improve the rejection factor against background and will therefore allow us to lower the Pt threshold and improve the efficiency while keeping the L2 rate at an acceptable level.

To estimate the trigger efficiency for the process $b \rightarrow \mu + X$ we used an ISAJET event sample where b quarks were generated with no p_T threshold (fully inclusive sample). The muon trigger rates as a function of p_T threshold were obtained from CDF note 1467. The probability of getting a fake impact parameter was obtained from a simulation of the SVT algorithm applied to an event sample generated by ISAJET and assuming a 5% occupancy in the SVX generated by noise. The results are summarized in Table 24 for an 80 nb cross section. Comparing the b signal cross sections for an impact parameter cut at the trigger level to that for an offline cut, we see that the SVT provides a gain of an order of magnitude.

The primary challenges for an impact parameter trigger are fast pattern recognition in high multiplicity events and high accuracy track fitting. The strategy we choose to follow to tackle this problem is based on the combined use of the Associative Memory (AM) technique together with a farm of Digital Signal Processors (DSPs) [35].

The overall architecture of SVT is shown in Figure 61. Digitization is performed in parallel for all channels (front-end chips include one ADC per strip. Sparsified digital data are sent to Hit Finders over 72 parallel lines (24 lines per barrel). The task of Hit Finders is to find pulse height clusters and compute the coordinate of the centroid of each cluster. Hit coordinates from Hit Finders and tracks from the CTC track finder, are fed both into the Associative Memory and Event Buffer. The task of the Associative Memory is to perform the first stage of the pattern recognition process: it reconstructs tracks with a limited spatial resolution, using 250 μm bins in SVX layers. These coarse resolution track candidates are

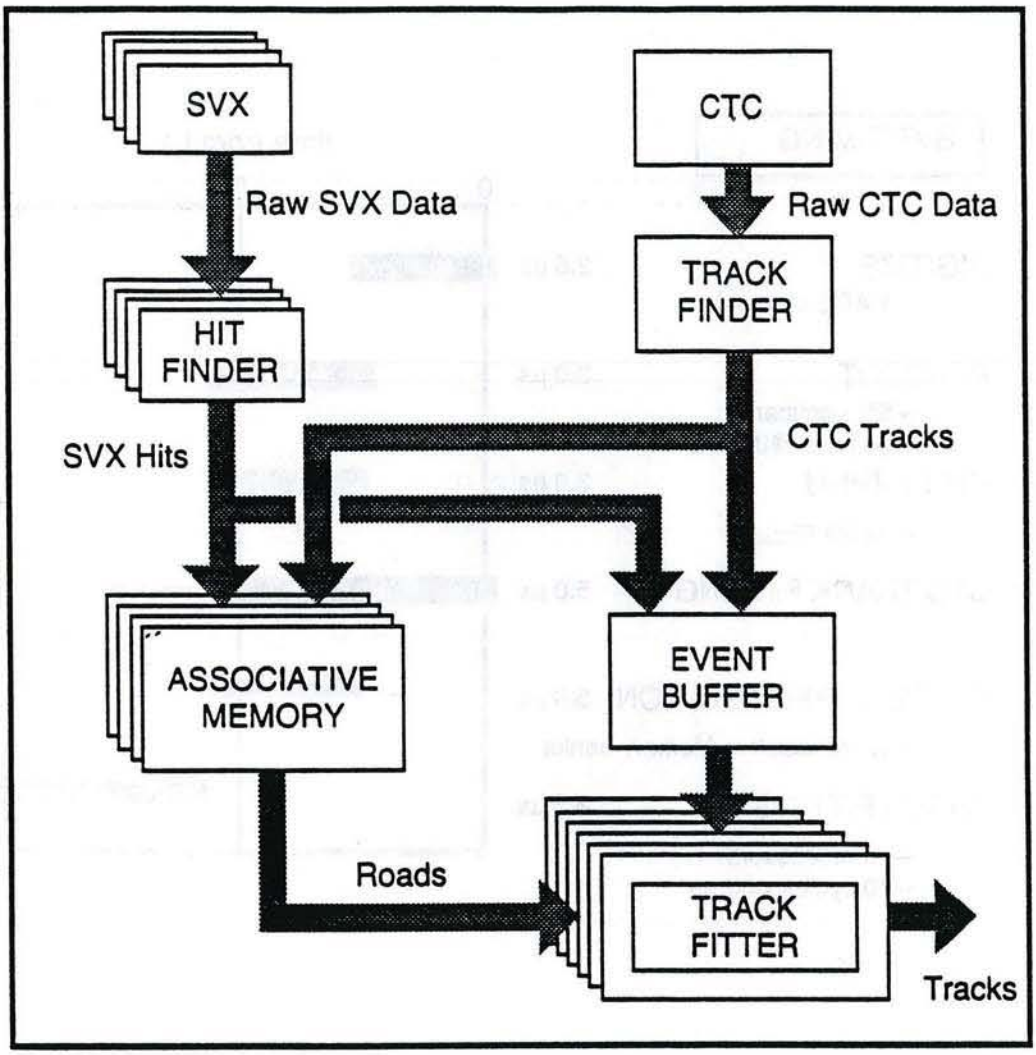

Figure 61: Conceptual design of the silicon vertex tracker (SVT). It is designed to reconstruct tracks in the Silicon Vertex Detector (SVX) and Central Tracking Chamber (CTC) with enough speed and accuracy to be used at trigger level 2 to select events containing secondary vertices from b decay.

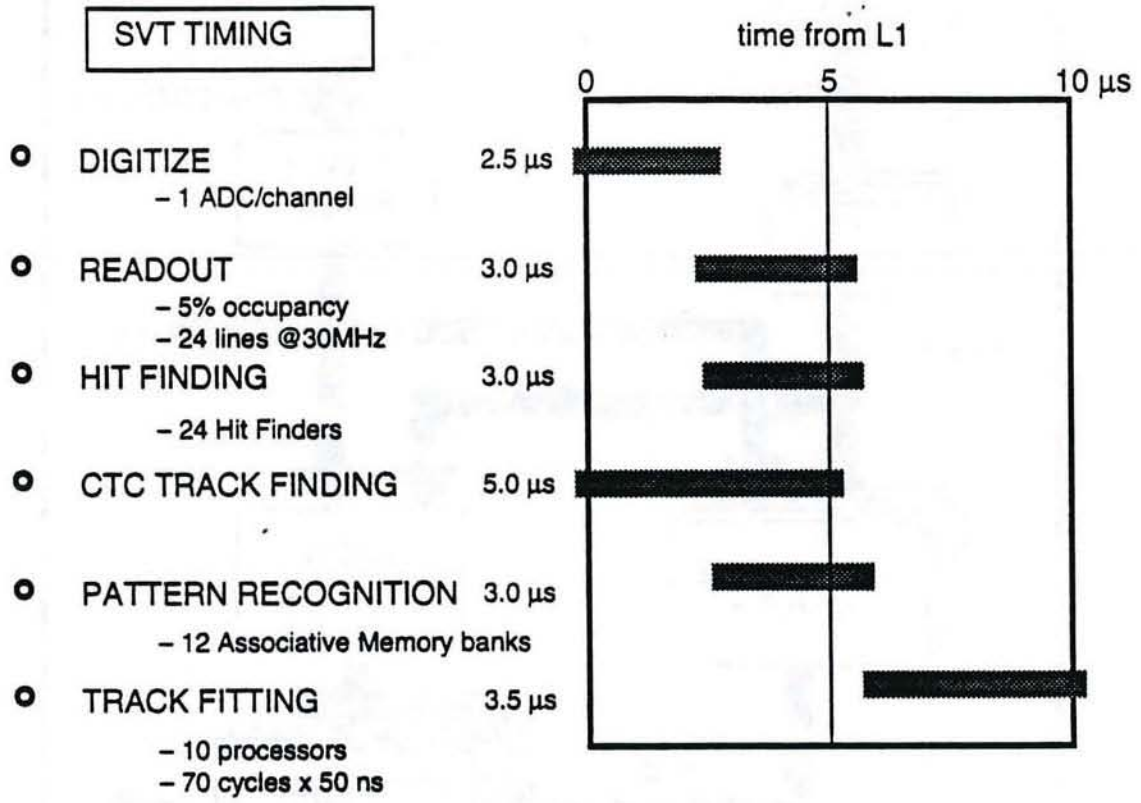

Figure 62: The overall timing of SVT for the average event.

Table 24: The first row shows the cross sections for a muon with p_T greater than 3 GeV/c and impact parameter greater than 100 um. The second row shows the cross sections for a muon with p_T greater than 6 GeV and no impact parameter information. The third row shows the cross sections we are left with if we take the cross section in the second row (without SVT) and apply an "offline" cut of 100 μm on the impact parameter of the muon. The first column (All) is the cross section for signal plus background. The second column ($b \rightarrow \mu X$) is the cross section for signal only.

	All	$b \rightarrow \mu + X$
SVT: $p_T > 3$ GeV, D> 100μm	80 nb	75 nb
no SVT: $p_T > 6$ GeV	80 nb	21 nb
no SVT: $p_T > 6$ GeV, D> 100μm offline	10 nb	6 nb

named roads, and are transmitted from the Associative Memory to a farm of processors (Track Fitters) where the track finding process is refined up to the full spatial resolution of SVX ($\sim$ 15 μm). Each processor in the farm receives one road from the Associative Memory, retrieves full resolution hits from the Event Memory and reconstructs one or more tracks within that road. All the processors in the farm do their work in parallel, each processor on a different road. The number of processors is large enough so that each processor has only one road to solve in the majority of events. Every time a processor finds a track it performs a geometrical fit and computes track parameters (impact parameter, momentum, ϕ). The expected accuracy of the track parameters from the SVT is:

$$\sigma_D = 35\mu\text{m} \ @ \ p_T = 2 \text{ GeV/c}$$

$$\sigma_\phi = 1 \text{ mrad} \ @ \ p_T = 2 \text{ GeV/c}$$

$$\sigma_{p_t} = 0.3\% \ p_T \text{ (GeV/c)}$$

Figure 62 shows the overall timing of SVT for the average event. Time is counted in microseconds from Level 1 Accept and is shown at the top. As can be seen from this diagram, SVT operation is finished in 10μs . Readout, Hit Finding and Associative Memory feeding overlap in time because they are pipelined.

12 Project Schedule, Cost and Manpower Needs

The schedule for the SVX II project is shown in Fig. 63. The design and R&D work will continue through 1993 on each subsystem , with final design decisions being made early in 1994. The construction process, including testing of delivered components and sub-assemblies is expected to take one and a half to two years. This schedule is based on our experience in building the SVX and SVX′ detectors. While SVX II is a significantly larger device with more readout channels and a more complex design, we believe that we can gain in efficiency from our experience, and that with adequate resources the detector can be ready for installation in January 1996. The level of M&S (materials and services) funding, and the manpower requirements are estimated in Table 25 and Fig. 64.

Detectors

We will continue to test the existing detector designs using double-metal readout (DELPHI detectors are already in hand) and kapton-metal readout (using detectors of Opal's design), and to compare the measurement of these detectors to our calculations of detector capacitance for different strip layouts. We will pursue our own prototype detectors with two different manufacturers, and study the capacitance, leakage current, resolution performace, and finally radiation hardness of these prototypes. Initial resolution studies will use a radioactive source or laser, but more complete measurements may require a test beam run.

A final decision on the strip design will be made in fall 1993, and the production detectors ordered early in FY94.

Mechanical–Ladders, Electrical Bonding, and Bulkheads

We are presently pursuing different materials and styles for ladder construction. The mechanical and thermal properties of our initial prototype designs are presently being measured. We expect to pursue two or three designs for some time before a final decision. We are studying alternative schemes for the electrical connection between detectors and between the detectors and the readout chips, including wire-bonding, flip-chip and tab bonding. The initial test structures will provide experience wire-bonding the double-sided ladders.

Candidate materials for the bulkhead include carbon fiber composites and beryllium. The bulkhead design will incorporate the cooling channels in the structure. Test structures will be built for cooling tests, incorporating realistic heat loads.

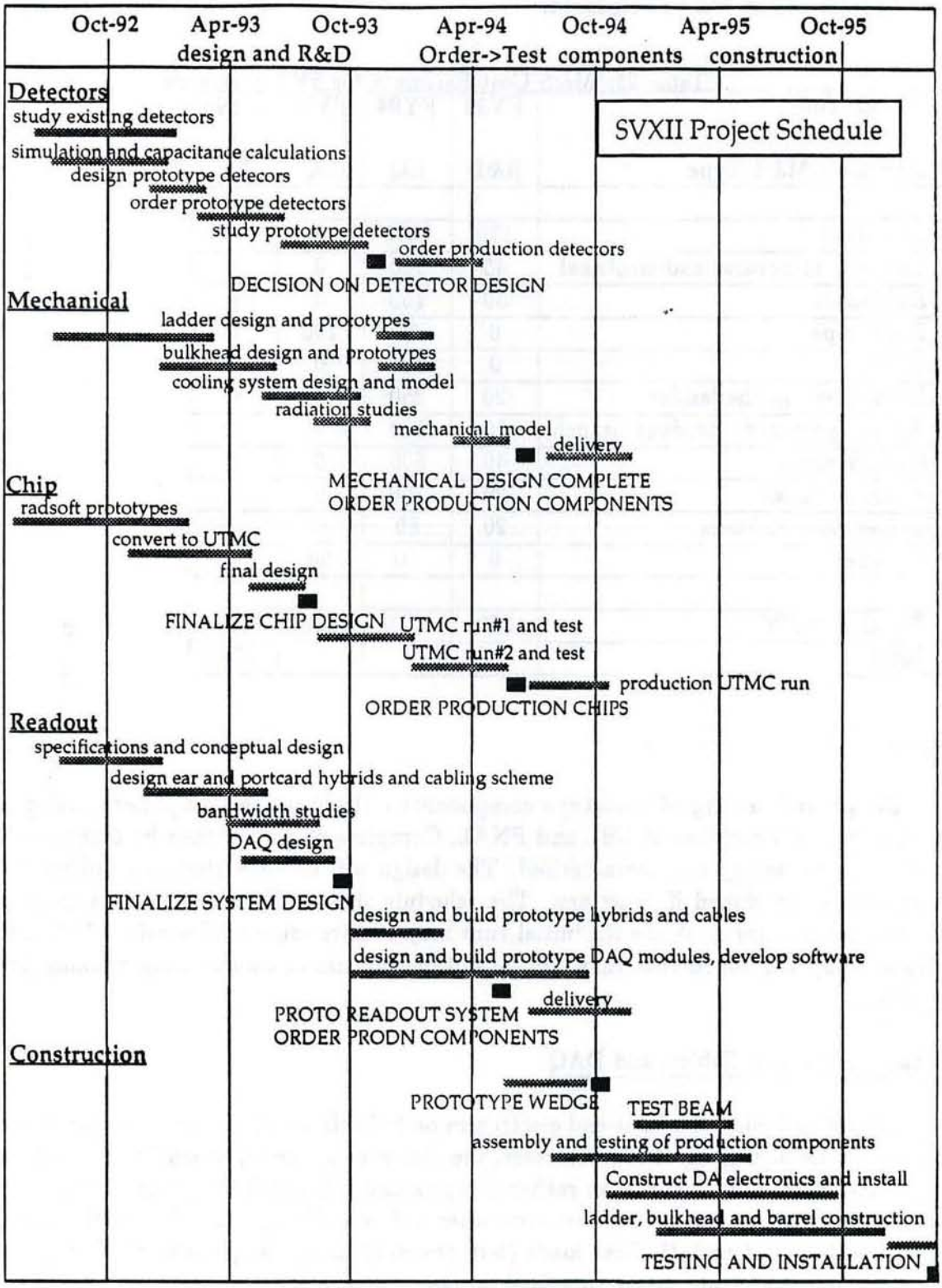

Figure 63: Schedule for the SVX II Stage 1 Project

The strength, thermal properties, and radiation hardness of all the materials to be used in the final design will be measured.

Table 25: M&S Cost Estimate for SVX II barrels

Fiscal Year	FY93	FY94	FY95	FY96
Dominant M&S Type	R&D	EQ	EQ	EQ
Detectors	170	1500	0	0
Ladders: structural and electrical	45	150	0	0
Bulkheads	30	150	0	0
Beam pipe	0	0	200	0
Chips	0	100	0	0
Hybrid/ear on the ladder	20	250	0	0
Hybrid/portcard - readout branch	15	100	0	0
DAQ System	40	630	0	0
Power Supplies	20	160	0	0
Cables/optical fibers	20	80	0	0
Fixtures	0	50	50	0
Total per FY	360	3170	250	0
Total				3780

Chip

Design and testing of prototype components - the front-end amplifier, analog pipeline and ADC - will continue at LBL and FNAL. Complete chips will then be fabricated in non-rad-hard technology and characterised. The design will be converted to a rad-hard process, and further developed if necessary. The schedule shown allows for three runs of the rad-hard process in total. While the initial runs may require some modifications before the final production, it is hoped that they will be suitable for use in constructing working prototype ladders.

Readout-hybrids, Cables, and DAQ

We are designing the front-end electronics on hybrids which are bonded onto the detector surface. The packaging of the detectors, the electronics, the on-board hybrid and the bulkhead and cooling channel is then rather complex and will require significant engineering. We expect to make several simple test structures before building realistic models. We will use live detectors and realistic heat loads (but probably using the present SVX chips) to build prototypes before committing to a final design.

There will be a readout cable branch per wedge, running at 53 MHz. We are investigating

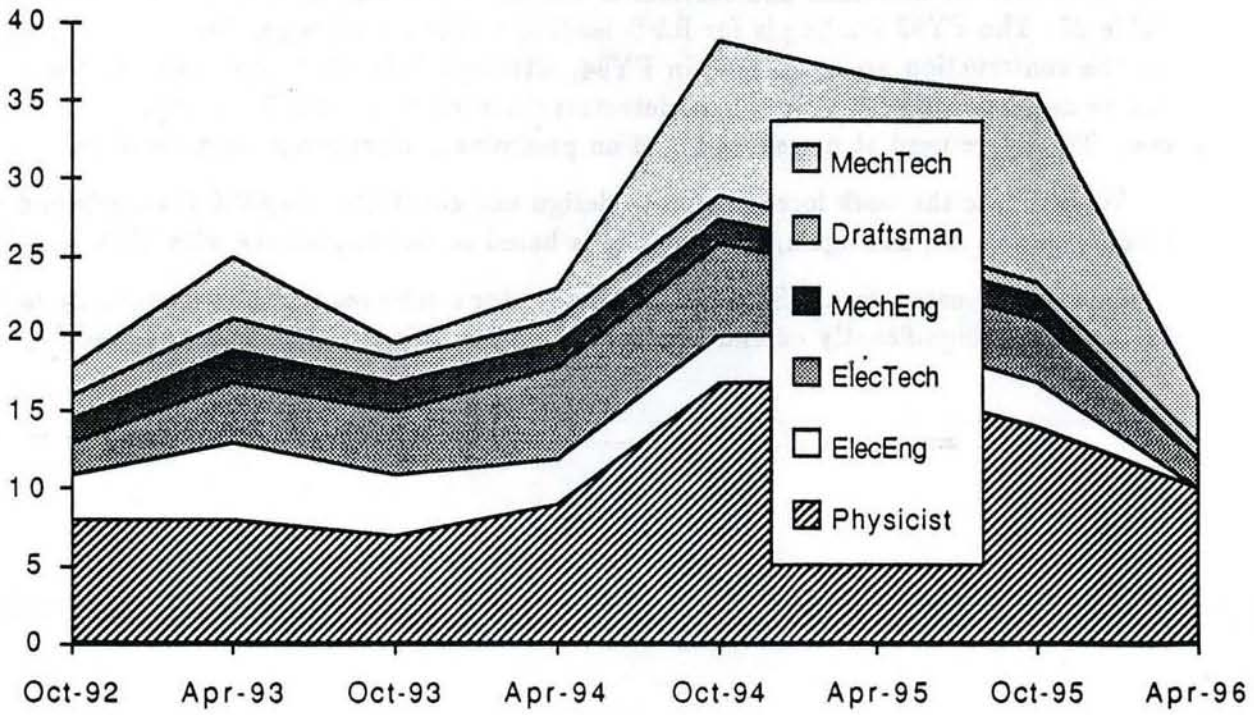

Figure 64: Mechanical technician, mechanical engineer, electronics technician, electronics engineer, and physicist full-time-equivalents needed.

the use of optical connections, and both optical and metal cabling schemes will be pursued initially. We will construct a realistic model of our design, to confirm the bandwidth and electrical properties of the bus, and again, all materials will be tested for susceptibility to radiation damage.

The data will be readout directly into memory in VME for both the SVT and the DAQ. Prototype VME boards will be built, initially to test the bandwidth performance of the system, and then to provide a prototype readout. The control of the front-end chips will also be via VME boards.

Construction

As the production components arrive, each will be tested and packaged into substructures; detectors, hybrids, ladder and bulkhead pieces, and branch cables. Hybrids and detectors will then be assembled on a ladder frame and electrically bonded, and the final ladders fully tested. The ladders will then be assembled onto the barrels. This is essentially the construction process used for SVX and for SVX′. Our estimate of the time and resources needed for this construction is scaled from this experience.

Funding and Manpower

As the design progresses a detailed cost estimate will be made. our initial estimate for the total cost for materials and services is \$3.8M. A breakdown by fiscal year is shown in Table 25. The FY93 funding is for R&D leading to the final design. Most of the materials for the construction are purchased in FY94, although it is likely that some of these costs can be deferred to FY95. The silicon detectors themselves account for a large fraction of the cost. The figure used at present is based on preliminary discussions with vendors.

We estimate the work force needed to design and construct the SVX II barrels and their readout in Fig. 64, and again, the estimate is based on our experience with SVX and SVX'.

With these resources, the SVX II Stage 1 detector can be ready for installation in January 1996, and will significantly extend the physics capabilities of CDF for Run II and beyond.

References

[1] G. Punzi and L. Ristori, "SVT: The Silicon Vertex Tracker", Version 3.4, CDF 1872, December, 1992.

[2] F. Bedeschi, CDF 371, 1985 and references contained therein.

[3] R. Hughes, *et. al.*, CDF 1626, 1991.

[4] V. Luth, *Spatial Resolution of Silicon Detectors: A Monte Carlo Study*, SLAC Report (1991)

[5] M. Binkley, private communication.

[6] F. Abe et al. Phys. Rev. Lett. **68**, 447 (1992).

[7] D. Kennedy and P. Langacker, Phys. Rev. **D44**, 1591(1991).

[8] J. Huth, Proc. of Particles and Fields '91, 151 (1991); Presentation to HEPAP Subpanel, Feb 28, 1992.

[9] F. Berends et al. Fermilab-Pub-90/213-T (1990).

[10] G.L. Kane, *Top Quark Physics*, UM-TH-91-32 (1991).

[11] See for example, M. Gold, C. Haber, P. Tipton, *b Physics with Existing Colliders*, Physics at Existing Colliders, D. Green and H. Lubbati, editors, World Scientific, New Jersey, 1990.

[12] A. H. Mueller and J. Nason, Phys. Lett 157B, 226 (1985).

[13] M. S. Witherell, *Heavy Quark Physics and the CKM Matrix*, preprint UCSB-HEP-91-06, 1991 SLAC Summer Institute, August, 1991.

[14] J. L. Rosner, *The CKM Matrix and B Physics*, preprint EFI-92-02, Workshop on b Physics, Edinburgh, Scotland, December 9, 1991, submitted to J. Phys. G.

[15] H. Schröder, $B\bar{B}$ *Mixing*, preprint DESY 91-139, to be published in "B Decays", edited by S. Stone, World Scientific, Singapore.

[16] W. Venus, "Results and Perspectives in Particle Physics", La Thuile, Aosta Valley, March, 1992.

[17] H. Albrecht et al. (ARGUS collaboration), Phys. Lett. 197B, 452 (1987)

[18] M. Artuso et al. (CLEO collaboration), Phys. Rev. Lett. 62, 2233 (1989)

[19] J. Rosner, Presentation to HEPAP subpanel, Fermilab, February 27, 1992.

[20] N. S. Lockyer et al. *Proposal for a B-Physics Experiment at TEV I: The μBCD*, October 1990, unpublished.

[21] *b Physics at CDF*, June 4, 1991, CDF Collaboration.

[22] ARGUS Collaboration, DESY 92-050, March 1992

[23] Reported by Cassel, DPF, Fermilab, November 1992.

[24] F. Abe et al, Phys. Rev. Lett. 68 (1992) 3404.

[25] P. Nason, S. Dawson, K. Ellis, Nucl. Phys. B327 (1989) p. 49. This comparison is meant to validate our extrapolation, not to test ISAJET. A thorough comparison of ISAJET to NDE, where next to leading order corrections are done in ISAJET, can be found in D. Kuebel, *et al*, Phys. Rev. D, 43 (1991) p. 767.

[26] M. Bauer, B. Stech, and M. Wirbel, Z. Phys. C, 34, 103 (1987). This value for the branching ratio assumes $|V_{ub}/V_{cb}| = 0.1$. Recent results from CLEO II give a somewhat lower value, although there remains considerable model dependence. (see P. Drell, XXVI International Conference on High Energy Physics, Dallas, August, 1992.)

[27] M. Frautschi, CDF 1842, 1992.

[28] Nicolo Cartiglia, "Facts about Silicon Detectors", U.C.S.C. transparancies

[29] H.Ikeda, M.Tanaka, and S.Okuno, NIM A 313 (1992) 31–36

[30] J.A.Ellison, *Radiation Levels in D0 and Effects on Silicon Detectors,*, D0 Note 1155, July 12,1991.

[31] K. Yamamoto *et. al., Interstrip Capacitance of the Double Sided Slilicon Strip Detector*, presented to the IEEE meeting in Orlando, Fla, Oct., 1992. (preprint available)

[32] E. Barberis *et. al., Measurement of Interstrip and Coupling Capacitances of Silicon Microstrip Detectors*, presented to the the IEEE meeting in Orlando, Fla, Oct., 1992. (preprint available)

[33] S. Masciocchi (INFN Milano), A.Peisert (INFN Padova), C. Ronqvist (SEFT Helsinki), D.Vite and R.Wheadon (Imperial coll), *Capacitance Measurements on Silicon Microstrip Detectors*, presented to the IEEE meeting in Orlando, Fla, Oct., 1992. (preprint available)

[34] Ed Barsotti, Hector Gonzalez and Carl Swoboda, *D0 and CDF Silicon Strip Upgrade Project–Preliminary Conceptual Design–Electronics Implementation and Cost and Schedule Details*, Computing Division/PPI-123, December 31, 1992.

[35] M.Dell'Orso, L.Ristori "VLSI Structures for Track Finding" Nuclear Instruments and Methods A278 (1989) 436-440. S.R.Amendolia, F.Bedeschi, G.Bellettini, S.Galeotti, A.Lusiani, A.Menzione, F.Morsani, D.Passuello, L.Ristori. "Study of a Fast Trigger System on Beauty Events at Fixed Target and Colliders" Nuclear Instruments and Methods A289 (1990) 539-542. S.R.Amendolia, S.Galeotti, F.Morsani, D.Passuello, L.Ristori and N.Turini "The AMCHIP: A VLSI Associative Memory for Track Finding" Nuclear Instruments and Methods A315 (1992) 446-448.